

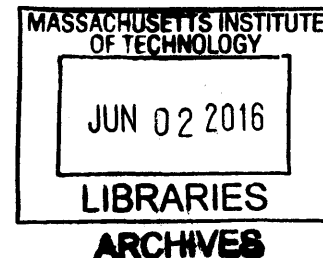
Electrochemical Studies of Oxygen Reduction for Aprotic Lithium-Oxygen Batteries

by

David Gator Kwabi

Bachelor of Science in Engineering, Mechanical Engineering
Princeton University, 2010

Master of Science, Mechanical Engineering
Massachusetts Institute of Technology, 2013



SUBMITTED TO THE DEPARTMENT OF MECHANICAL ENGINEERING IN PARTIAL
FULFILLMENT OF THE REQUIREMENTS FOR THE DEGREE OF

DOCTOR OF PHILOSOPHY IN MECHANICAL ENGINEERING

AT THE

MASSACHUSETTS INSTITUTE OF TECHNOLOGY
June 2016

© 2016 Massachusetts Institute of Technology. All rights reserved

Signature of Author..... **Signature redacted**

Department of Mechanical Engineering
May 17, 2016

Certified by..... **Signature redacted**

A handwritten signature in black ink, appearing to be "Yang Shao-Horn".

Yang Shao-Horn
W.M. Keck Professor of Energy
Thesis Supervisor

Accepted by..... **Signature redacted**

Rohan Abeyaratne
Professor of Mechanical Engineering
Chairman, Department Graduate Committee

Electrochemical Studies of Oxygen Reduction for Aprotic Lithium-Oxygen Batteries

by

David G. Kwabi

Submitted to the Department of Mechanical Engineering
on May 17, 2016

in partial fulfillment of the requirements for the degree of
Doctor of Philosophy in Mechanical Engineering

Abstract

Understanding oxygen electrochemistry lies at the heart of enabling many advanced energy storage and conversion technologies such as fuel cells, electrolyzers and metal-air batteries. Aprotic Li-O₂ electrochemistry is receiving much attention in this regard, as the Li-O₂ battery theoretically offers higher energy densities than conventional Li-ion systems at potentially lower cost. This thesis explores the relationship between the energetics of O₂ redox processes, and nucleation, growth, and reactivity of Li-O products in Li-O₂ batteries.

Using a combination of rotating disk techniques and first principles calculations, we first assess the influence of O₂⁻ and Li⁺ ion solvation on the energetics of O₂/O₂⁻ and Li⁺/Li redox processes. By combining these results with measurements of the redox potential of the Li⁺-O₂⁻ reaction intermediate, we show that both the coupling strength and solubility of the Li⁺-O₂⁻ complex are rationalized by the combined solvation of Li⁺ and O₂⁻ ions, with greater combined solvation increasing solubility but decreasing coupling energy, respectively. We next extend these results to studying the influence of applied potential and Li⁺-O₂⁻ solvation on the participation of soluble and solid species during Li₂O₂ growth, using the rotating ring disk electrode (RRDE) and electrochemical quartz crystal microbalance (EQCM) methods, respectively. As the applied potential increases, the reaction mechanism for Li₂O₂ formation switches from solution to surface-mediated, with the most likely pathways being Li⁺-O₂⁻ disproportionation and 2e⁻ transfer to O₂, respectively.

These insights are applied to understanding nucleation and growth of Li₂O₂ in Li-O₂ batteries, using high surface area carbon-based electrodes as model systems. We first report, for the first time, the formation of large ~ 300 nm donut-shaped particles of Li₂O₂ at high applied potentials during Li-O₂ discharge, and smaller particles (< 50 nm) at lower potentials. The existence of these disparate potential-dependent growth morphologies of Li₂O₂ strongly supports the predominance of potential-dependent reaction mechanisms, as hypothesized based on RRDE and EQCM results. We also show, however, that while increasing Li⁺-O₂⁻ solvation promotes higher discharge voltages, Li⁺-O₂⁻ solvation does not scale with Li₂O₂ particle size, particularly at low applied potentials. We therefore proposed a classical growth model of Li₂O₂ particle size based on Li₂O₂ reactivity with the electrolyte and Li₂O₂ supersaturation. Lastly, the influence of aging and electrolyte pKa on discharge product chemistry was explored. Aging electrochemically formed Li₂O₂ in a dimethylsulfoxide-based electrolyte promoted its decomposition to LiOH, while LiOH was found to be more likely to form upon discharge with decreasing effective pKa of water in the electrolyte, indicating higher proton availability.

These considerations highlight the importance of using model systems and first principles calculations to bridge fundamental investigation of redox processes with meso- and micro-scale studies of bulk discharge product formation, which is critical for a holistic understanding and rational design of practical metal-air batteries.

Thesis Committee:

Prof. Yang Shao-Horn, Dept of Mechanical Engineering, MIT (Chair)

Prof. Alexie Kolpak, Dept of Mechanical Engineering, MIT

Prof. Jeffrey Grossman, Dept of Materials Science and Engineering, MIT

Prof. Christopher Cummins, Dept of Chemistry, MIT

Acknowledgments

I am very grateful to many individuals who have supported me and this work. First, I would like to thank my adviser Prof. Yang Shao-Horn, for her unyielding devotion to my welfare as a student, but also my development as a thinker and researcher. I will be forever grateful for the many discussions we have had wrestling with my many harebrained ideas, and the rigor and logical acuity with which she approached answering scientific questions. I have benefited a great deal from her example. I would also like to thank my committee members Prof. Alexie Kolpak, Prof. Jeffrey Grossman and Prof. Christopher Cummins, for very stimulating discussions during thesis committee meetings and for highlighting potential areas for improvement and further study.

This work would not have been possible without input from a number of collaborators and fellow researchers. I am particularly grateful to Dr. Vyacheslav Bryantsev and Dan Addison, for collaborating on certain computational aspects of this work and many interactions on the role of solvation on Li-O₂ reaction mechanisms. I would also like to thank Thomas Batcho and Prof. Carl Thompson for joint work and a synergistic partnership on solvent effects on morphological features of Li₂O₂. Other collaborators within the Electrochemical Energy Lab (EEL) include Dr. Michal Tulodziecki, Dr. Livia Giordano and Shuting Feng. Many members of the Li-air subgroup of the EEL have been instrumental in teaching me various electrochemical techniques and providing excellent feedback on my progress including: Prof. Yi-Chun Lu, Prof. Betar Gallant, Dr. Jonathon Harding, Koffi Pierre Claver Yao, Dr. Sayed Sayed, Dr. Magali Gauthier, Chibueze Amanchukwu and Dr. Nagore Ortiz-Vitoriano. Many other members of EEL have been wonderful colleagues and friends over the years, and it has been a privilege to have worked with and received so much from such a bright and energetic group of individuals so committed to scientific excellence. I would be remiss if I did not mention my gratitude to the MIT Department of Facilities and the Environmental Health and Safety offices, who made it possible to conduct research in a clean and safe environment.

Outside the lab, I have benefited from the encouragement and support of friends from various walks of life, in particular from Park Street Church, the MIT Graduate Christian Fellowship, Sidney Pacific Graduate Residence, as well as from my high school years at the SOS-Hermann Gmeiner International College in Ghana and undergraduate studies at Princeton University. Lastly, I would like to thank my family for always being there for me. My parents Theresa and Albert, and my siblings Joel, Christabel and Sharon have been a solid rock in my life. I could not have done this without their faithful prayers on my behalf, and emotional and spiritual support. To them and to many others space will not permit me to mention, I say a heartfelt “thank you.”

Contents

Chapter 1: Introduction.....	14
1.1 Batteries and the Need for Energy Storage	14
1.2 Li-O ₂ Battery Operation and Challenges	17
1.3 Scope of Thesis	22
Chapter 2: Experimental and Computational Analysis of the Solvent-Dependent O ₂ /Li ⁺ -O ₂ ⁻ Redox Couple.....	26
2.1 Introduction	26
2.2 Experimental and Computational Methods.....	30
2.2.1 Electrochemical Cell and Electrode Preparation	30
2.2.2 Measurement of O ₂ /TBA ⁺ -O ₂ ⁻ redox potentials in aprotic organic solvents	31
2.2.3 Measurement of Li ⁺ /Li redox potentials in aprotic organic solvents.....	34
2.2.4 Calculation of oxygen reduction potentials in aprotic organic solvents	36
2.3 Results and Discussion.....	40
2.3.1 Measured and Computed O ₂ /TBA ⁺ -O ₂ ⁻ and Li ⁺ /Li standard potentials	40
2.3.2 Redox potential of O ₂ /Li ⁺ -O ₂ ⁻ and coupling strength and solubility of Li ⁺ -O ₂ ⁻	46
2.4 Conclusions	52
Chapter 3: Surface and Solution-Mediated Li ₂ O ₂ Reaction and Growth Mechanisms and Morphologies	54
3.1 Introduction	54
3.2 Experimental Methods	57
3.2.1 Rotating Ring Disk Electrode Measurements.....	57
3.2.2 Electrochemical Quartz Microbalance Measurements	58
3.3 Results	61
3.3.1 Potential-Dependent Li ₂ O ₂ Morphologies	61
3.3.2 Solution and Surface-Mediated Reaction Mechanisms for Li ₂ O ₂ Formation.....	65
3.3.3 Solvent Influence on Li ₂ O ₂ Morphology	81
Chapter 4: The Effect of Water on Discharge Product Growth and Chemistry in Li-O ₂ Batteries	92
4.1 Introduction	92
4.2 Experimental and Theoretical Methods	94
4.2.1 Cell Testing.....	94

4.2.2	Scanning and Transmission Electron Microscopy.....	95
4.2.3	pKa and Solvation Free Energy Calculations	95
4.3	Results	97
4.3.1	The Effect of Water on Li ₂ O ₂ Nucleation Rates on Low-Surface-Area Carbon Paper Electrodes.....	97
4.3.2	The Effect of Water on Li ₂ O ₂ Morphologies in High-Surface-Area CNT Electrodes 102	
4.3.3	The Influence of Water pKa and Solvation on the Reaction Product Chemistry – LiOH vs. Li ₂ O ₂	109
4.4	Conclusions	114
Chapter 5:	Chemical Instability of Dimethyl Sulfoxide in Li-O ₂ Batteries.....	116
5.1	Introduction	116
5.2	Experimental Methods	118
5.2.1	Electrochemical Measurements	118
5.2.2	Ball-milling of commercial Li ₂ O ₂	118
5.2.3	Mixing of suspensions containing Li ₂ O ₂ and KO ₂ in DMSO.....	119
5.2.4	X-ray Diffraction Characterization.....	119
5.2.5	Raman, FT-IR Spectroscopy and GC-MS Measurements.....	120
5.2.6	SEM Characterization.....	121
5.3	Results	121
5.3.1	Reactivity between electrochemically formed Li ₂ O ₂ and DMSO	121
5.3.2	Analyzing reactivity between Li ₂ O ₂ /KO ₂ and DMSO using chemical mixtures..	125
5.4	Conclusions	133
Chapter 6:	Summary and Perspectives	135
Appendix A	141
Appendix B	148
Appendix C	155
Appendix D	162
Appendix E – Safety Considerations	164
REFERENCES	166

List of Figures

Figure 1-1. 2014 U.S. energy production (left) and consumption (right) in quadrillion BTU. Source: US Energy Information Administration Annual Energy Review 2011, https://www.eia.gov/totalenergy/data/monthly/pdf/flow/css_2014_energy.pdf	15
Figure 1-2. Cathodic and anodic reaction potential ranges and corresponding gravimetric capacities of selected lithium battery chemistries. ⁷	17
Figure 1-3 (a) Schematic illustrating working principles of a Li-O ₂ cell. During discharge, Li ⁺ ions from the anode travel through Li-containing electrolyte and combine with reduced oxygen at the cathode to form Li ₂ O ₂ . The reverse process occurs on charge and (b) Ragone plot showing gravimetric power and energy densities based on the cathode mass for selected Li-ion and discharged Li-O ₂ batteries after first discharge. Li-O ₂ cathodes considered are based on freestanding hierarchically porous carbon (“graphene”), ¹² carbon nanofibers (CNF), ¹³ vertically aligned carbon nanotubes (VACNT), ¹⁴ and nano-porous Au. ¹⁵ Cells based on conventional Li-ion positive electrodes, LiCoO ₂ ¹⁶ and LiNi _{0.5} Mn _{0.5} O ₂ ¹⁷ are also shown.	19
Figure 2-1. Cyclic voltammograms (CVs) of ORR/OER in 0.5 M TBAClO ₄ in DME (black) and 0.1 M LiClO ₄ in DME (blue, 5× increase in current for comparison) on glassy carbon at 20 mV/s.	27
Figure 2-2. Schematic showing (a) TBA ⁺ -O ₂ ⁻ and Li ⁺ -O ₂ ⁻ complexes and (b) the effect of increasing O ₂ ⁻ and Li ⁺ ion solvation from weakly to strongly solvating media (such as DME to DMSO) on O ₂ /TBA ⁺ -O ₂ ⁻ and Li ⁺ /Li redox potentials measured using an Ag/Ag ⁺ reference electrode and Me ₁₀ Fc ⁺ /Me ₁₀ Fc as a solvent independent redox reference.	28
Figure 2-3. CVs at 20 mV/s showing reversible ORR/OER in oxygen-saturated electrolytes containing 0.3 M (red) and 0.5 M (black) TBAClO ₄ in DME. CVs were obtained with an Ag/Ag ⁺ electrode as reference. Polarization in 0.3 M show more resistive behavior than in 0.5 M.	31
Figure 2-4. CVs showing O ₂ /O ₂ ⁻ and Me ₁₀ Fc/Me ₁₀ Fc ⁺ redox reactions in argon and oxygen-saturated electrolytes containing 2mM Me ₁₀ Fc in (a) 0.5 M TBAClO ₄ in DME, 0.1 M TBAClO ₄ in (b) DMA (c) DMF (d) MeCN and (e) DMSO. CVs were obtained at 20 mV/s with an Ag/Ag ⁺ electrode as reference.....	33
Figure 2-5. CVs at 20, 50 and 100 mV/s showing O ₂ /TBA ⁺ -O ₂ ⁻ and Me ₁₀ Fc/Me ₁₀ Fc ⁺ redox reactions in oxygen-saturated electrolytes containing 2mM Me ₁₀ Fc in (a) 0.5 M TBAClO ₄ in DME, 0.1 M TBAClO ₄ in (b) DMA (c) DMF (d) DMSO and (e) MeCN. CVs were obtained with an Ag/Ag ⁺ electrode as reference.	34
Figure 2-6. (a) Thermodynamic cycle for the calculation of Li ⁺ or O ₂ ⁻ ion solvation. (b) Structures of the most stable X(Solvent) _n clusters (Solvent = DMSO, DME; X = Li ⁺ , O ₂ ⁻ , n = 4-6) obtained at the M06-L/6-311++G**//B3LYP/6-31G** level. Solvation effects on relative cluster stability are included using the dielectric continuum model with scaled (by 1.35) solute van der Waals radii.(c) Comparison of standard experimental (hexagons) and calculated (squares) O ₂ /O ₂ ⁻ and experimental (circles) and calculated (diamonds) Li ⁺ /Li redox potentials against computed Li ⁺ and O ₂ ⁻ solvation energies of each solvent. All Li ⁺ /Li and O ₂ /O ₂ ⁻ potentials are plotted with respect to MeCN and DME respectively and Nernstian corrections were applied to Li ⁺ /Li potentials, while O ₂ solubility corrections were applied to the O ₂ /TBA ⁺ -O ₂ ⁻ potentials. (d) Standard experimental redox potentials of O ₂ /TBA ⁺ -O ₂ ⁻ vs Li ⁺ /Li against combined Li ⁺ and O ₂ ⁻ solvation energy.....	39

Figure 2-7. (a) Steady-state CVs of $O_2/TBA^+-O_2^-$ and $Me_{10}Fc^+/Me_{10}Fc$ redox reactions collected at 20 mV/s in oxygen-saturated electrolytes containing 2 mM $Me_{10}Fc$ in 0.5 M $TBAClO_4$ in DME, 0.1 M $TBAClO_4$ in DMA and DMSO obtained with an Ag/Ag^+ reference electrode and Ni foam counter electrode. (b) Experimental standard $O_2/TBA^+-O_2^-$ and Li^+/Li redox potentials vs $Me_{10}Fc^+/Me_{10}Fc$ plotted against acceptor and donor numbers of each solvent. The lower cathodic/anodic currents of $Me_{10}Fc^+/Me_{10}Fc$ can be attributed to lower diffusivity and solubility of Fc compared to those of oxygen.^{68,94} 41

Figure 2-8. (a) CVs obtained at 50 mV/s showing bulk Li plating and dissolution using a Pt working electrode in 0.1 M $LiClO_4$ in DMSO, DMA, MeCN and DME (5× increase in current for comparison) using a Li metal counter electrode and Ag^+/Ag reference. The redox potential of Li^+/Li was found by the dotted lines, extrapolating the point of zero current during the anodic scan to the potential axis. (b) Comparison between Ag^+/Ag vs Li^+/Li potentials obtained from Li stripping experiments and those from open circuit potentials between the Ag quasi-reference electrode and Li metal immersed in the electrolyte. Both methods are in excellent agreement ($R^2 = 1.004$). 43

Figure 2-9. Schematic showing sectional view of RRDE during Li-ORR. Superoxide species are convected to the Au ring and oxidized, or converted to Li_2O_2 at the disk either by disproportionation or successive electron transfer. 46

Figure 2-10. (a) Ring current transients during RRDE measurements in 0.1 M $LiClO_4$ in DMSO at 900 rpm with disk held at 2.6 V vs Li^+/Li (b) Disk current transients during RRDE measurements in 0.1 M $LiClO_4$ in DMSO at 900 rpm with disk held at 2.6 V vs Li^+/Li (c) Variation of ring-to-disk charge ratios for potentiostatic experiments in 0.1 M $LiClO_4$ in DMSO, DME, DMA and DMF at ring potentials between 2.75 and 3.70 V vs Li^+/Li . The RRDE was rotated at 900 rpm for all measurements (d) Relationship between standard redox potentials for $O_2/TBA^+-O_2^-$ (circles) and $O_2/Li^+-O_2^-$ (diamonds) vs Li^+/Li (filled symbols) and $Me_{10}Fc^+/Me_{10}Fc$ (open symbols) and the total solvation energy for Li^+ and O_2^- ions calculated from a mixed cluster-continuum model for each solvent. Nernstian corrections were applied to Li^+/Li potentials, while O_2 solubility corrections were applied to the $O_2/TBA^+-O_2^-$ potentials. 47

Figure 2-11. Comparison between (a) combined computed solvation energy of Li^+ and O_2^- ions in DMSO, DME and DMA and computed (diamonds) and experimental (circles) $Li^+-O_2^-$ coupling energies and (b) $O_2/TBA^+-O_2^-$ vs Li^+/Li redox potentials with the logarithm of ring-to-disk charge during Li-ORR (circles) and combined computed solvation energy of Li^+ and O_2^- ions in DMSO, DME, DMA and DMF (diamonds). Dotted line shows linear regression through experimental data, $R^2 = 0.98$ 49

Figure 3-1. Discharge profiles of Li- O_2 cells of VC and Au/C at (a) 100 (b) 250 (c) 500 (d) 1000 and (e) 2000 mA/ g_{carbon} . (f) Data in (a-e) were normalized by the total weight of the electrode before discharge (carbon + Au + binder). 63

Figure 3-2. SEM images of (a) pristine VC electrode, (b) pristine Au/C electrode, (c) VC and (d) Au/C electrode discharged at 100 mA/g, (e) VC and (f) Au/C electrode discharged at 1000 mA/ g_{carbon} . SEM images were taken from the surface of the air electrode on the O_2 side. 64

Figure 3-3. CVs (uncorrected for i-R) of ORR/OER at 50 mV/s in O_2 -saturated 0.1M $LiClO_4$ in (a) DME and (b) DMSO on glassy carbon at 0, 400, 900 and 1600 rpm showing disk (left axis) and ring (right axis) current densities. Measurements were carried out in glass three-electrode cell with Li foil used as the counter and reference electrodes, while the ring was held at 3.5 V vs Li^+/Li . Estimated fractions of total ORR charge (diamonds) composed of solid (squares) and soluble (circles) species as a function of rotation speed in 0.1M $LiClO_4$ in (c) DME (open, red symbols)

and DMSO (filled, blue symbols). (d) Ar background-corrected total ring-disk charge versus applied disk potential in 0.1M LiClO₄ in DMSO (blue circles), DME (red diamonds) and DMF (green squares) at 900 rpm. Error bars for data in DMSO and DME are calculated from standard deviations from 3 independent measurements. 66

Figure 3-4. First 16 seconds of (a) disk and (b) ring current transients in Ar and O₂-saturated 0.1M LiClO₄ in DME at disk potentials of 2.5, 2.4, 2.2 and 2.0 V with the ring held at 3.5 V vs Li⁺/Li. First 30 seconds of (c) disk and (d) ring current transients in Ar and O₂-saturated 0.1M LiClO₄ in DMSO at disk potentials of 2.7, 2.5, 2.4 and 2.2 V with the ring held at 3.5 V vs Li⁺/Li..... 68

Figure 3-5. CVs showing ORR and OER reactions in 0.1M LiClO₄ in DME with potential plotted against (a) current and frequency and (b) M/z value of species deposited during ORR, and similar CVs in 0.1M LiClO₄ in DMSO with potential plotted against (c) current and frequency and (d) M/z value of species deposited during ORR. Dashed green lines in (a) and (c) indicate the delay between the ORR current onset and EQCM frequency decrease. 71

Figure 3-6. Calculated curves for the evolution of the RRDE collection efficiency vs the rate constant *k* of disproportionation at 900 rpm using equation S1 and viscosity of and superoxide diffusion coefficient in DMSO and DME. The dashed lines correspond to rate constants interpolated from 5% collection efficiency, and correspond to 2.3 and 5.0 s⁻¹ in DMSO and DME, respectively. 76

Figure 3-7. (a) Discharge profile and (b) Ex situ Raman spectra of CNT electrode discharged at 10 mA/g_C to ~ 4600 mAh/g_C in 0.1M LiClO₄ in DMSO..... 77

Figure 3-8. Schematic illustrating effect of ORR overpotential on predominant Li₂O₂ growth mechanisms..... 79

Figure 3-9. Galvanostatic discharge profiles using CNT electrodes at 25 and 500 mA/g_C to 4000 mAh/g_C in 0.1M LiClO₄ in MeCN, DME, DMSO and 1M LiNO₃ in DMA. An LiCoO₂-based anode was used for the MeCN electrolyte because of its chemical incompatibility with Li. 1M LiNO₃ was used in DMA instead of 0.1M LiClO₄ because the former has been shown to be compatible with Li metal,¹⁵⁸ which was used as the anode. 82

Figure 3-10. Ex situ SEM images of CNT electrodes discharged at 25 mA/g_C to 4000 mAh/g_C in (a) DME (b) DMSO (c) DMA and (d) MeCN. 84

Figure 3-11. Li₂O₂ toroid size vs computed rate of electrolyte decomposition plotted according to equation [3-5] and assuming constant supersaturation. 86

Figure 4-1. Thermodynamic cycle showing calculation of pK_a of water in different aprotic solvents. 96

Figure 4-2. (a) Current transient responses to potentiostatic discharge at 2.6 V in 0.1M LiClO₄ in DME with < 30 and 5000 ppm of water (first 50,000 seconds of discharge shown). SEM images of potentiostatically discharged electrodes in 0.1M in LiClO₄ in DME with (b) < 30 ppm and (c) 5000 ppm of water. Both samples were discharged to ~0.055 mAh. 98

Figure 4-3. Current transient responses to potentiostatic discharge at 2.0 V in 0.1M LiClO₄ in DME with < 30 and 5000 ppm of water (b) Analysis of potentiostatic response in 5000 ppm H₂O to determine the Avrami exponent *n*, where *Y* = fraction of species converted and *n* is the exponent in the Avrami equation $Y = 1 - \exp(-Bt^n)$ where *B* is a rate constant. SEM images of potentiostatically discharged electrodes in 0.1M LiClO₄ in DME with (c) < 30 ppm and (d) 5000 ppm of water. Both samples were discharged to ~10 mAh. 100

Figure 4-4. XRD pattern of Li-O₂ carbon paper electrode discharged at 2.0 V in 0.1M LiClO₄ in DME with 5000 ppm of water. 102

Figure 4-6. (a) Galvanostatic Li-O₂ discharge curves of CNT electrodes at 25 mA/g_C to 4000 mAh/g_C in 0.1M LiClO₄ in DME with 5000 and < 30 ppm of water. SEM images of CNTs discharged in 0.1M LiClO₄ in DME with (b) 5000 ppm and (c) < 30 ppm of water. (d) TEM images from CNT discharged in 0.1M LiClO₄ in DME with < 30 ppm of water..... 103

Figure 4-7. Galvanostatic Li-O₂ discharge curves of CNT electrodes at (a) 25 and (b,c) 250 and 500 mA/g_C in 0.1M LiClO₄ in DME with 5000 and < 30 ppm of water. *Ex situ* SEM images of Li-O₂ electrodes discharged at (c,d) 25 and (e,f) 500 mA/g_C in < 30 and 5000ppm of water.... 105

Figure 4-8. Schematic illustrating competition between surface and solvent-mediated nucleation of Li₂O₂ in the presence of water, which is modulated by electrode surface site concentration and activity. In the presence of water, high concentration and activity of surface sites in CNTs results in greater surface-mediated nucleation, while lower concentration and activity of surface sites in carbon paper results in more solvent-mediated Li₂O₂ nucleation..... 106

Figure 4-9. Raman spectra of pristine CNT and carbon paper electrodes, showing D and G bands from carbon. 107

Figure 4-10. First discharge capacity as a function of current density and water content in the catholyte of cells with carbon paper (squares), VC/Super P (circles) and CNT (diamond)-based electrodes and glyme-based solvents, with assumed specific surface areas of 1, 100 and 500 m²/g respectively. A similar plot is reported in the study by Schwenke *et al.*¹²⁸ with the data of Adams *et al.*⁷⁰ Data from Meini,¹⁵⁷ Lau,¹¹⁷ Aetukuri¹⁰⁹ and co-workers have been added for comparison. 108

Figure 4-11. (a) Galvanostatic and (b) *ex situ* XRD measurements of Li-O₂ CNT electrodes discharged at 25 mA/g_C to 4000 mAh/g_C in 0.1M LiClO₄ in MeCN with 5000 and < 30 ppm of water. SEM images of CNTs discharged in 0.1M LiClO₄ in MeCN with (c) < 30 and (d) 5000 ppm of water. The discharge potential in (a) is calculated assuming Li removal from LiCoO₂ occurs around 3.9 V vs Li⁺/Li. 109

Figure 4-12. (a) Optimized structure of four DME solvent molecules surrounding water molecule. Color code: Red = Oxygen; Grey = Carbon; White = Hydrogen. (b) Plot showing relationship between computed pK_a and solvation free energy of water in DME, MeCN, DMF and DMA. pK_a values were obtained from single point energy calculations at the M06L/6-311++G(d,p) level of theory performed on molecular structures fully optimized at B3LYP/6-31G(d,p) level..... 113

Figure 5-1. XRD patterns showing evolution of LiOH (red dashed lines) from (a) Li₂O₂ in a CNT electrode discharged at 100 mA/g_C to ~3000 mAh/g_C in 0.1 M LiClO₄ in DMSO after 0.5 h and 380 h of aging in electrolyte following the completion of discharge. The grey asterisk denotes a peak from the Al substrate. (b) Solid precipitates collected after centrifugation of suspensions containing commercial Li₂O₂, KO₂ and DMSO and Li₂O₂ and DMSO in mole ratios of 1:1:100 and 1:100 respectively after 500 hours of continuous stirring. The magnified section shows major peaks for Li₂O₂ and LiOH..... 122

Figure 5-2. Scanning Electron Microscopy (SEM) images of CNT electrodes discharged at 25 mA/g_C to ~4000 mAh/g_C in 0.1 M LiClO₄ in DMSO imaged (a) 0.5 hours (b) 12 hours (c) 24 hours (d) 576 hours after discharge. Examples of LiOH particles are marked by large circles and examples of Li₂O₂ discs by smaller circles. 123

Figure 5-3. SEM images of ball-milled Li₂O₂. Li₂O₂ particles have oval-shaped morphologies, and reach up to 1 μm in size. 126

Figure 5-4 (a) Raman spectra of solid precipitates collected after centrifugation of suspensions of Li₂O₂, KO₂ and DMSO and Li₂O₂ and DMSO in mole ratios of 1:1:100 and 1:100 respectively after 500 hours of continuous stirring. Spectra of commercial Li₂O₂ (ball-milled) and LiOH

powders are shown for comparison. Spectra between 3000 and 4000 cm^{-1} have been background-corrected (see Figure S7). (b) FT-IR spectra of neat DMSO, and suspensions of Li_2O_2 , KO_2 and DMSO (with mole ratio of 1:1:100) and Li_2O_2 and DMSO (1:100) after 24 and 336 hours of mixing. The peak at 1142 cm^{-1} indicates the symmetric stretch of the SO_2 group in DMSO_2 (c) Gas chromatograms showing evolution of column pressure with time of analytes of neat DMSO and supernatants of suspensions of Li_2O_2 , KO_2 and DMSO and Li_2O_2 and DMSO in mole ratios of 1:1:100 and 1:100 respectively after 500 hours of continuous mixing and (d) mass spectra of neat DMSO and after ~6 min of analyte evolution for supernatants of suspensions containing Li_2O_2 and DMSO and KO_2 , Li_2O_2 and DMSO..... 128

Figure 5-5. Schematic showing proposed mechanism for DMSO decomposition via either (a) nucleophilic attack by superoxide or (b) proton abstraction by superoxide ions followed by the formation of DMSO_2 and LiOH 131

Chapter 1: Introduction

1.1 Batteries and the Need for Energy Storage

Energy demand in the United States (Figure 1-1) and around the world is dominated by fossil fuel-based sources such as petroleum, natural gas and coal, the supplies of which are not expected to run out at least for the next 100 years. There is scientific consensus, however, that greenhouse gas emissions from continued fossil fuel consumption will lead to severe and irreversible climate change in the next few decades. This has generated interest in developing renewable energy sources such as wind, solar, tidal and geothermal power. Unfortunately, these energy sources are temporally intermittent, and therefore must be used within a framework of comprehensive energy storage, primarily *via* batteries and chemical fuels such as hydrogen and biofuels. Much research attention has thus been devoted to finding and developing renewable energy storage alternatives.

1-4

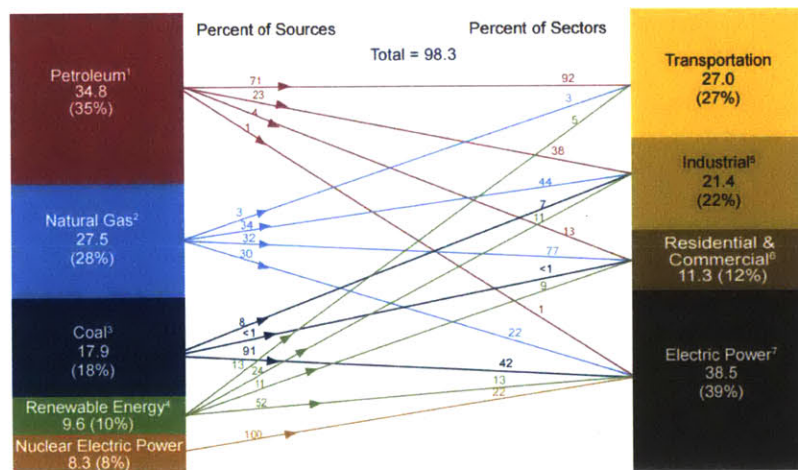


Figure 1-1. 2014 U.S. energy production (left) and consumption (right) in quadrillion BTU.

Source: US Energy Information Administration Annual Energy Review 2011,

https://www.eia.gov/totalenergy/data/monthly/pdf/flow/css_2014_energy.pdf

Electrochemical energy storage and conversion devices such as batteries and capacitors are particularly attractive as they can accommodate a wide variety of chemistries and material configurations, suited to a varied selection of power and energy density requirements.^{5,6} Lithium-ion batteries have powered the portable device revolution and are ubiquitous in phones, laptop computers and remote sensors. Redox flow batteries hold great promise for stationary applications such grid-scale load leveling, while supercapacitors have been used for regenerative braking in hybrid electric vehicles and energy harvesting from mechanical movement and electromagnetic fields.⁵

Despite their promise, current electrochemical energy storage and conversion devices have much lower energy storage capabilities than fossil fuels and implementing them as fossil fuel replacements would be much too costly, particularly for energy-intensive applications such as fully electric vehicles and industrial power plants. A great deal of fundamental research has therefore been devoted to finding and developing battery concepts with higher theoretical energy densities than are currently available.

The gravimetric energy density (in Wh per kilogram of active material weight) of any battery chemistry can be calculated based on the difference in electric potential (in volts) between the negative electrode (called the anode during discharge) and positive electrode (cathode during discharge), and the amount of charge stored per unit weight of material (or capacity, in mAh/g).

Figure 1-2 plots the reaction potentials and associated gravimetric capacities of selected cathodic and anodic cell chemistries based on the intercalation of lithium into various host lattices. The maximum possible gravimetric energy density of a full cell operating with a given pair of negative and positive redox levels would equal the product of the smaller gravimetric capacity and the potential difference between cathodic and anodic redox reactions. State-of-the-art lithium-ion cathodes such as LiCoO_2 and $\text{LiNi}_{0.5}\text{Mn}_{0.5}\text{O}_2$ have theoretical gravimetric energy densities ranging between 500 – 600 $\text{Wh/kg}_{\text{cell}}$ (assuming a graphite-based anode), but practical energy densities (including the mass of other cell package components such as electrolyte, separator and binder) are about 30 – 40% of that value, and would be impractical for energy-dense applications such as electric vehicles, which require batteries with energy densities of at least 500 Wh/kg at the package level.

Fervent interest has arisen over the past two decades surrounding the non-aqueous rechargeable Li-air, or Li-oxygen (Li-O_2) battery, which is theoretically projected to store ~ 3500 $\text{Wh/kg}_{\text{cell}}$, and is thus attracting increasing attention as a future energy storage alternative to fossil fuels. This thesis will focus exclusively on using electrochemical techniques to fundamentally understand and thereby improve energy storage capabilities in prototypical non-aqueous Li-O_2 batteries.

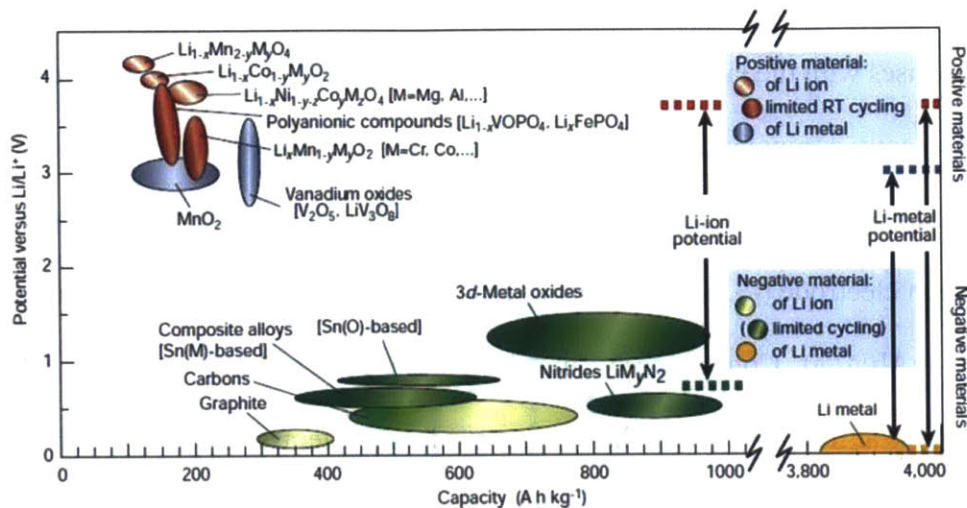


Figure 1-2. Cathodic and anodic reaction potential ranges and corresponding gravimetric capacities of selected lithium battery chemistries.⁷

1.2 Li-O₂ Battery Operation and Challenges

Li-O₂ batteries differ from traditional Li-ion batteries in that rather intercalating into a host lattice, Li ions react directly with oxygen dissolved in the electrolyte, resulting in the formation of lithium-oxygen compounds (Figure 1-3a).^{8,9} In prototypical rechargeable non-aqueous Li-O₂ batteries, Li⁺ ions are formed from the oxidation of the metallic Li anode on discharge and travel through the electrolyte to the cathode. At the cathode, oxygen is simultaneously reduced in the presence of these Li⁺ ions to form a solid, insoluble Li₂O₂ phase, while electrons in the external circuit perform electrical work. This process is reversed during charge with the decomposition of Li₂O₂, evolution of molecular oxygen and plating of Li at the negative Li electrode.

This configuration comprises a hybrid between a fuel cell and a traditional intercalation battery, but dispenses with the latter's need to use heavy transition metals in the positive electrode. Replacing these heavy components with lightweight, high-surface-area materials such as carbon, and using a Li anode, which is an exceptionally light metal with a low redox potential vs the standard hydrogen electrode (-3.04 V), contributes to a high cell voltage (2.96 V) and gravimetric capacity (1168 mAh/g_{cell}). Consequently, the theoretical energy density for the Li-O₂ battery (~3500 Wh/kg_{cell}) is at least 3× greater than for most Li-ion systems.⁹ It is additionally envisioned that using oxygen from ambient air will contribute to cost reduction, raising the prospect of higher energy density batteries than are currently available at significantly lower cost per kWh.

Much research effort has gone into the development of Li-O₂ cell prototypes that can achieve projected gravimetric energy density gains over Li-ion batteries.¹⁰ Gravimetric power and energy densities based on the positive electrode weight for selected Li-ion and discharged Li-O₂ cathode chemistries are shown in the Ragone plot in Figure 1-3b. At a gravimetric power of ~100 W/kg_{cell}, Li-ion cathodes such as LiCoO₂⁵ and LiNi_{0.5}Mn_{0.5}O₂⁶ can deliver energy densities between 500 – 800 Wh/kg_{cell}, while various Li-O₂ cathodes based on graphene, carbon nanofibers, and Vulcan carbon have demonstrated 1800 – 2800 Wh/kg_{cell}. These energy densities suggest that Li-O₂ batteries provide a route to achieving 3 – 5 times the energy density of current lithium-ion battery configurations, although system-level advantages might be lower.¹¹

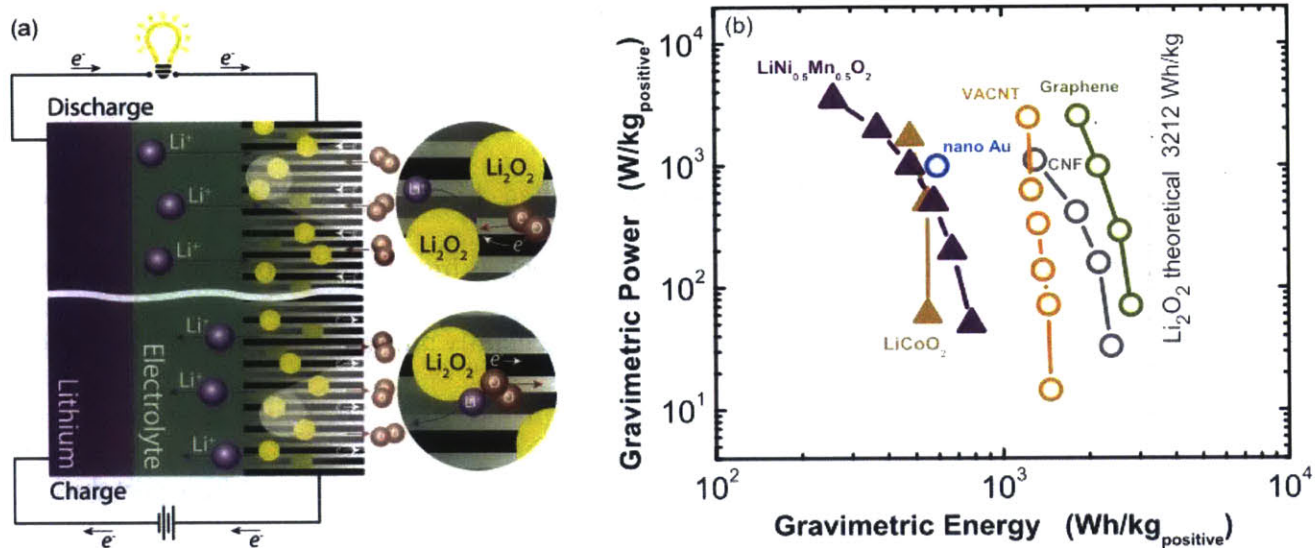


Figure 1-3 (a) Schematic illustrating working principles of a Li-O₂ cell. During discharge, Li⁺ ions from the anode travel through Li-containing electrolyte and combine with reduced oxygen at the cathode to form Li₂O₂. The reverse process occurs on charge and (b) Ragone plot showing gravimetric power and energy densities based on the cathode mass for selected Li-ion and discharged Li-O₂ batteries after first discharge. Li-O₂ cathodes considered are based on freestanding hierarchically porous carbon (“graphene”),¹² carbon nanofibers (CNF),¹³ vertically aligned carbon nanotubes (VACNT),¹⁴ and nano-porous Au.¹⁵ Cells based on conventional Li-ion positive electrodes, LiCoO₂¹⁶ and LiNi_{0.5}Mn_{0.5}O₂¹⁷ are also shown.

Although prototypical Li-O₂ cells have demonstrated *first discharge* gravimetric energy densities several-fold higher than those of current Li-ion batteries at the cell level, much is still not understood about Li₂O₂ growth mechanisms, and how Li₂O₂ morphologies can be optimized for high energy density. This point is particularly critical since the volumetric energy density of a Li-O₂ battery critically depends on pore volume utilization, which can vary depending on how space-filling Li-O₂ discharge product morphology is.¹⁰ How Li₂O₂ growth mechanisms and morphology

are affected by electrolyte solvent and applied potential will be addressed in detail in **Chapters 2 and 3**.

In addition to a need for fundamental understanding, Li-O₂ battery technology still faces several device-level challenges to practical application, such as high charging overpotentials, low rate capability and poor cycle life. These challenges are generally understood as having two major origins. The first has to do with the highly insulating nature of Li₂O₂, which is theoretically predicted to have a wide band gap of ~ 5 eV,¹⁸ and can sustain very limited charge transport during discharge and charge, either by electron tunneling^{19–21} or hole polaron hopping between O₂²⁻ dimers.^{18,22,23} Thus, the formation of Li₂O₂ deposits on the positive electrode effectively passivates the electrode toward further electrochemical formation reactions and leads to low rate capability²⁴ and slow charging kinetics^{8,25} (overpotentials ≥ 1000 mV on charge). A number of strategies to speed up Li₂O₂ charging kinetics have been proposed. One of the most prominent is to use solution-phase redox mediators that are oxidized above the thermodynamic potential for Li₂O₂ formation during charge, and can in turn oxidize electrodeposited Li₂O₂ in solution. This obviates the need for Li₂O₂ oxidation to take place *via* kinetically sluggish electron transfer to the electrode. A variety of small molecule-based redox mediators^{26–28} are capable of oxidizing Li₂O₂ at overpotentials of ≤ 500 mV, as opposed to ~ 1000 mV, which is typical in the absence of redox mediation. Another strategy is the incorporation of transition metal-based nanoparticles in the positive electrode,^{29–32} which can react with Li₂O₂ and form Li_xMO₂-type (where M is the transition metal) compounds^{32,33} that are drastically easier to oxidize than Li₂O₂, by up to 500 mV.

A more significant impediment to the practical implementation of Li-O₂ electrochemistry is the chemical instability of oxygen reduction reaction (ORR) intermediates and products against many cell components such as the electrolyte and cathode surface. In early studies, organic

carbonate-based electrolyte solvents commonly used in Li-ion batteries were used as electrolyte solvents for prototypical Li-O₂ cells. They have however been shown to be highly susceptible to nucleophilic attack by the superoxide (O₂⁻) ORR intermediate,³⁴⁻³⁶ resulting in the formation of side products such as Li₂CO₃, HCO₂Li and CH₃CO₂Li during discharge. These species are expected to decompose at higher potentials than Li₂O₂ (> 4.5 V vs Li⁺/Li), and thus accumulate during electrochemical cycling, leading to capacity losses and progressively higher charging overpotentials during cycling. Several non-carbonate-based electrolyte solvents have been shown to support more reversible cycling, however electrolyte decomposition continues to persist in these systems as well. Polar solvents in particular such as dimethylsulfoxide (DMSO) and dimethylformamide (DMF) are susceptible to proton abstraction,^{37,38} while relatively less polar media such as ethers are vulnerable to hydrogen removal or autoxidation in the presence of O₂.³⁹⁻⁴² Silane and amide-based solvents⁴³⁻⁴⁵ as well as ionic liquids^{46,47} are promising alternatives, however they all exhibit electrolyte degradation to some degree.^{48,49}

Compounding the problem of reactivity even further is the proliferation of reports showing that reduced oxygen species (ROS) such as O₂⁻ and Li₂O₂ react with nominally inactive cell components such as the carbon used in the positive electrode,^{14,50-53} electrolyte salt⁵⁴ and binder.⁵⁵ These reactions contribute further to the high charging overpotentials and poor cyclability seen in carbon-based Li-O₂ cells. The use of non-carbon-based positive electrodes such as TiC⁵⁶/Ti₄O₇⁵⁷ Co₃O₄^{58,59} and Au¹⁵ can circumvent this problem, but at the cost of drastically reducing gravimetric energy density – as an example, the use of nanoporous Au as the cathode results in a gravimetric energy density that is comparable to those of current Li-ion batteries (see Figure 1-3b). Indeed, carbon's combination of low density, affordability and high specific area make it an almost ideal positive electrode for practical systems, and rather than replacing it outright, a more prudent

approach would be to passivate it toward parasitic reactions using thin coatings of inert, conductive materials.

Due to the scale and complexity of possible parasitic interactions between ROS and various Li-O₂ cell components, a systematic understanding of decomposition reaction pathways is critical, in order to rationally design Li-O₂ cells resistant to long-term chemical degradation. In **Chapter 4**, we show that the effective pK_a of water, which is a potential contaminant in nominally non-aqueous electrolytes, can dictate the formation of Li₂O₂ vs LiOH during discharge, which is an important factor to consider in choosing electrolytes for rechargeable Li-O₂ batteries, where precise control of discharge product chemistry is critical. In **Chapter 5**, model chemical studies of O₂⁻ and Li₂O₂ reactivity with DMSO are used to reveal the sensitivity of Li-O₂ discharge product chemistry to the amount of contact time with the electrolyte, which had not been considered in prior reactivity studies.

1.3 Scope of Thesis

This thesis explores the relationship between the energetics of O₂ redox processes, and nucleation, growth, and reactivity of Li-O products in Li-O₂ batteries. **Chapter 2** is a study of the influence of O₂⁻ and Li⁺ ion solvation on the energetics of O₂/O₂⁻ and Li⁺/Li redox processes using a combination of rotating disk techniques and first principles calculations. By combining these results with measurements of the redox potential of the Li⁺-O₂⁻ reaction intermediate, we will show that both the coupling strength and solubility of the Li⁺-O₂⁻ complex can be rationalized by

the combined solvation of Li^+ and O_2^- ions, with greater combined solvation increasing solubility but decreasing coupling energy, respectively.

Building on these findings, **Chapter 3** reports on the influence of soluble ORR intermediates on final Li_2O_2 morphologies formed in prototypical Li- O_2 cells with high surface area, multi-walled carbon nanotube (CNT) and Vulcan carbon electrodes. We first report, for the first time, the formation of large ~ 300 nm donut-shaped particles of Li_2O_2 at high applied potentials during Li- O_2 discharge, and smaller particles (< 50 nm) at lower potentials. The existence of these disparate potential-dependent growth morphologies of Li_2O_2 strongly supports the predominance of potential-dependent reaction mechanisms. These reaction mechanisms are investigated using the ring disk electrode (RRDE) and electrochemical quartz crystal microbalance (EQCM) methods and the influence of applied potential on Li^+ - O_2^- solvation and the participation of soluble and solid species during Li_2O_2 growth is shown. As the applied potential increases, the reaction mechanism for Li_2O_2 formation switches from solution to surface-mediated, with the most likely pathways being Li^+ - O_2^- disproportionation and $2e^-$ transfer to O_2 , respectively.

We also show, however, that while increasing Li^+ - O_2^- solvation promotes greater discharge potentials, Li^+ - O_2^- solvation does not scale with Li_2O_2 particle size, particularly at low applied potentials. In this regard, we propose a growth model that rationalizes Li_2O_2 particle sizes on the basis of Li_2O_2 reactivity with the electrolyte and Li_2O_2 supersaturation, which influences the nucleation barrier.

Reactivity between Li_2O_2 and the electrolyte is explored in more depth in **Chapters 4 – 5**. In **Chapter 4**, we highlight the importance of electrolyte deprotonation generally to decomposition reactions during Li- O_2 discharge by showing that the effective pKa of water in non-aqueous

solvents influences discharge product chemistry: low pKa is indicative of a lower barrier to deprotonation by ROS, leading to LiOH formation during discharge, while high pKa is likelier to result in Li₂O₂. While much evidence exists for chemical reactivity between ROS produced during Li-O₂ discharge and many electrolyte solvents used in Li-O₂ batteries, the long-term stability of discharge product chemistry upon aging with the electrolyte is poorly understood. Thus, in **Chapter 5**, we show that aging discharged Li₂O₂ in DMSO-based electrolyte induces a change to LiOH over time. Suspensions of Li₂O₂ and KO₂ in DMSO successfully mimic this evolution and show that superoxide ions accelerate the deprotonation and subsequent decomposition of DMSO.

Combining fundamental studies of metal-O₂ reaction intermediate energetics with model studies showing how ROS contribute to discharge product growth can shed light on reaction and decomposition mechanisms in these batteries, and highlight important design considerations for the development of practical energy storage systems with high energy density, rechargeability and cycle life.

Chapter 2: Experimental and Computational Analysis of the Solvent-Dependent O₂/Li⁺-O₂⁻ Redox Couple.

Reproduced in part with permission from David Kwabi, Vyacheslav S. Bryantsev, Thomas P. Batcho, Daniil Itkis, Carl V. Thompson, and Yang Shao-Horn, Experimental and Computational Analysis of the Solvent-Dependent O₂/Li⁺-O₂⁻ Redox Couple: Standard Potentials, Coupling Strength, and Implications for Li-O₂ Batteries. *Angew. Chem. Int. Ed. Engl.* **2016**, *9*, 3129–3134. Copyright 2016, John Wiley and Sons, Inc

2.1 Introduction

Activating oxygen chemistry^{1,4,60,61} is central to transforming energy storage by providing high gravimetric energy in devices such as rechargeable Li-O₂^{8,25} and sodium-oxygen batteries⁶² and reversible fuel cells.⁶³ Non-aqueous Li-O₂ batteries operate by reducing molecular oxygen in the presence of Li⁺ to form Li₂O₂ at the positive electrode on discharge and releasing oxygen by oxidizing Li₂O₂ on charge. As noted in **Chapter 1**, there are significant challenges to practical implementation of Li-O₂ batteries, including low voltage efficiency, cycle life, and power capability. These are due primarily to the lack of fundamental understanding of oxygen reduction and evolution reaction kinetics and parasitic reactions in Li-O₂ batteries.

The kinetics of oxygen reduction in the presence of strongly coordinating Li⁺ are sluggish (Figure 2-1), and its elementary reaction steps are not well understood. Oxygen reduction proceeds first by the formation of O₂⁻^{64,65} and then lithium superoxide (Li⁺ + O₂⁻ → Li⁺-O₂⁻).^{66,67} Secondly,

Li_2O_2 is formed by disproportionation of $\text{Li}^+\text{-O}_2^-$ ($2\text{Li}^+\text{-O}_2^- \rightarrow \text{Li}_2\text{O}_2 + \text{O}_2$) and/or a second electron reduction of $\text{Li}^+\text{-O}_2^-$ to solid Li_2O_2 .^{68,69}

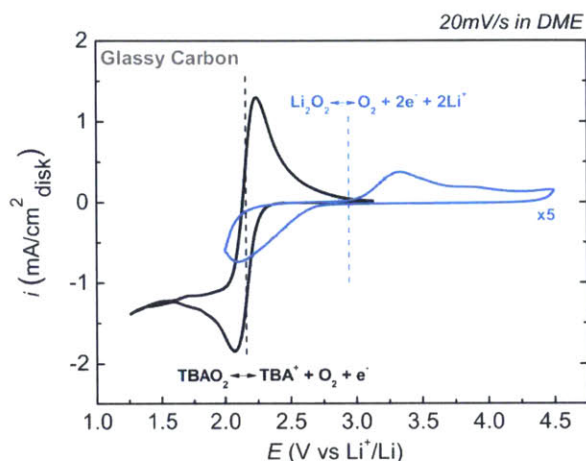


Figure 2-1. Cyclic voltammograms (CVs) of ORR/OER in 0.5 M TBAClO_4 in DME (black) and 0.1 M LiClO_4 in DME (blue, 5× increase in current for comparison) on glassy carbon at 20 mV/s.

A number of studies using ether-based electrolytes have shown that large Li_2O_2 particles and high discharge capacities are observed under low rates ($< 10 \mu\text{A}/\text{cm}^2$ in ethers^{70,71}), which has been attributed to the availability of soluble $\text{Li}^+\text{-O}_2^-$ at low overpotentials. The presence of $\text{Li}^+\text{-O}_2^-$ (Figure 2-2) during discharge is supported by spectroscopic evidence from *in situ* surface enhanced Raman Spectroscopy (SERS),^{66,67} Ultraviolet-Visible (UV-Vis)⁷² and Electron Paramagnetic Resonance (EPR)⁷³ spectroscopy. Abraham and co-workers^{68,74} have suggested that the stability of $\text{Li}^+\text{-O}_2^-$ increases with solvent donor number (DN), which measures the solvation enthalpy of the standard Lewis acid SbCl_5 in a given solvent (in kcal/mol).⁷⁵ This concept is supported by recent work,⁶⁷ which reports that increasing solvent DN leads to increased $\text{Li}^+\text{-O}_2^-$ solubility and capacities upon discharge.

Understanding how standard potentials of $O_2/Li^+-O_2^-$ change in different solvents and correlating the change with that of $O_2/TBA^+-O_2^-$ and $Li^+-O_2^-$ solubility is critical to control the kinetics and discharge product characteristics in Li- O_2 batteries. Unfortunately, unlike $O_2/TBA^+-O_2^-$, the equilibrium potentials and kinetics of the $O_2/Li^+-O_2^-$ couple in aprotic solvents, are not known. The fast kinetics of oxygen reduction to soluble O_2^- in the presence of weakly coordinating TBA^+ ($TBA^+ + O_2 + e^- \leftrightarrow TBA^+ - O_2^-$ in Figure 2-2a), which stands in contrast to the slow kinetics of O_2/Li_2O_2 (Figure 2-1), have been studied extensively.

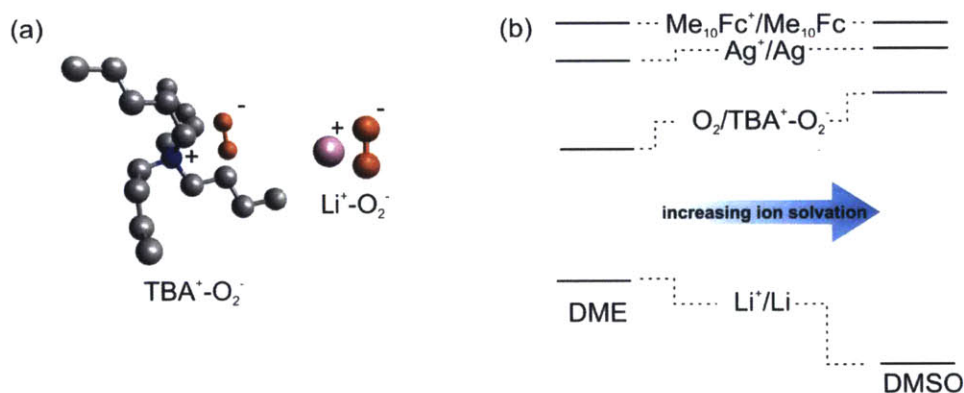


Figure 2-2. Schematic showing (a) $TBA^+-O_2^-$ and $Li^+-O_2^-$ complexes and (b) the effect of increasing O_2^- and Li^+ ion solvation from weakly to strongly solvating media (such as DME to DMSO) on $O_2/TBA^+-O_2^-$ and Li^+/Li redox potentials measured using an Ag/Ag^+ reference electrode and $Me_{10}Fc^+/Me_{10}Fc$ as a solvent independent redox reference.

Seminal work by Sawyer and co-workers in the 1980s has suggested that the increasing $O_2/TBA^+-O_2^-$ redox potential from pyridine to dimethylsulfoxide (DMSO) can be attributed to greater O_2^- solvation.⁷⁶ Greater O_2^- ion solvation increases the $O_2/TBA^+-O_2^-$ redox potential as O_2^- ions would be more stable in contrast to lowered Li^+/Li redox potential with increasing Li^+

solvation (Figure 2-2b). This trend is consistent with recent findings that the reversible potential of $O_2/TBA^+-O_2^-$ increases with larger solvent acceptor number (AN),⁷⁷ which measures the P-Nuclear Magnetic Resonance (NMR) shift induced by the solvent in the standard base triethylphosphine oxide⁷⁸ (an empirical measure of solvent acidity). Likewise, Li^+/Li potentials decrease with greater solvent DN (measured from the half-wave potential of the Li^+/Li couple measured against the solvent-independent bis(biphenyl)chromium redox couple⁷⁹). The potential of the $O_2/Li^+-O_2^-$ redox couple in different solvents, however, depends on the solvation of O_2^- as well as the coupling energy of Li^+ to O_2^- . This coupling, which is a Lewis acid-base interaction, is not straightforward to estimate from AN-dependent $O_2/TBA^+-O_2^-$ and DN-dependent Li^+/Li potentials. Indeed, not only do DN and AN have different units, they also do not provide quantitative solvation energies for Li^+ and O_2^- ions.

Here we first report increasing standard $O_2/TBA^+-O_2^-$ potentials with greater AN and decreasing Li^+/Li redox potentials with DN for a series of aprotic solvents, which are referenced to the solvent-independent decamethylferrocenium/decamethylferrocene ($Me_{10}Fc^+/Me_{10}Fc$) redox couple, which is stable against O_2^- , unlike ferrocenium (Fc^+) in the Fc^+/Fc couple.⁸⁰ The measured redox potentials of $O_2/TBA^+-O_2^-$ and Li^+/Li are in agreement with standard potentials computed using a mixed cluster-continuum model, which increases and decreases with greater computed solvation energy of O_2^- and Li^+ , respectively. Of significance, we show that greater Li^+ and O_2^- solvation correlates with weakened coupling strength of $Li^+-O_2^-$, which is supported by decreasing difference between measured $O_2/Li^+-O_2^-$ and $O_2/TBA^+-O_2^-$ standard potentials.

2.2 Experimental and Computational Methods

2.2.1 Electrochemical Cell and Electrode Preparation

Electrochemical measurements were performed in glass three-electrode cells (Chemglass, USA) with a Pine (Pine, USA) bipotentiostat. Working RDEs consisted either of a Pt or glassy carbon (GC) (5 mm diameter; Pine, USA) surface. Whereas the RDE is appropriate for probing species with lifetimes on the order of several minutes/hours, RRDE offers the advantage that products generated at the disk can be detected at the annular ring within tens of milliseconds after formation⁸¹ and can be used to study short-lived $\text{Li}^+\text{-O}_2^-$ species.⁸² RRDE experiments were performed using a GC disk surrounded by a gold ring with 6.5 mm internal diameter and 7.5 mm external diameter. The $\text{O}_2/\text{Li}^+\text{-O}_2^-$ redox potential was extrapolated from the ring potential, where the ring-to-disk charge ratio reached zero. All electrodes were polished to a 0.05 μm mirror-finish, ultra-sonicated in deionized water (18.2 $\text{M}\Omega\cdot\text{cm}$, Millipore) for 5 min and dried in a glass oven (Büchi B-585) at 70 °C for 8 hours before each experiment. Electrodes were kept in the vacuum oven and directly transferred to a water-free glovebox ($\text{H}_2\text{O} < 0.1$ ppm, Mbraun, USA) without exposure to the ambient.

Three-electrode cells consisted of a 5 mm-diameter GC disk as the working electrode, a Ni foam or lithium foil counter electrode and a quasi-reference electrode consisting of a silver wire immersed in 0.1 M TBAClO_4 (Sigma Aldrich) and 0.01 M AgNO_3 (BASi) in acetonitrile, separated from the electrolyte with a Vycor frit. RDE and RRDE experiments were performed in a water-free argon glovebox ($\text{H}_2\text{O} < 0.1$ ppm, $\text{O}_2 < 1\%$). The electrolyte solvents used were DMSO (Sigma Aldrich), dimethoxyethane (DME) (BASF, USA), acetonitrile (MeCN) (Sigma Aldrich), dimethylacetamide (DMA) (Sigma Aldrich) and dimethylformamide (DMF) (Sigma Aldrich).

LiClO₄ and TBAClO₄ salts were purchased from Sigma Aldrich and vacuum-dried at 100 °C for 8 hours prior to use, while Me₁₀Fc was purchased from Alfa Aesar and used as received.

2.2.2 Measurement of O₂/TBA⁺-O₂⁻ redox potentials in aprotic organic solvents

To determine the influence of electrolyte solvent on the oxygen reduction potentials, CVs were measured in O₂-saturated electrolyte containing TBAClO₄ salt and 2 mM of Me₁₀Fc, the potential of whose redox reaction ($Me_{10}Fc \leftrightarrow Me_{10}Fc^+ + e^-$) was solvent-independent. 0.1 M TBAClO₄ was used in DMSO, MeCN, DMA and DMF while a higher concentration of 0.5 M TBAClO₄ was used in DME due to its lower conductivity (Figure 2-3).

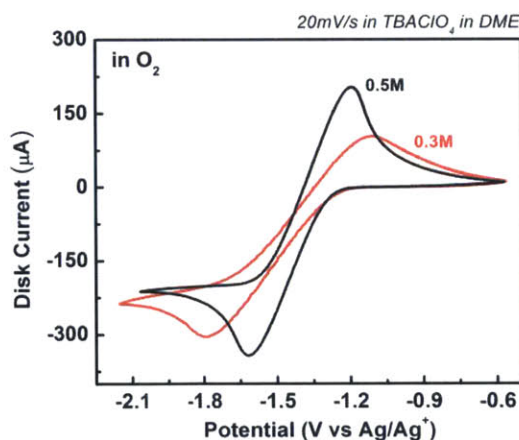


Figure 2-3. CVs at 20 mV/s showing reversible ORR/OER in oxygen-saturated electrolytes containing 0.3 M (red) and 0.5 M (black) TBAClO₄ in DME. CVs were obtained with an Ag/Ag⁺ electrode as reference. Polarization in 0.3 M show more resistive behavior than in 0.5 M.

The Ag⁺/Ag electrode was used as the reference electrode. In order to confirm that the presence of oxygen did not influence the Me₁₀Fc⁺/Me₁₀Fc redox reaction, or lead to decomposition

of $\text{Me}_{10}\text{Fc}^+$, CVs were first collected in Ar. CVs of the $\text{Me}_{10}\text{Fc}^+/\text{Me}_{10}\text{Fc}$ redox process under oxygenated conditions are identical to those obtained in Ar-saturated electrolyte in all solvents (Figure 2-4). Additionally, all CVs demonstrated quasi-reversibility of both redox processes for scan rates of 20, 50 and 100 mV/s (Figure 2-5).

The working electrode was prepared as described above, and then immersed into electrolyte that had been purged with Ar for 20 minutes. After steady-state CVs were obtained in argon at 20, 50 and 100 mV/s the cell was purged with O_2 for 20 min and similar CVs were obtained in O_2 -saturated electrolyte. $\text{O}_2/\text{TBA}^+-\text{O}_2^-$ and $\text{Me}_{10}\text{Fc}/\text{Me}_{10}\text{Fc}^+$ redox potentials were calculated from the midpoint of the cathodic and anodic peak potentials observed in the CV experiments $((E_{\text{cath}} + E_{\text{anod}})/2)$. $\text{O}_2/\text{TBA}^+-\text{O}_2^-$ redox potentials vs $\text{Me}_{10}\text{Fc}^+/\text{Me}_{10}\text{Fc}$ were corrected to standard potentials on the basis of different oxygen solubilities⁸³ in the solvents used (more details in Appendix A).

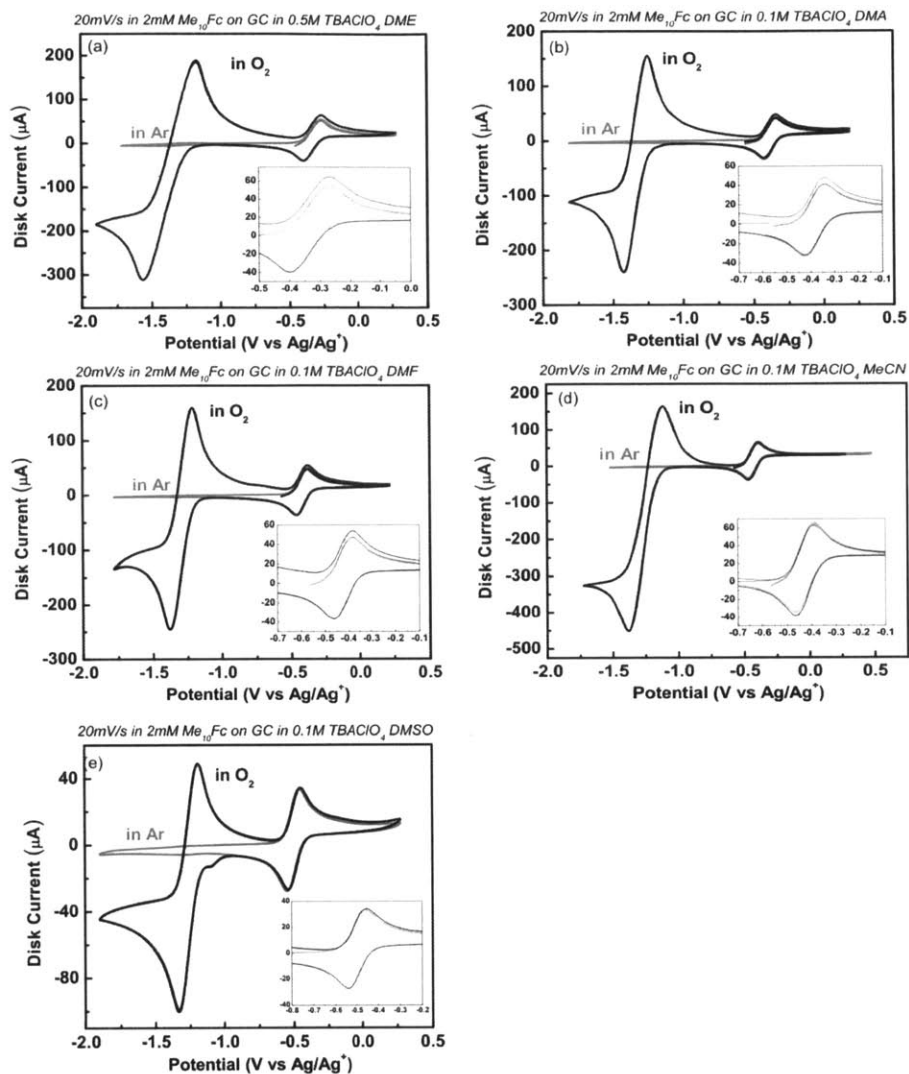


Figure 2-4. CVs showing O_2/O_2^- and $Me_{10}Fc/Me_{10}Fc^+$ redox reactions in argon and oxygen-saturated electrolytes containing 2mM $Me_{10}Fc$ in (a) 0.5 M $TBAClO_4$ in DME, 0.1 M $TBAClO_4$ in (b) DMA (c) DMF (d) MeCN and (e) DMSO. CVs were obtained at 20 mV/s with an Ag/Ag^+ electrode as reference.

2.2.3 Measurement of Li^+/Li redox potentials in aprotic organic solvents

The effect of electrolyte solvent on Li^+/Li redox potentials was examined by comparing experimental Li^+/Li redox potentials against the solvent-independent $\text{Me}_{10}\text{Fc}^+/\text{Me}_{10}\text{Fc}$ reference. This was performed in two stages: first the Li^+/Li potential vs Ag/Ag^+ was inferred from bulk Li plating and dissolution experiments using an Ag^+/Ag reference electrode.

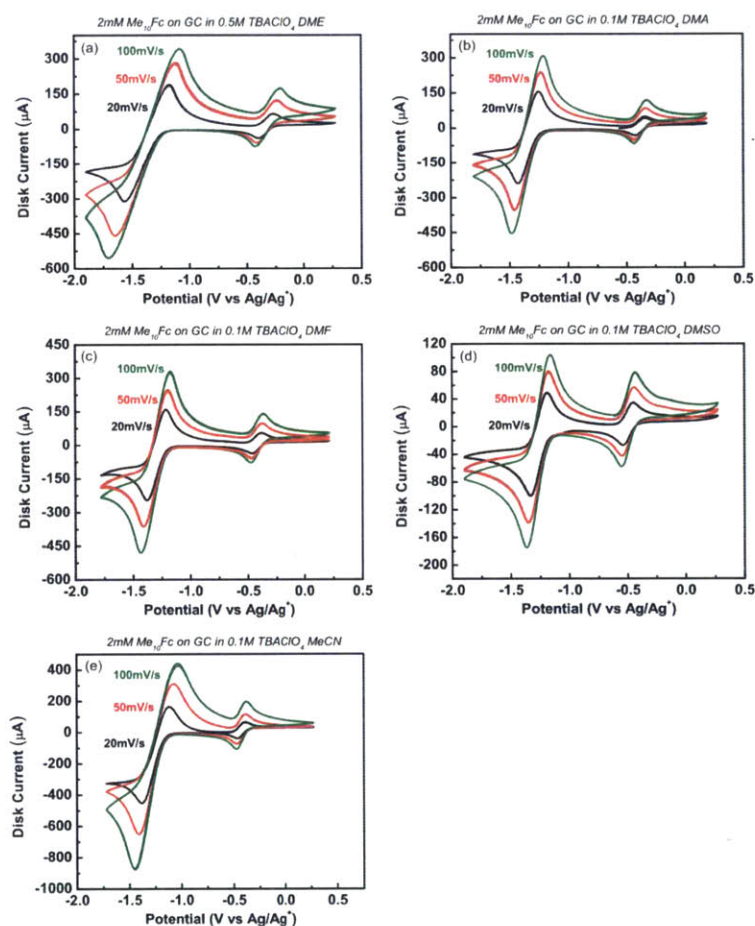


Figure 2-5. CVs at 20, 50 and 100 mV/s showing $\text{O}_2/\text{TBA}^+-\text{O}_2^-$ and $\text{Me}_{10}\text{Fc}/\text{Me}_{10}\text{Fc}^+$ redox reactions in oxygen-saturated electrolytes containing $2\text{mM Me}_{10}\text{Fc}$ in (a) 0.5M TBAClO_4 in DME, 0.1M TBAClO_4 in (b) DMA (c) DMF (d) DMSO and (e) MeCN. CVs were obtained with an Ag/Ag^+ electrode as reference.

This potential was then added to the Ag^+/Ag vs $\text{Me}_{10}\text{Fc}^+/\text{Me}_{10}\text{Fc}$ redox potentials previously obtained from direct CV measurements of the $\text{Me}_{10}\text{Fc}^+/\text{Me}_{10}\text{Fc}$ redox couple, in order to arrive at the Li^+/Li potential vs $\text{Me}_{10}\text{Fc}^+/\text{Me}_{10}\text{Fc}$. For the Li plating and dissolution experiments, a Pt working electrode was prepared as described previously and used as the working electrode, while lithium foil (Chemetall, USA) was used as the counter electrode, with the Ag^+/Ag reference electrode. CVs were performed at 50 mV/s in 0.1 M LiClO_4 in DMSO, DME, MeCN and DMA, where anodic and cathodic currents corresponded to bulk Li plating and removal respectively. The validity of this calibration was assessed against another method reported previously,⁸⁴ where the potential of the Ag reference electrode was measured against a strip of lithium foil at open circuit, upon immersion in electrolytes of 0.1 M LiClO_4 in DMSO, DME, MeCN and DMA (Table 2-1).

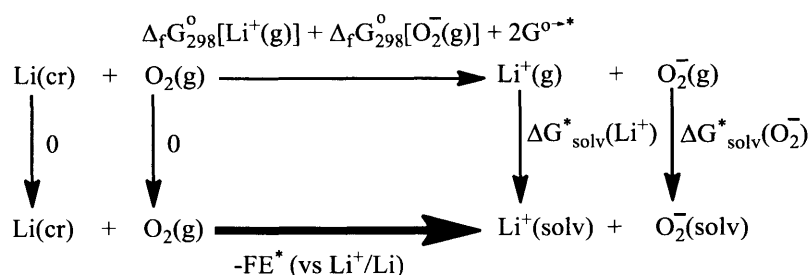
Table 2-1. Comparison of Ag^+/Ag potentials measured at open circuit against Li metal and from Li plating/dissolution experiments.

Electrolyte solvent	Stripping	Open Circuit Voltage
MeCN	3.22	3.23
DMSO	3.79	3.81
DMA	3.70	3.71
DME	3.32	3.34
DMF		3.67

In further support of this technique, direct measurement of the Me₁₀Fc⁺/Me₁₀Fc redox reference in 1 M LiNO₃ in DMA using a Li metal reference electrode (Figure A 1 in Appendix A) yielded a potential (3.25 V vs Li⁺/Li) that is in exact agreement with the equivalent value obtained from adding the potential of Me₁₀Fc⁺/Me₁₀Fc vs Ag⁺/Ag (-0.39 V) to Ag⁺/Ag vs Li⁺/Li (3.64 V from Table 2-1). Since DMF reacts violently with Li metal, only the open circuit voltage of Ag⁺/Ag vs Li metal was checked and used. Li⁺/Li potentials were corrected to standard potentials due to LiClO₄ concentrations of 0.1 rather 1 M of LiClO₄ dissolved in the different solvents (see Appendix A for more details).

2.2.4 Calculation of oxygen reduction potentials in aprotic organic solvents

Oxygen reduction potentials versus the Li⁺/Li scale were calculated using the thermodynamic cycle shown in Scheme S1.



Scheme 2-1. Thermodynamic cycle for the calculation of oxygen reduction potentials vs Li⁺/Li scale.

Based on Scheme 2-1, we can write

$$-FE^*(\text{vs Li}^+/\text{Li}) = \Delta_f G_{298}^\circ[\text{Li}^+(\text{g})] + \Delta_f G_{298}^\circ[\text{O}_2^-(\text{g})] + 2\Delta G^{\circ \rightarrow *} + \Delta G_{\text{solv}}^*[\text{Li}^+] + \Delta G_{\text{solv}}^*[\text{O}_2^-] \quad [2-1]$$

where $\Delta_f G_{298}^\circ[\text{Li}^+(\text{g})]$ and $\Delta_f G_{298}^\circ[\text{O}_2^-(\text{g})]$ are the standard gas-phase free energies of formation of Li^+ and O_2^- , respectively, F is Faraday's constant, E^* is the standard reduction potential vs. Li^+/Li , and $\Delta G_{\text{solv}}^*(X^\pm)$ is the solvation free energy of $X^\pm = \text{Li}^+$ and O_2^- . $\Delta G^{\circ \rightarrow *}$ represents the conversion of an ideal gas at standard state of 1 atm (24.46 L mol^{-1}) to an ideal solution standard state of 1 M (1 mol L^{-1}).⁸⁵

$$\Delta G^{\circ \rightarrow *} = RT \ln(24.46) = 1.89 \text{ kcal/mol} \quad (T = 298.15 \text{ K}) \quad [2-2]$$

A convenient practice in theoretical calculations of standard redox potentials is to use a free electron in vacuum as the reference state for the electron.^{86,87} Adopting the zero level as the reference for the electron energy⁸⁸ in vacuum (rather than the Li^+/Li redox energy) and applying the reasoning used to derive equation [2-1] the absolute oxygen reduction potential can be written as

$$-FE^*(\text{abs}) = \Delta_f G_{298}^\circ[\text{O}_2^-(\text{g})] + \Delta G^{\circ \rightarrow *} + \Delta G_{\text{solv}}^*[\text{O}_2^-] \quad [2-3]$$

It is important to note that $\Delta G_{\text{solv}}^*[\text{O}_2^-]$ used in equations [2-1] and [2-3] refers to the absolute/intrinsic solvation energy of the O_2^- ion, without the additional electrostatic contributions from the vacuum/solvent interface i.e. the surface potential of the solvent cluster.⁸⁹ This assumption appears to be universally accepted as part of the definition of the absolute electrode potential, and is justified in the present study since the ion-(solvent)_n clusters employed in the present work for the calculation of $\Delta G_{\text{solv}}^*(\text{Li}^+)$ and $\Delta G_{\text{solv}}^*(\text{O}_2^-)$ are too small to reach the point of surface potential development ($n \leq 8$).^{86,89} An equation analogous to that for absolute oxygen

reduction (equation [2-3]) can be written for Li oxidation, with the important qualification that the free energy of Li⁺ formation ($\Delta_f G_{298}^\circ[\text{Li}_{(g)}^+]$) is comprised of the free energy of Li metal sublimation as well as gas-phase Li ionization.

Absolute single-ion solvation free energies in equation [2-1] were calculated using the thermodynamic cycle (cluster cycle) shown in Figure 2-6a.^{89,90} Solute-solvent interactions in the first solvation shell were computed explicitly while solvent effects beyond the first solvation shell were approximated using a dielectric, Poisson-Boltzmann continuum model. Previous studies indicated that due to a favorable compensation of errors the cluster cycle with (solvent)_n cluster as a reagent provides more accurate solvation free energies than the monomer cycle with n distinct solvent molecules as reagents.⁸⁹ From Figure 2-6a, $\Delta G_{\text{solv}}^*(X^{m\pm})$ can be expressed as the algebraic sum of the gas-phase complexation free energy ($\Delta G_{g,\text{bind}}^\circ$), the difference in the solvation free energy for $[X(\text{solvent})_n]^{m\pm}$ and (solvent)_n clusters calculated using a dielectric continuum model, and the standard state/concentration correction terms:^{85,89}

$$\Delta G_{\text{solv}}^*(X^{m\pm}) = \Delta G_{g,\text{bind}}^\circ + \Delta G_{\text{solv}}^*([X(\text{Solvent})_n]^{m\pm}) - \Delta G_{\text{solv}}^*(\text{Solvent})_n - \Delta G^{\circ \rightarrow *}$$

$$- RT \ln \left(\frac{[\text{Solvent}]_n}{n} \right)$$

Here, $\Delta G^{\circ \rightarrow *}$ is defined as in equation [2-2] and $RT \ln([\text{solvent}]/n)$ is the free energy change of 1 mol of (solvent)_n ideal gas from [solvent]/n M liquid state to 1 M standard state in solution. According to equation [2-4], the accuracy of single-ion solvation free energies depends on (i) the accuracy of DFT methods for predicting complexation free energies in the gas phase, (ii) the accuracy of dielectric continuum models for predicting solvation free energies of solvent

molecules, (iii) adequate sampling of solvent and solute-solvent clusters, and (iv) reasonable convergence of results with cluster size n .

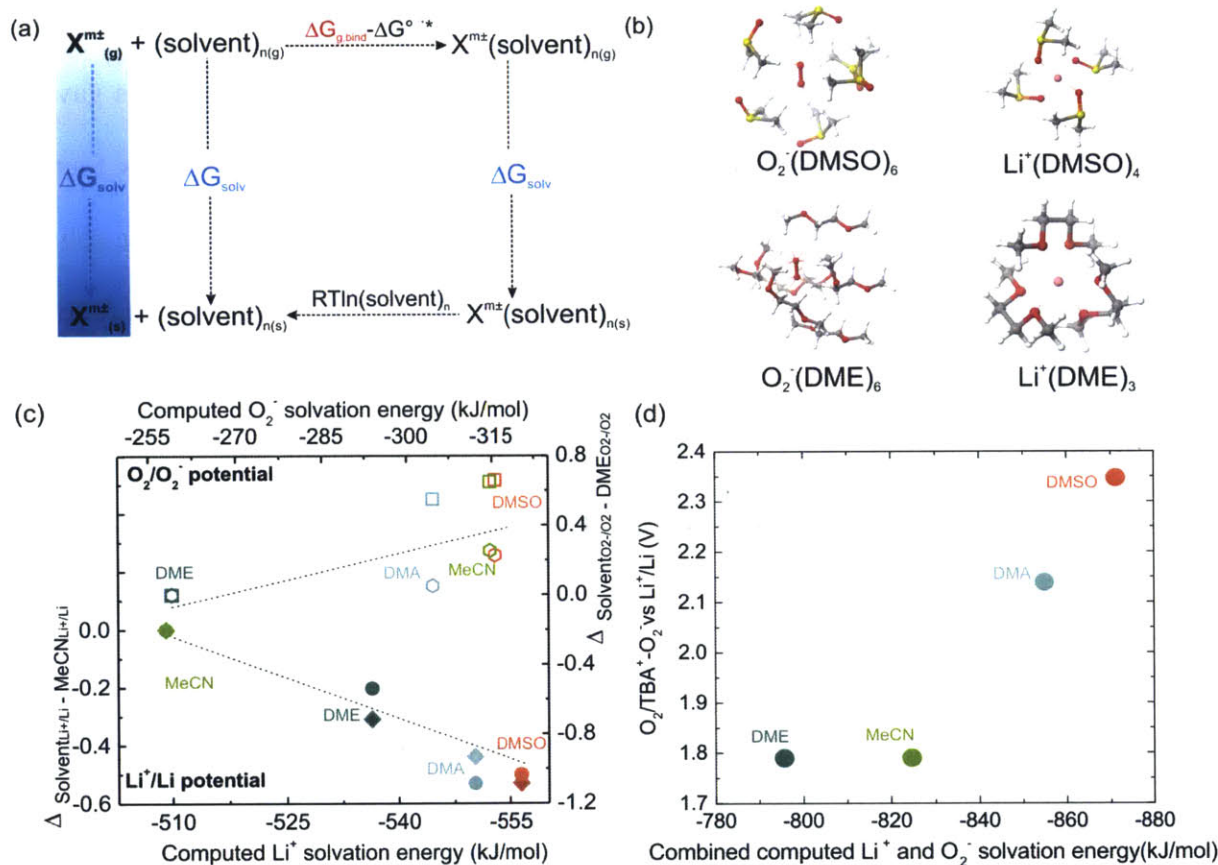


Figure 2-6. (a) Thermodynamic cycle for the calculation of Li^+ or O_2^- ion solvation. (b) Structures of the most stable $\text{X}(\text{Solvent})_{\text{n}}$ clusters (Solvent = DMSO, DME; $\text{X} = \text{Li}^+, \text{O}_2^-$, $n = 4-6$) obtained at the M06-L/6-311++G**//B3LYP/6-31G** level. Solvation effects on relative cluster stability are included using the dielectric continuum model with scaled (by 1.35) solute van der Waals radii. (c) Comparison of standard experimental (hexagons) and calculated (squares) O_2/O_2^- and experimental (circles) and calculated (diamonds) Li^+/Li redox potentials against computed Li^+ and O_2^- solvation energies of each solvent. All Li^+/Li and O_2/O_2^- potentials are plotted with respect to

MeCN and DME respectively and Nernstian corrections were applied to Li^+/Li potentials, while O_2 solubility corrections were applied to the $\text{O}_2/\text{TBA}^+-\text{O}_2^-$ potentials. (d) Standard experimental redox potentials of $\text{O}_2/\text{TBA}^+-\text{O}_2^-$ vs Li^+/Li against combined Li^+ and O_2^- solvation energy.

A previous investigation⁹⁰ of the complexation of superoxide and alkali metal ions with MeCN and ethers in the gas phase found that the M06-L and M06 density functionals gave the best performance against the experimental data. Scaling the solute atomic radii was found to improve the accuracy of solvation free energy calculations for small molecules in aprotic solvents, as shown in Figure A2 in Appendix A. Conformational sampling of solute-solvent and pure solvent clusters was performed using the Monte-Carlo sampling algorithm (called BLENDS)^{91,92} to generate 40 initial cluster configurations. The energies for MeCN and ion-MeCN clusters were taken from previous work.⁹⁰ Some initial configurations were also built upon visual inspection and conformational rearrangement of the optimized clusters. Single-ion solvation calculations are reported using the lowest-energy clusters in solution (ranked by electronic energies in the solvent reaction field). The presence of the full first solvation shell around singly charged and neutral ionic solutes has been shown^{89,90,93} to be sufficient for providing reasonably converged results with cluster size and good agreement with experiment.

2.3 Results and Discussion

2.3.1 Measured and Computed $\text{O}_2/\text{TBA}^+-\text{O}_2^-$ and Li^+/Li standard potentials

We show that measured standard potentials of $\text{O}_2/\text{TBA}^+-\text{O}_2^-$ and Li^+/Li scale with computed solvation energy of O_2^- and Li^+ ions. First, the use of higher AN solvents, indicative of

greater $\text{TBA}^+\text{-O}_2^-$ solvating ability, led to higher $\text{O}_2/\text{TBA}^+\text{-O}_2^-$ redox potentials, as indicated in Figure 2-2b and previous work.^{76,77} Figure 2-7a shows cyclic voltammograms (CVs) obtained in O_2 -saturated DMSO, 1,2-dimethoxyethane (DME), acetonitrile (MeCN) and dimethyl acetamide (DMA)-based electrolytes, which contained no Li^+ ions but rather weakly coordinating TBA^+ and Me_{10}Fc . Similar measurements were performed in dimethyl formamide (DMF) (see Figure 2-4).

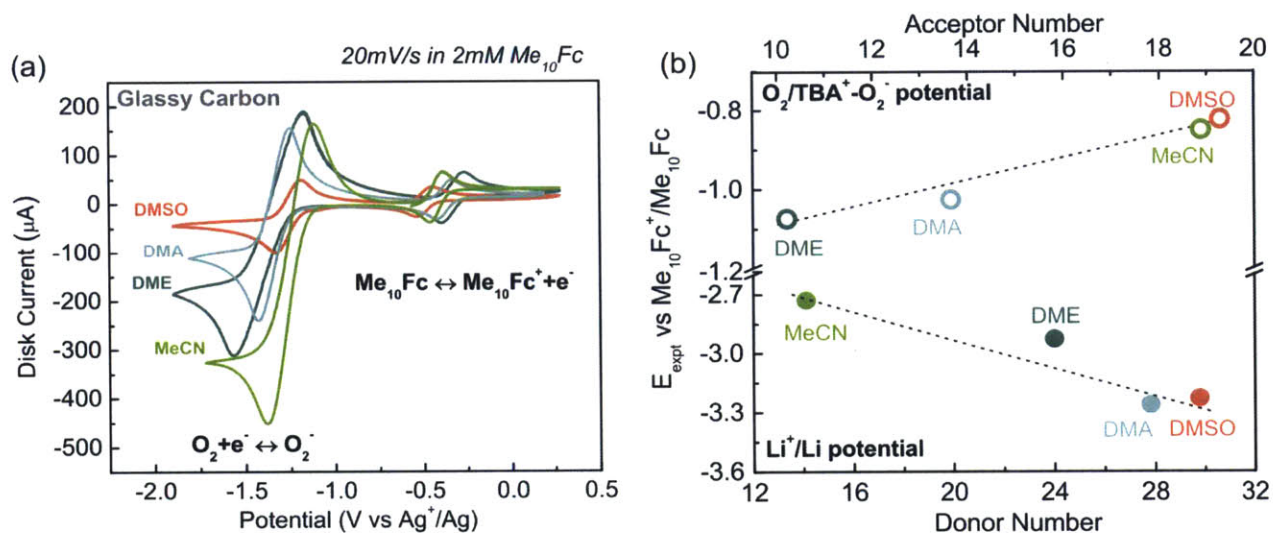


Figure 2-7. (a) Steady-state CVs of $\text{O}_2/\text{TBA}^+\text{-O}_2^-$ and $\text{Me}_{10}\text{Fc}^+/\text{Me}_{10}\text{Fc}$ redox reactions collected at 20 mV/s in oxygen-saturated electrolytes containing 2 mM Me_{10}Fc in 0.5 M TBAClO_4 in DME, 0.1 M TBAClO_4 in DMA and DMSO obtained with an Ag/Ag^+ reference electrode and Ni foam counter electrode. (b) Experimental standard $\text{O}_2/\text{TBA}^+\text{-O}_2^-$ and Li^+/Li redox potentials vs $\text{Me}_{10}\text{Fc}^+/\text{Me}_{10}\text{Fc}$ plotted against acceptor and donor numbers of each solvent. The lower cathodic/anodic currents of $\text{Me}_{10}\text{Fc}^+/\text{Me}_{10}\text{Fc}$ can be attributed to lower diffusivity and solubility of Fc compared to those of oxygen.^{68,94}

These media were chosen because they are kinetically stable against superoxide^{76,95,96} and have been proposed as candidate electrolyte solvents for Li-O_2 batteries.^{38,41,49} Both $\text{O}_2/\text{TBA}^+\text{-O}_2^-$

(centered ~ -1250 mV vs Ag/Ag⁺) and Me₁₀Fc⁺/Me₁₀Fc (centered at ~ -300 mV vs Ag/Ag⁺) redox processes were reversible, and shifted in different solvents, as shown in Figure 2-7a. As the redox potential of Me₁₀Fc⁺/Me₁₀Fc is solvent-independent,⁸⁰ the redox potentials of O₂/TBA⁺-O₂⁻ referenced to Ag/Ag⁺ in different solvents were then scaled with that of Me₁₀Fc⁺/Me₁₀Fc. Standard O₂/TBA⁺-O₂⁻ redox potentials were found to increase with greater AN, where the largest difference of ~ 0.2 V was noted between DME and DMSO (Figure 2-7b). The standard O₂/TBA⁺-O₂⁻ potentials referenced to Me₁₀Fc⁺/Me₁₀Fc linearly correlate with solvent AN ($R^2 = 0.98$), which is in agreement with previous correlation between AN and O₂/TBA⁺-O₂⁻ vs Fc⁺/Fc ($R^2 = 0.99$).⁷⁷ The correlations established using these solvent-independent references are much improved in comparison to the trend obtained using the solvent-dependent Ag/Ag⁺ reference reported by Sawyer *et al.*⁷⁶ ($R^2 = 0.75$).

Li⁺/Li redox potentials were found to decrease with greater solvent DN (Figure 2-7b), in accordance with the trend suggested in Figure 2-2b. The Li plating/stripping potentials were first obtained from CV measurements referenced to Ag⁺/Ag, which was then referenced to the Me₁₀Fc⁺/Me₁₀Fc potential using the scaling found between Me₁₀Fc⁺/Me₁₀Fc and Ag⁺/Ag. CVs of bulk Li plating and stripping from the Pt working electrode in 0.1 M LiClO₄ in DMSO, DME, MeCN and DMA are shown in Figure 2-8a, which are characterized by a sharp rise in cathodic current during the negative scan, attributable to Li deposition, and an anodic peak on the reverse scan, indicating Li removal from the Pt surface. The redox potential of Li⁺/Li ($Li^+ + e^- \leftrightarrow Li$) reaction was defined from the potential at zero current (i.e. where neither Li plating nor removal occurs) during the anodic scan.

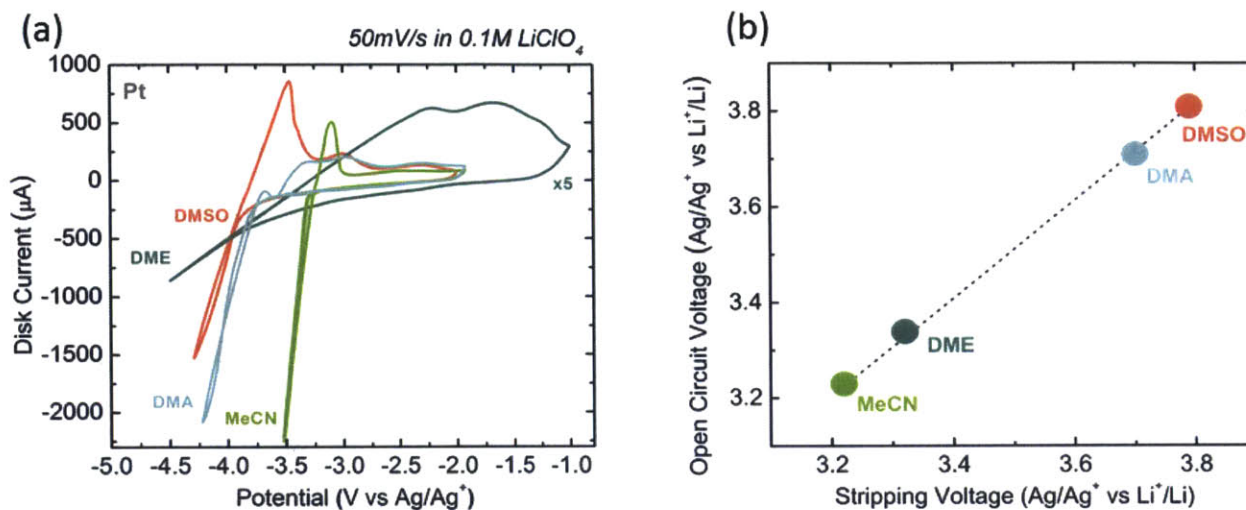


Figure 2-8. (a) CVs obtained at 50 mV/s showing bulk Li plating and dissolution using a Pt working electrode in 0.1 M LiClO₄ in DMSO, DMA, MeCN and DME (5× increase in current for comparison) using a Li metal counter electrode and Ag⁺/Ag reference. The redox potential of Li⁺/Li was found by the dotted lines, extrapolating the point of zero current during the anodic scan to the potential axis. (b) Comparison between Ag⁺/Ag vs Li⁺/Li potentials obtained from Li stripping experiments and those from open circuit potentials between the Ag quasi-reference electrode and Li metal immersed in the electrolyte. Both methods are in excellent agreement ($R^2 = 1.004$).

Decreasing Li⁺/Li redox potentials with greater DN obtained from this method is in accordance with the trend obtained using a methodology we reported previously,⁸⁴ for which the Ag⁺/Ag quasi-reference electrode was calibrated against the Li⁺/Li scale using the open-circuit voltage measured vs Li metal immersed in the electrolyte (Figure 2-8b). Reported higher Li-O₂ discharge potentials in DMSO than in ether-based solvents such as tetraglyme (200 mV)⁹⁷ and DME (~250 mV)⁹⁸ can be attributed largely to lower Li⁺/Li redox in DMSO by 300 mV than DME (Figure 2-7b).

Further evidence for increasing $O_2/TBA^+-O_2^-$ and decreasing Li^+/Li redox potentials with greater solvation came from single ion solvation energies of O_2^- and Li^+ ions in DMSO, DME, MeCN and DMA (Figure 2-6) computed using the mixed cluster-continuum model. The computed solvation free energies of individual O_2^- and Li^+ ions in these solvents were referenced to the ion free energy in the gas phase and computed following the scheme shown in Figure 2-6a. The most stable ion-solvent clusters for O_2^- in DMSO and DME are shown in Figure 2-6b as examples, from which single-ion solvation free energies were obtained. O_2^- in six-fold coordination, $[O_2(Solvent)_6]^-$, on average forms 12 bonds with C-H donor groups of DMSO, DME, MeCN and DMA. The computed solvation free energy, $\Delta G_{solv}^*(O_2^-)$, was found to increase with greater AN ($R^2 = 0.81$), from -259 kJ/mol in DME to -315 kJ/mol in DMSO. It is important to note that the continuum solvent model without the explicit first solvation shell (only taking in account of the medium dielectric constant changes) overestimates the values of $\Delta G_{solv}^*(O_2^-)$ for all solvents and cannot be used to differentiate the solvation energetics of O_2^- among DMSO, MeCN and DMA. The absolute oxygen reduction potential (O_2/O_2^-) was computed with respect to electron energy in vacuum, using $-FE^*(abs) = \Delta_f G_{298}^\circ [O_{2(g)}^-] + \Delta G^{\circ \rightarrow * } + \Delta G_{solv}^* [O_2^-]$, where $\Delta_f G_{298}^\circ [O_{2(g)}^-]$ and $\Delta G^{\circ \rightarrow * }$ are solvent-independent parameters related to gas-phase ionization and standard state correction, respectively. Computed solvent-dependent changes in the O_2/O_2^- redox potential referenced to DME show a good agreement with, but are consistently higher than measured differences of $O_2/TBA^+-O_2^-$, as shown in Figure 2-6c. This could originate from a combination of computational inaccuracy and computed O_2/O_2^- potentials not accounting for $TBA^+-O_2^-$ pairing which, although weak, would partially neutralize and therefore reduce the effective solvation of O_2^- in experimental measurements.

The most stable Li⁺-solvent clusters with cluster size n = 4 for DMSO and 3 for DME are shown in Figure 2-6b, from which single-ion solvation free energies were obtained. The computed solvation free energy, $\Delta G^*_{\text{solv}}(\text{Li}^+)$, was found to linearly decrease with greater DN ($R^2 > 0.99$), from -509 kJ/mol in MeCN to -557 kJ/mol in DMSO, as shown in Figure 3c. On the other hand, $\Delta G^*_{\text{solv}}(\text{Li}^+)$ does not scale with AN. Our calculated solvation free energies of Li⁺ in MeCN and DMSO are in agreement with previously reported experimental studies on ion-solvent clusters^{89,90} (Table A 2 in Appendix A). It should also be mentioned that the continuum model without explicitly accounting for the first solvation shell of Li⁺ does not show any differences in the solvation free energies of Li⁺ between MeCN and DMSO. Moreover, the computed absolute potential of Li⁺/Li decreased linearly with lower $\Delta G^*_{\text{solv}}(\text{Li}^+)$, which was computed using $-FE^*(\text{abs}) = \Delta_f G_{298}^\circ[\text{Li}^+_{(g)}] + \Delta G^{\circ \rightarrow *}_{\text{solv}} + \Delta G^*_{\text{solv}}[\text{Li}^+]$, with $\Delta_f G_{298}^\circ[\text{Li}^+_{(g)}]$ and $\Delta G^{\circ \rightarrow *}$ being solvent independent variables related to gas-phase ionization (including the Li sublimation energy) and standard state correction, respectively. Remarkably, computed solvent-dependent changes in the Li⁺/Li redox potential referenced to MeCN showed an excellent agreement compared with measured differences, as shown in Figure 2-6c.

As greater Li⁺ solvation lowers the Li⁺/Li potential while greater O₂⁻ solvation increases the O₂/O₂⁻ potential, solvents that strongly solvate *both* Li⁺ and O₂⁻ have high O₂/O₂⁻ potentials vs Li⁺/Li potentials, as shown in Figure 2-6c. Indeed, the O₂/TBA⁺-O₂⁻ redox potentials referenced to the Li⁺/Li scale increased with greater combined solvation of O₂⁻ and Li⁺ (Figure 2-6d), and were in close agreement with computed standard oxygen reduction potential of O₂/O₂⁻ vs Li⁺/Li (**Table A 4** and **Table A 5** in Appendix A), and previous experimental findings reporting higher O₂/TBA⁺-O₂⁻ redox potentials vs Li⁺/Li of 2.25²⁷ and 2.37⁶⁸ V in DMSO, compared to ~2.0 V for DME, MeCN⁶⁸ and ionic liquids.⁹⁹

2.3.2 Redox potential of $O_2/Li^+-O_2^-$ and coupling strength and solubility of $Li^+-O_2^-$

Solvent-dependent $O_2/Li^+-O_2^-$ redox potentials in Li^+ -containing DMSO, DME, DMA and DMF were estimated using chronoamperometric rotating ring disk electrode (RRDE) measurements. The disk was held at a potential to reduce O_2 under rotation at 900 rpm while the ring was held at discrete potentials to oxidize soluble intermediate species that diffused from the disk to the ring (Figure 2-9).

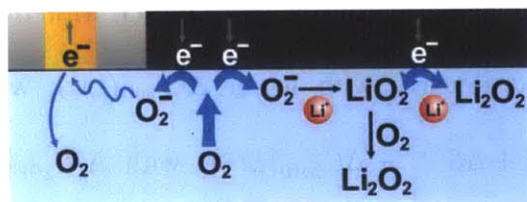


Figure 2-9. Schematic showing sectional view of RRDE during Li-ORR. Superoxide species are convected to the Au ring and oxidized, or converted to Li_2O_2 at the disk either by disproportionation or successive electron transfer.

Ring current transients measured from 3.50 to 2.76 V vs Li^+/Li (Figure 2-10a) while the disk potential was kept at 2.6 V vs Li^+/Li (Figure 2-10b) in DMSO are shown as an example (those for other solvents in Figure A3 in Appendix A). Ring currents were found to decrease with reducing potentials from 3.7 V to 2.7 V vs Li^+/Li for all solvents examined, which can be attributed to the ring potential approaching the equilibrium potential for soluble intermediate oxidation. We hypothesize that soluble ORR intermediates oxidized on the ring are $Li^+-O_2^-$ -like species. This hypothesis is supported by previous *in situ* Electrochemical Quartz Microbalance¹⁰⁰ (EQCM) analysis and SERS^{66,67} studies. Of significance to note is that the appearance of a peak at 1137 cm^{-1}

DMF at ring potentials between 2.75 and 3.70 V vs Li^+/Li . The RRDE was rotated at 900 rpm for all measurements (d) Relationship between standard redox potentials for $\text{O}_2/\text{TBA}^+-\text{O}_2^-$ (circles) and $\text{O}_2/\text{Li}^+-\text{O}_2^-$ (diamonds) vs Li^+/Li (filled symbols) and $\text{Me}_{10}\text{Fc}^+/\text{Me}_{10}\text{Fc}$ (open symbols) and the total solvation energy for Li^+ and O_2^- ions calculated from a mixed cluster-continuum model for each solvent. Nernstian corrections were applied to Li^+/Li potentials, while O_2 solubility corrections were applied to the $\text{O}_2/\text{TBA}^+-\text{O}_2^-$ potentials.

The standard $\text{O}_2/\text{Li}^+-\text{O}_2^-$ potentials extrapolated from chronoamperometric measurements of the ring/disk charge ratio are shown in Figure 2-10c, and reveal increasing $\text{O}_2/\text{Li}^+-\text{O}_2^-$ potentials in the order from DMSO, DMA, DMF to DME. $\text{O}_2/\text{Li}^+-\text{O}_2^-$ potentials in MeCN could not be measured due to very low ring currents, which fall within experimental uncertainty as a result of negligible solubility of Li^+-O_2^- in MeCN (see Figure A4e in Appendix A), in agreement with previous RRDE studies.^{67,98,103} Standard potentials were obtained by correcting extrapolated values in Figure 5d for oxygen solubility and Li^+ concentration (see Appendix A). Of significance to note is that standard $\text{O}_2/\text{TBA}^+-\text{O}_2^-$ potentials increased with increasing computed combined solvation of O_2^- and Li^+ (Figure 2-10d). This resulted in a reduction in the difference between standard $\text{O}_2/\text{TBA}^+-\text{O}_2^-$ and $\text{O}_2/\text{Li}^+-\text{O}_2^-$ potentials with increasing combined solvation, which is in agreement with the trend in computed $\text{O}_2/\text{Li}^+-\text{O}_2^-$ and O_2/O_2^- redox potentials found in DMSO, DME, MeCN and DMA (Table A 6 in Appendix A). We note that although experimental standard $\text{O}_2/\text{Li}^+-\text{O}_2^-$ redox potentials would be expected to increase with combined solvation energy of Li^+ and O_2^- , they were found to decrease in this study. This observation can be attributed to additional contributions to the energetics of Li^+-O_2^- formation beyond solvation, such as the formation of Li^+-O_2^- aggregates or Li^+-O_2^- species adsorbed to the Au ring, as previously noted.

The reduction in the difference between standard $O_2/TBA^+-O_2^-$ and $O_2/Li^+-O_2^-$ potentials with increasing combined solvation can be attributed to increasing solvation of Li^+ and O_2^- and thus decreasing coupling energy of solvated Li^+ binding to O_2^- . The increase in the coupling energy of $Li^+-O_2^-$ relative to $TBA^+-O_2^-$, described as the Gibbs free energy of $Li^+ + TBA^+-O_2^- \rightarrow Li^+-O_2^- + TBA^+$, can be estimated from the difference between standard potentials of $O_2/Li^+-O_2^-$ and $O_2/TBA^+-O_2^-$ obtained from RDE and RRDE measurements (**Table A 7** in Appendix A). Interestingly, the $Li^+-O_2^-$ coupling energy gain decreased with increasing combined computed solvation energy of Li^+ and O_2^- ions, as shown in **Figure 2-11a**. For example, the difference between standard $O_2/Li^+-O_2^-$ and $O_2/TBA^+-O_2^-$ redox potentials in DME is 1.24 V, yielding $Li^+-O_2^-$ coupling of -120 kJ/mol. In contrast, smaller $Li^+-O_2^-$ coupling energy of -21 kJ/mol in DMSO and -47 kJ/mol in DMA were found.

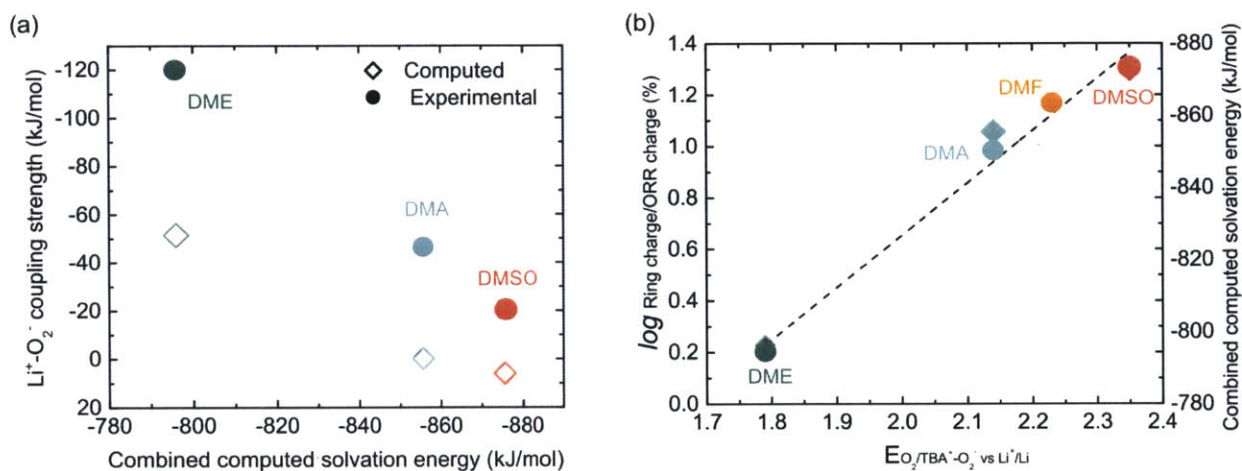


Figure 2-11. Comparison between (a) combined computed solvation energy of Li^+ and O_2^- ions in DMSO, DME and DMA and computed (diamonds) and experimental (circles) $Li^+-O_2^-$ coupling energies and (b) $O_2/TBA^+-O_2^-$ vs Li^+/Li redox potentials with the logarithm of ring-to-disk charge during Li-ORR (circles) and combined computed solvation energy of Li^+ and O_2^- ions in DMSO,

DME, DMA and DMF (diamonds). Dotted line shows linear regression through experimental data, $R^2 = 0.98$.

$\text{Li}^+\text{-O}_2^-$ coupling energies obtained from experimental $\text{O}_2/\text{TBA}^+\text{-O}_2^-$ and $\text{O}_2/\text{Li}^+\text{-O}_2^-$ redox potentials in this study are considerably more negative than those from previous work based on thermochemical data of solid $\text{Li}^+\text{-O}_2^-$ ⁶⁷ which does not take into consideration $\text{Li}^+\text{-O}_2^-$ solvation, resulting in weak coupling in DME (-25 kJ/mol) and thermodynamically unfavorable coupling for DMSO (20 kJ/mol). The thermodynamically favorable coupling for $\text{Li}^+\text{-O}_2^-$ is supported by observations that Li_2O_2 readily forms upon the addition of a Li^+ salt to superoxide-containing suspensions of DME and DMSO.^{40,102,104,105}

We find that increasing O_2^- and Li^+ solvation, as expressed by $\text{O}_2/\text{TBA}^+\text{-O}_2^-$ redox potentials vs Li^+/Li , increases the solubility of $\text{Li}^+\text{-O}_2^-$ in the solvent, as shown in **Figure 2-11b**. $\text{Li}^+\text{-O}_2^-$ solubility was compared using the logarithm of the ring-to-disk charge ratio obtained during ORR from RRDE measurements with the ring kept at 3.5 V vs Li^+/Li . $\text{Li}^+\text{-O}_2^-$ solubility was found to increase linearly (DME < DMA < DMF < DMSO) with combined computed solvation energies of Li^+ and O_2^- , and measured (**Figure 2-11b**) and computed (Appendix A) $\text{O}_2/\text{TBA}^+\text{-O}_2^-$ redox potentials vs Li^+/Li . A previously reported correlation between $\text{Li}^+\text{-O}_2^-$ solubility and DN⁶⁷ can be attributed to the fact that the combined computed solvation energy is dominated by computed Li^+ solvation energies (which scales with DN) as computed Li^+ solvation energies are considerably higher than those of O_2^- . However, considering Li^+ solvation (or DN) alone cannot explain trends in the $\text{Li}^+\text{-O}_2^-$ solubility for solvents with similar DN's but different AN's such as DMF (DN = 26.6 and AN = 16.0) than DMA (DN = 27.8 and 13.6, where greater $\text{Li}^+\text{-O}_2^-$ solubility observed for DMF and DMA cannot be explained by DN (Figure A5 in Appendix A). Extending this understanding to non-aqueous Na- and K- O_2 electrochemistry, one

would expect that the solubility of $\text{Na}^+\text{-O}_2^-$ and $\text{K}^+\text{-O}_2^-$ would not scale with DN as well, as Na^+ and K^+ are weaker Lewis acids than Li^{+106} and will be solvated less strongly. This is supported by a recent computational study of de-solvation energies of Li^+ and Na^+ in 27 organic solvents,¹⁰⁷ which found that Na^+ de-solvation energies were on average 20% less than Li^+ , implying weaker Na^+ solvation in non-aqueous solvents. Similarly, computed gas-phase binding energies of Na^+ and K^+ to tetrahydrofuran have been reported to be much less than that for Li^+ ,¹⁰⁸ and comparable to the computed solvation energies of O_2^- , $\Delta G^*_{\text{solv}}(\text{O}_2^-)$, found in this study.

Understanding and controlling the solvation and coupling of O_2^- and Li^+ ions has far-reaching implications for developing reversible Li- O_2 battery electrochemistry. Increasing $\text{Li}^+\text{-O}_2^-$ solubility is critical to achieve high discharge capacities from increasing filling of pores with Li_2O_2 solids during discharge and influences the morphologies of Li_2O_2 particles.^{13,67,70,71,109} However, solvents with increasing solvation power of O_2^- , reduced coupling of O_2^- and Li^+ ions and increased $\text{Li}^+\text{-O}_2^-$ solubility such as DMSO can be more subject to superoxide attack and decrease solvent stability in Li- O_2 batteries.^{37,110,111} This argument is supported by increasing computed $\Delta G^*_{\text{solv}}(\text{O}_2^-)$ with decreasing computed pKa of solvents (in DMSO) (Table A 3 in Appendix A), and previous findings which established a correlation between solvent AN and DN, and pKa, where solvents with higher $\text{Li}^+\text{-O}_2^-$ solubility – promoting Li_2O_2 toroid formation - are more susceptible to proton abstraction by O_2^- .¹¹² However, as Li^+ solvation structures can vary greatly among similar solvents (e.g. glymes),^{113,114} and different classes of solvents such as ionic liquids,¹¹⁵ caution should be exercised and further studies are needed to examine the influence of the solvation and coupling of O_2^- and Li^+ ions on solvent stability and to inform rational design of solvents optimized for high energy densities on discharge and high solvent stability.

2.4 Conclusions

This chapter has shown that standard potentials of the $\text{O}_2/\text{Li}^+-\text{O}_2^-$ redox reaction becomes comparable to those of $\text{O}_2/\text{TBA}^+-\text{O}_2^-$ with increasing combined solvation energy of Li^+ and O_2^- ions, due to reduced coupling energy of Li^+-O_2^- . In addition, we show that Li^+-O_2^- solubility increases with greater combined solvation energy of O_2^- and Li^+ , which can be correlated with experimental standard $\text{O}_2/\text{TBA}^+-\text{O}_2^-$ potentials. These results highlight the importance of the interplay between O_2^-/Li^+ -solvent and O_2^-/Li^+ interactions for understanding and controlling the energetics of intermediate species produced. In **Chapter 3**, these insights are extended to understanding reaction and growth mechanisms responsible for Li_2O_2 formation.

Chapter 3: Surface and Solution-Mediated Li₂O₂ Reaction and Growth

Mechanisms and Morphologies

Reproduced in part with permission from David Kwabi, Michal Tulodziecki, Nir Pour, Daniil Itkis, Carl V. Thompson, and Yang Shao-Horn, Controlling Solution-Mediated Reaction Mechanisms of Oxygen Reduction Using Potential and Solvent for Aprotic Lithium-Oxygen Batteries. *Journal of Physical Chemistry Letters*. **2016**, 7, 1024-1212 (Copyright 2016, American Chemical Society) and Yi-Chun Lu, David G. Kwabi, Koffi P.C. Yao, Jonathon R. Harding, Jigang Zhou, Lucia Zuin and Yang Shao-Horn, The discharge rate capability of rechargeable Li-O₂ batteries. *Energy & Environmental Science*. **2011**, 4, 2999 (Copyright 2011, Royal Society of Chemistry)

3.1 Introduction

Given that the practical energy density of an Li-O₂ battery is critically linked to the degree of Li₂O₂ filling of void spaces in the cathode during discharge, understanding Li₂O₂ growth mechanisms and morphologies is of utmost importance for deploying real systems.^{67,116,117} In this chapter, we show for the first time that Li₂O₂ growth morphologies can be grouped under two broad categories: toroids of about 350 nm to, and thin conformal coatings on the electrode surface (< 50 nm). Both morphologies have subsequently been well reproduced in the literature,^{12,13,24,70,118,70,71} and shown to exhibit a discharge rate/overpotential dependence, with toroids (250 nm ~ 1 μm in size) forming at low applied oxygen reduction reaction (ORR) overpotential (defined as the difference between the applied potential and reversible potential of 2.96 V vs Li⁺/Li¹¹⁹)

typically above 2.7 V vs Li^+/Li ^{12,70,71,118,120,121} and thin deposits at larger overpotential (< 2.6 V vs Li^+/Li)^{70,71,122} and current densities. There is an apparent discrepancy between large toroidal morphologies and the fact that Li_2O_2 is a bulk insulator with a band gap between 4 - 5 eV,¹²³⁻¹²⁵ which grows to only 5 – 10 nm when electrochemically deposited on planar electrodes.²⁰ Recent electrochemical^{109,126-128} and *in situ* surface-enhanced Raman spectroscopy (SERS)⁶⁷ studies suggest that strongly coordinating electrolyte salt anions, high donor number solvents or protic additives such as water, methanol and perchloric acid enhance toroidal Li_2O_2 growth by solvating and stabilizing the lithium superoxide ($\text{Li}^+\text{-O}_2^-$) intermediate and thus promoting Li_2O_2 via disproportionation of $\text{Li}^+\text{-O}_2^-$ ($2\text{Li}^+\text{-O}_2^- \rightarrow \text{Li}_2\text{O}_2 + \text{O}_2$) rather than direct $2e^-$ transfer to the surface ($2\text{Li}^+ + \text{O}_2 + 2e^- \rightarrow \text{Li}_2\text{O}_2$). Similar reasoning has been proposed to account for the formation of toroids at low overpotentials,^{18,70} where the low driving force for electron transfer results in the disproportionation pathway being dominant. It is believed that as disproportionation is a chemical reaction, it can result in solution-mediated, homogeneous precipitation of large Li_2O_2 particles. A recent study investigating Li_2O_2 formation by adding Li^+ to KO_2 -saturated dimethylsulfoxide (DMSO) is consistent with this scheme,¹⁰⁴ in showing morphologies closely resembling electrochemically formed toroids, and composed of thin platelets, suggestive of self-assembly into micron-scale deposits.^{12,70,71,118,120,121}

Unfortunately, little *direct* evidence exists for solution-mediated growth of Li_2O_2 during cell discharge. SERS evidence of an $\text{Li}^+\text{-O}_2^-$ -related peak reducing as the ORR overpotential increases is ambiguous in this respect as the $\text{Li}^+\text{-O}_2^-$ detected^{66,67,102} may be bound to the electrode surface rather than stabilized in the solution. Likewise, although the influence of protic additives/water in promoting toroidal^{109,128} Li_2O_2 is clear, this may not necessarily be due to a solution-based growth mechanism promoted by greater $\text{Li}^+\text{-O}_2^-$ solubility. Indeed, the growth of

large particles is plausible according to conventional, surface-mediated growth models,¹²⁹ particularly at extremely low nucleation or high growth rates. Under this framework, electrolytes that promote greater $\text{Li}^+\text{-O}_2^-$ solubility impede the attachment of Li_2O_2 growth precursors to the electrode, resulting in lowered surface nucleation rates and larger particles, without a change in growth mechanism.¹¹⁷ Such a scheme is supported by a recent report showing the electrochemical formation of large, spherical (up to 1.5 μm) Li_2O_2 particles in an all-solid-state battery,¹³⁰ in which solution-mediated Li_2O_2 growth is impossible. The possibility of conventional, layer-by-layer Li_2O_2 growth¹²⁰ is further supported by first principles calculations, predicting that despite its bulk insulating nature, electrochemically grown Li_2O_2 can support appreciable surface/interfacial charge transport, as a result of surface Li^+ vacancies,^{131–133} grain boundaries,¹³⁴ and hole/electron polarons,^{18,22,124,135} and significant bulk charge transport when doped with transition metals.¹³⁶ The conductive, non-stoichiometric nature of electrochemically formed Li_2O_2 could play a role in discharge product growth, and is consistent with recent reports of solid-state superoxide-like species existing within the matrix of toroidal Li_2O_2 , using Raman^{137,138} and surface-sensitive x-ray absorption near edge spectroscopy,⁷¹ as well as magnetic measurements.¹³⁹ Given the above, the extent to which solution vs surface-mediated growth of Li_2O_2 occurs in nonaqueous electrolytes is unclear i.e. whether both mechanisms co-exist, or either is more dominant. It is particularly unclear whether the growth mechanism can change as a function of electrolyte solvent and applied potential. Resolving these questions from fundamental studies is critical for developing practical Li-air batteries with high volumetric/specific energy densities, where the choice of electrolyte solvent and duty cycle are important engineering inputs.

In order to shed light on these questions, we systematically investigated the influence of the applied ORR potential on the amount of soluble intermediates and the deposition of solid

species during ORR, using the Rotating Ring Disk Electrode (RRDE) and Electrochemical Quartz Crystal Microbalance (EQCM) techniques, respectively. All experiments were conducted on carbon substrates, using slightly polar 1,2-dimethoxyethane (DME) and strongly polar DMSO as electrolyte solvents. DMSO and DME were chosen as they have been suggested to have among the highest and lowest^{67,98,103,140} $\text{Li}^+\text{-O}_2^-$ solubilities, respectively, among candidate solvents, and provide a platform for assessing the influence of solvent polarity on Li_2O_2 growth mechanisms. We found that in both solvents, increasing the ORR overpotential results in smaller amounts of soluble ORR intermediates and faster rates of solid Li_2O_2 deposition. We also showed that the ORR reaction pathway depends on solvent at high overpotentials (below 2.5 V vs Li^+/Li). In DMSO, there is competition between 1 and $2e^-$ reduction of solvated $\text{Li}^+\text{-O}_2^-$ and O_2 , respectively whereas in DME, direct $2e^-$ transfer to O_2 is preferred. These results strongly support the hypothesis that toroidal Li_2O_2 formation at low ORR overpotentials is solvent-mediated, and show that even at high overpotentials, $\text{Li}^+\text{-O}_2^-$ solvation has an influence on the reaction pathway for Li_2O_2 formation.

3.2 Experimental Methods

3.2.1 Rotating Ring Disk Electrode Measurements

RRDE measurements were performed in glass three-electrode cells (Chemglass, USA) with a Pine (Pine, USA) bipotentiostat with Li reference and counter electrodes. Working RDEs consisted either of a glassy carbon (GC) (5 mm diameter; Pine, USA) surface surrounded by a gold ring with 6.5 mm internal diameter and 7.5 mm external diameter. All electrodes were polished to a 0.05 μm mirror-finish, ultra-sonicated in deionized water (18.2 $\text{M}\Omega\cdot\text{cm}$, Millipore)

for 5 min and dried in a glass oven (Büchi B-585) at 70 °C for 8 hours before each experiment. Electrodes were kept in the vacuum oven and directly transferred to a water-free glovebox ($\text{H}_2\text{O} < 0.1$ ppm, Mbraun, USA) without exposure to the ambient. Electrolyte solvents used were DMSO (Sigma Aldrich), DME (BASF, USA) and DMF (Sigma Aldrich). LiClO_4 was purchased from Sigma Aldrich and vacuum-dried at 100 °C for 8 hours prior to dissolution at 0.1 M.

To investigate the effect of rotation on superoxide collection, CVs were obtained between 2.0 – 4.5 V at 0 – 1600 rpm in O_2 -saturated electrolyte, with the ring held at 3.5 V. Working electrodes were first prepared by the procedure described above, and immersed into an O_2 -purged electrolyte for 20 minutes prior to each CV or chronoamperometry experiment.

To systematically investigate the effect of applied potential on the formation of superoxide (i.e. as a fraction of total ORR charge), collection experiments were performed as follows: the disk potential was stepped from open circuit voltage (OCV) of 3.0 – 3.2 V to selected potentials between 3.0 and 2.0 V (2.8, 2.7, 2.6, 2.5, 2.4, 2.2 and 2.0 V) at 900 rpm for 3 min at each potential, while the ring was held at 3.5 V in Ar-purged electrolyte. The procedure was repeated in O_2 -saturated electrolyte, with the ring again held at 3.5 V to oxidize superoxide produced during O_2 reduction. Capacitive correction of disk and ring currents was done by subtracting the charge measured under Ar from that found in pure O_2 under identical potentiostatic conditions.

3.2.2 *Electrochemical Quartz Microbalance Measurements*

EQCM measurements were conducted using a commercial SEIKO microbalance (SEIKO QCA 922) with AT-cut 9 MHz quartz covered with graphite with roughness of around 0.6 μm on both sides. The electro-active geometric surface area was $S = 0.196$ cm^2 . The crystal was immersed

in 0.1M LiClO₄ in DMSO or DME purged with O₂ for 20 min prior to electrochemical measurements. Frequency change and motional resistance were simultaneously measured during the experiment.

The EQCM was calibrated with a CV measurement in 0.001M solution of CuSO₄ in 0.5 M H₂SO₄ at RT, with 2 mV/s scanning rate. The proportionality constant ($C = \Delta f / \Delta m$) was determined between the change of quartz frequency (Δf) and change of deposited mass (Δm). A constant value $C = 1.07 \times 10^{-9}$ g/Hz close to the theoretical one $C_t = 1.068 \times 10^{-9}$ g/Hz was found, suggesting that issues regarding viscosity of the bath or roughness of the deposit can be neglected. The equivalent weight M/z of the deposited compound was determined with 2 methods. For DME, a standard linear fitting of the frequency vs charge curve was done. This method is strongly limited to fit linear parts of the curve and cannot be applied for lines with strong curvature or transition zones (a switch from one type reaction to another), such as in DMSO. In this case, we used a second method that is based on differentiating frequency with respect to charge, $df/dQ = (M/z) \times 1/(C \times F)$, where F is Faraday's constant, z is number of moles of charge, and M is mass.¹⁴¹ Before differentiation, the frequency change data were smoothed using the Savitzky-Golay procedure.

To account for the error coming from frequency oscillations, a standard deviation of obtained M/z was calculated and reported in the manuscript. Firstly, we calculated the standard deviation of the frequency, considering the smoothed data points to be mean values for each raw data point:

$$s = \sqrt{\frac{1}{N-1} \sum_{i=1}^N (x_i - \bar{x})^2}$$

where s is the sample standard deviation, N is the number of points, x_i is the data point and \bar{x} is the smoothed data point. Next, the standard deviation of the frequency mean was calculated:

$$SE_{\text{mean } f} = \frac{s}{\sqrt{N}}$$

Finally, the standard deviation of the M/z is calculated:

$$SE_{\text{mean M/z}} = \frac{SE_{\text{mean } f}}{\overline{dQ}} * C * F$$

where the \overline{dQ} is the average charge difference between two adjacent points.

Cell Testing, X-ray Diffraction, Raman and Scanning Electron Microscopy

Li-O₂ cells consisted of a lithium metal anode and freestanding vertically aligned few-walled CNTs (~1 × 1 cm, detailed preparation of the nanotubes have been reported^{14,120}) or lithiated Nafion-bonded Vulcan carbon (VC) as the O₂ electrode. VC electrodes were prepared by coating ultrasonicated inks composed of either VC or Au/VC, lithiated Nafion (LITHion™ dispersion, Ion Power, USA), and 2-propanol onto the separator (Celgard 480). After weighing and vacuum-drying at 100 °C for 8 h, the electrodes were transferred to a glove box (H₂O < 0.1 ppm, O₂ < 0.1 ppm, Mbraun, USA) without exposure to ambient. Carbon loadings were about 0.5 mg/cm² and all cells were assembled with 0.1 M LiClO₄ in DME (H₂O < 30 ppm, BASF or Sigma-Aldrich) or DMSO (H₂O < 30 ppm, BASF, USA). Cells were assembled with a lithium foil (Chemetall, Germany, 15 mm in diameter) or LiCoO₂ anode where indicated, and soaked in 120 μl of electrolyte. A stainless steel mesh was used as the current collector. Following assembly, cells were transferred to a connected second argon glove box (Mbraun, USA, H₂O < 1 ppm, O₂ < 1%)

without exposure to air and pressurized with dry O₂ (99.994 pure O₂, Airgas, H₂O < 2 ppm) to 25 psi (gage) to ensure that an adequate amount of O₂ was available to cells. Electrochemical tests were conducted using a Biologic VMP3. Galvanostatic discharge tests were performed by first resting at open circuit (~2.9 – 3.2 V vs Li⁺/Li) for 4 hours before applying current.

Raman spectroscopy was performed on discharged electrodes on a LabRAM HR800 microscope (Horiba Jobin Yvon) using an external 20 mW He:Ne 633 nm laser (Horiba, Jobin Yvon), focused with a 50× long working distance objective and a 10^{-0.3} neutral density filter. A silicon substrate was used to calibrate the Raman shift.

Scanning electron microscopy was carried out either on a Zeiss Ultra 55, Zeiss Supra 55VP, Zeiss Merlin microscope (Carl Zeiss, Germany) or a JEOL 6320. Samples were sealed in argon and quickly placed in the vacuum chamber to minimize exposure to ambient atmosphere. Imaging was performed at a working voltage of 5 kV.

XRD patterns of pristine and discharged electrodes were collected using a Rigaku SmartLab or Rotaflex X-ray diffractometer (Tokyo, Japan) with a copper rotating anode (Cu K_α) under the glancing-angle mode with an incident X-ray angle of 5°. Kapton® film sealed glass holders were used to hold discharged electrodes for XRD analysis. The XRD sample preparations of discharged electrodes were all done in the glovebox.

3.3 Results

3.3.1 Potential-Dependent Li₂O₂ Morphologies

Li-O₂ cells based on VC electrodes were first discharged between 100 and 2000 mA/g_{carbon} (Figure 3-1) to a lower voltage cutoff of 2.0 V vs Li⁺/Li. The use of Au nanoparticles enhanced the discharge voltage related to plain VC at all rates, however both the discharge capacities and voltages were found to reduce significantly with increasing current densities. This highlights the low rate capability of Li-O₂ battery systems in general, and the need for a fundamental understanding of reaction limitations and Li₂O₂ morphologies and chemistries formed upon discharge.

We first show that the discharge capacities obtained do not result from Li⁺ or O₂ transport limitations in the electrode. Considering the electrode thickness of 20 μm and estimated Li⁺ and O₂ diffusion coefficients in 0.1M LiClO₄ in DME,²⁴ the limiting flux of Li⁺ and O₂ across the flooded electrode is 3×10^{-7} and 9×10^{-8} mol cm⁻² s⁻¹ respectively. These values are much higher than that of 4×10^{-9} mol_{O₂} cm⁻² s⁻¹ corresponding to -0.8 mA cm⁻², the highest current density used in this study. Thus, the reduction in the discharge capacity is not caused by the depletion of O₂ or Li⁺ in the electrolyte-filled pores across the electrode thickness.

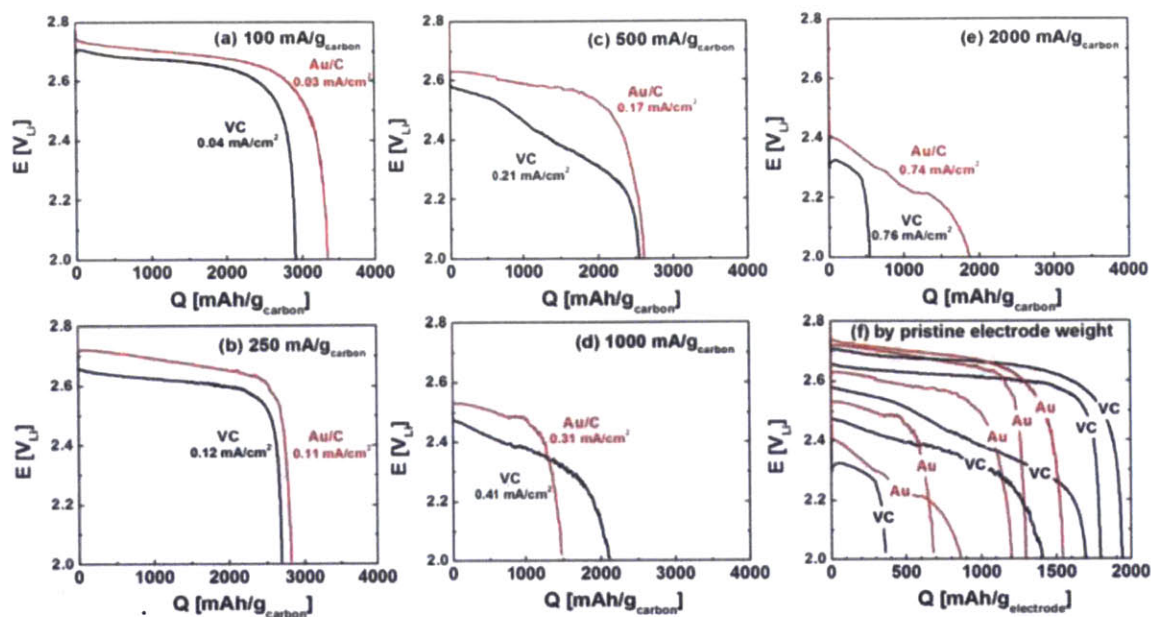


Figure 3-1. Discharge profiles of Li-O₂ cells of VC and Au/C at (a) 100 (b) 250 (c) 500 (d) 1000 and (e) 2000 mA/g_{carbon}. (f) Data in (a-e) were normalized by the total weight of the electrode before discharge (carbon + Au + binder).

Given that bulk Li₂O₂ is a wide band gap insulator,^{18,23,123} the decreased discharge voltages and capacities are more likely a result of poor charge transport through solid Li₂O₂ deposited on the electrode, where kinetically sluggish hole polaron transport^{18,22,124} and electron tunneling^{19,20} have been proposed as charge transport mechanisms. In order to understand the nature of ORR products formed on discharge, pristine and discharged VC and Au/C electrodes at 100 and 2000 mA/g_{carbon} were examined by XRD (Figure B 1 in Appendix B) and SEM. Additional XRD peaks in all discharged electrodes compared to the pristine electrodes can be assigned to Li₂O₂, suggesting that it is the dominant crystalline ORR product. Morphological changes to the O₂ electrodes before and after discharge are shown in Figure 3-2. Figure 3-2a shows that VC with

primary particle sizes in the range from 50 to 100 nm creates a porous structure to provide electronic conductivity and interconnected pores for electrolyte for both VC and Au/C electrodes. After discharge at 100 mA/g_{carbon}, the entire electrode surface on the O₂ side for both Au/C and VC was found to be covered by donut-shaped particles on the order of 300 nm.

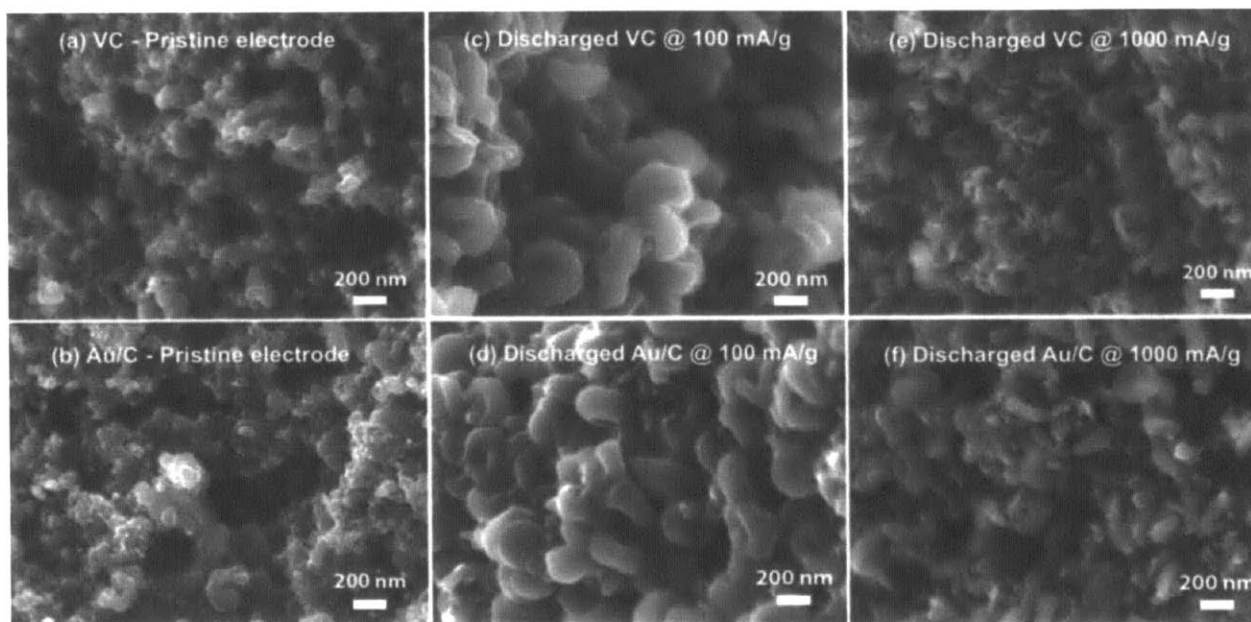


Figure 3-2. SEM images of (a) pristine VC electrode, (b) pristine Au/C electrode, (c) VC and (d) Au/C electrode discharged at 100 mA/g, (e) VC and (f) Au/C electrode discharged at 1000 mA/g_{carbon}. SEM images were taken from the surface of the air electrode on the O₂ side.

At the high current density of 1000 mA/g_{carbon}, the particle sizes of ORR products in the discharged electrodes are very comparable and much smaller than those found at 100 mA/g, as shown in Figure 3-2e-f. This dependence of Li₂O₂ morphology on applied ORR potential or discharge rate has been reproduced by subsequent studies^{70,71} and detailed transmission electron microscopy studies of Li₂O₂ donuts/toroids have shown that they are composed of epitaxially stacked layers

of crystalline Li_2O_2 plates.¹²⁰ How these toroids form, however, is a critical question that is not completely understood. As discussed in the Introduction, there is much debate surrounding the influence of solution vs surface-mediated Li_2O_2 growth mechanisms on Li_2O_2 morphology, which is tackled in more detail in the following section.

3.3.2 *Solution and Surface-Mediated Reaction Mechanisms for Li_2O_2 Formation*

RRDE experiments were first performed to examine the influence of applied potential on the amount of soluble ORR species. Cyclic voltammograms (CVs) of oxygen reduction were obtained using RRDE in DMSO and DME to quantify the formation of soluble reduction intermediates. Figure 3-3a and Figure 3-3b show steady-state CVs representing the ORR and oxygen evolution reaction (OER) in O_2 -saturated 0.1 M LiClO_4 in DME and DMSO between 2.0 – 4.5 V vs Li^+/Li at rotation speeds between 0 and 1600 rpm. The ORR current response has an onset at ~ 2.75 V in DME, and maximum current around -0.24 mA/cm^2 at all rotation speeds. The presence of a rotation-independent current peak can be attributed to fundamentally electron-transfer-limited, rather than mass transport-limited kinetics, such as electron transport through an insulating Li_2O_2 layer.^{20,119} This behavior stands in contrast to the current response during ORR in DMSO (Figure 3-3b), which reaches a peak of -0.86 mA/cm^2 and increases with rotation, suggesting the formation of more soluble reaction intermediates/products than in DME. At 400, 900 and 1600 rpm, there is positive ring current (the ring is kept under an oxidizing potential) during the ORR on the disk in both solvents, which is consistent with the depletion of soluble oxidizable species from the electrode surface during rotation.

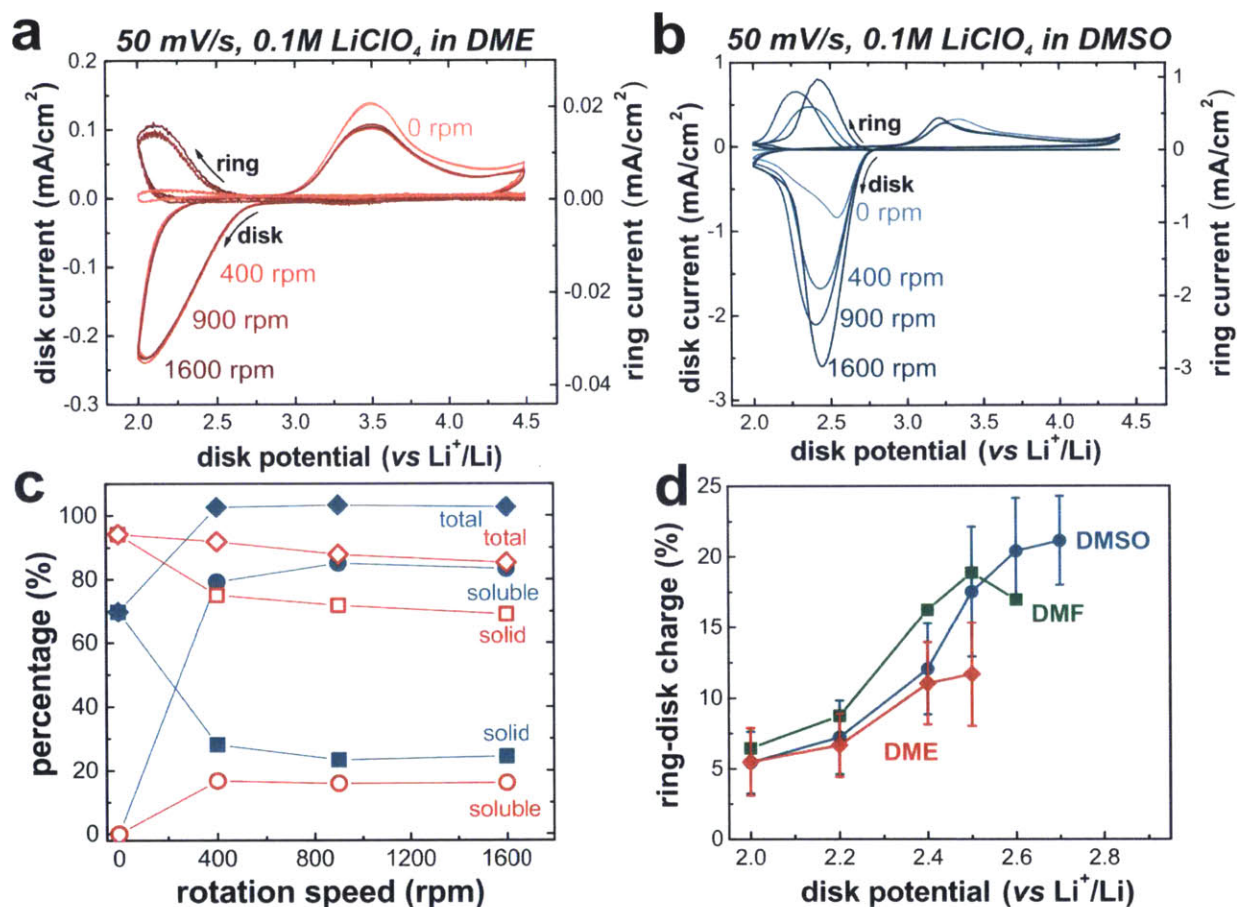


Figure 3-3. CVs (uncorrected for i-R) of ORR/OER at 50 mV/s in O₂-saturated 0.1M LiClO₄ in (a) DME and (b) DMSO on glassy carbon at 0, 400, 900 and 1600 rpm showing disk (left axis) and ring (right axis) current densities. Measurements were carried out in glass three-electrode cell with Li foil used as the counter and reference electrodes, while the ring was held at 3.5 V vs Li⁺/Li. Estimated fractions of total ORR charge (diamonds) composed of solid (squares) and soluble (circles) species as a function of rotation speed in 0.1M LiClO₄ in (c) DME (open, red symbols) and DMSO (filled, blue symbols). (d) Ar background-corrected total ring-disk charge versus applied disk potential in 0.1M LiClO₄ in DMSO (blue circles), DME (red diamonds) and DMF (green squares) at 900 rpm. Error bars for data in DMSO and DME are calculated from standard deviations from 3 independent measurements.

We show that total ORR charge can be decomposed into soluble (e.g. $\text{Li}^+\text{-O}_2^-$) and insoluble (i.e. Li_2O_2) components, in DME and DMSO in Figure 3-3c. This analysis was performed by integrating the ring current during ORR (between 2.0 – 3.0 V) and disk current during OER (3.0 – 4.5 V) with time, to obtain the ring charge (corresponding to soluble species), Q_{ring} , and OER charge (corresponding to insoluble species), Q_{OER} , which was normalized to the total charge produced during the ORR, Q_{ORR} . Provided there is insignificant parasitic reactivity between ORR products and the electrolyte or other components,⁸² the following relation will hold:

$$\frac{Q_{ring}}{\eta Q_{ORR}} + \frac{Q_{OER}}{Q_{ORR}} = 1 \quad [3-1]$$

where η represents the geometric collection efficiency of the RRDE (23.5%) previously reported.¹⁴² The first term represents the fraction of ORR charge represented by the production of soluble $\text{Li}^+\text{-O}_2^-$ -type species while the second term denotes the fraction of Li_2O_2 or other easily oxidizable solid species on the surface of the disk. In the complete absence of side reactions with the electrolyte solvent, both fractions are together expected to account for all ORR products and should add up to 100%. As shown in Figure 3-3c, > 85 % of the total ORR charge can be allocated to either soluble or solid species during rotation. The remaining fraction of the ORR charge may be attributed to incomplete removal of ORR decomposition products such as LiOH ,^{37,110,111} Li_2CO_3 ,^{14,50,52} HCO_2Li and/or $\text{CH}_3\text{CO}_2\text{Li}$,^{40,41} which are harder to oxidize than Li_2O_2 .¹⁴³ It is interesting to note that in DMSO, about 80% of the total ORR charge is comprised of soluble species, while in DME only 20% is. This difference is consistent with ORR products being more soluble in DMSO than in DME as shown in the CV measurements and suggested in previous reports.^{67,103} That almost 100% of the ORR charge can be reliably deconvolved into solid and

soluble components demonstrates the relative chemical stability of ORR products, and justifies using the RRDE to track the relative contributions of $\text{Li}^+\text{-O}_2^-$ and Li_2O_2 to ORR as a function of overpotential.

To systematically investigate the effect of applied discharge potential on the amount of $\text{Li}^+\text{-O}_2^-$, potentiostatic ORR measurements were performed on the disk, under rotation at 900 rpm, at various potentials between 2.0 and 3.0 V with the ring at 3.5 V in 0.1M LiClO_4 in DME and DMSO (Figure 3-4).

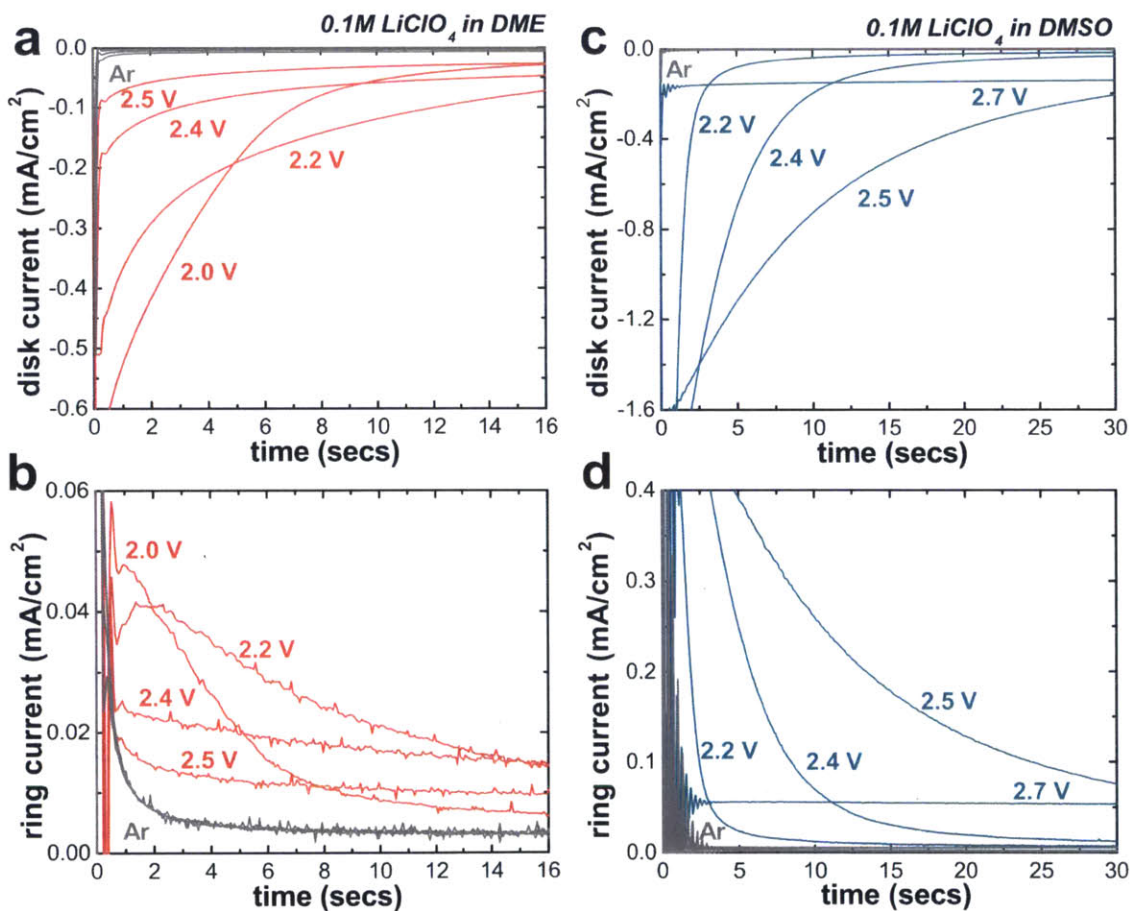


Figure 3-4. First 16 seconds of (a) disk and (b) ring current transients in Ar and O_2 -saturated 0.1M LiClO_4 in DME at disk potentials of 2.5, 2.4, 2.2 and 2.0 V with the ring held at 3.5 V vs Li^+/Li .

First 30 seconds of (c) disk and (d) ring current transients in Ar and O₂-saturated 0.1M LiClO₄ in DMSO at disk potentials of 2.7, 2.5, 2.4 and 2.2 V with the ring held at 3.5 V vs Li⁺/Li.

Consistent with CV measurements, average absolute disk and ring currents are roughly 4× smaller in DME than in DMSO. Interestingly, the potential at which ring and disk currents are greater than 3 and 10 times the background current in Ar, respectively, is lower (2.5 V vs Li⁺/Li) in DME than in DMSO (2.7 V vs Li⁺/Li). In addition, both disk and ring current responses are constant at 2.7 V vs Li⁺/Li in DMSO (Figure 3-4c-d), which can be attributed to steady-state production of soluble Li⁺-O₂⁻ with minimal Li₂O₂ formation. In contrast, current transients at other overpotentials decay with time, where the rate of decay increases with increasing overpotential (see Appendix B), which can result from the passivation of the disk by solid Li₂O₂. Thus, at 2.7 V vs Li⁺/Li in DMSO, there is steady-state production of soluble Li⁺-O₂⁻ with minimal Li₂O₂ formation. This hypothesis is additionally supported by disk oxidation CVs that were run between 3.0 and 4.5 V vs Li⁺/Li after each potentiostatic reduction (Appendix B), which show that after 3 min of potentiostatic ORR at 2.7 V vs Li⁺/Li, the resulting oxidation is only slightly higher than the background sweep in O₂ i.e. oxidation CVs that were run without potentiostatic reduction having occurred immediately beforehand.

Increasing the overpotential results in smaller amounts of soluble Li⁺-O₂⁻. The Ar background-corrected ring/disk charge, Q_{ring}/Q_{ORR} , decreases as a function of disk potential in both DMSO and DME (Figure 3-4d). Thus, a high fraction of ORR charge goes towards the production of soluble Li⁺-O₂⁻ at low overpotentials, but Li₂O₂ and other insoluble species at higher overpotentials. This result supports the hypothesis that the major reaction pathways governing Li₂O₂ growth morphologies observed in Li-O₂ cells are potential-dependent. At discharge potentials above 2.75 V vs Li⁺/Li in both 0.1M LiClO₄ in DME⁷¹ and DMSO (Figure B 4 in

Appendix B), chemical disproportionation and aggregation of $\text{Li}^+\text{-O}_2^-$ species results in toroidal Li_2O_2 while below 2.6 V, direct, surface-mediated electron transfer is responsible for conformal Li_2O_2 coatings. In further support of this scheme, it is particularly interesting to note that at low overpotentials/high absolute potentials (2.6 and 2.7 V), Q_{ring}/Q_{ORR} in DMSO begins to approach the collection efficiency of the RRDE (23.5%), while in DME, the highest Q_{ring}/Q_{ORR} is about 12%. At high overpotentials/low absolute potentials (< 2.4 V vs Li^+/Li), however, Q_{ring}/Q_{ORR} becomes comparable in both solvents. These observations further support the above scheme: since $\text{Li}^+\text{-O}_2^-$ is the predominant species at low overpotentials, Q_{ring}/Q_{ORR} is highly sensitive to $\text{Li}^+\text{-O}_2^-$ solubility in that regime, while at higher overpotentials, surface-mediated formation of solid Li_2O_2 dominates and therefore Q_{ring}/Q_{ORR} is solvent-independent. In order to support the universality of this hypothesis, we performed similar potentiostatic RRDE experiments in dimethylformamide (DMF), which has an intermediate $\text{Li}^+\text{-O}_2^-$ solubility,¹⁴⁰ i.e. between DMSO and DME (Figure 3-3d). Q_{ring}/Q_{ORR} follows the trend expected from DMSO and DME, with the amount of soluble intermediates decreasing as overpotential increases.

As RRDE is sensitive to the formation of soluble species during ORR, we complemented the above insights using EQCM measurements, which are sensitive to the deposition of solid species. CV experiments were conducted on a graphite-coated quartz crystal in 0.1 M LiClO_4 in O_2 -saturated DME and DMSO at 2 mV/s, with mass changes during Li-O_2 reactions monitored by analysis of changes to the resonant frequency of the crystal. Figure 3-5a-b show the CV profiles of ORR and OER together with the frequency changes in DME and DMSO electrolytes.

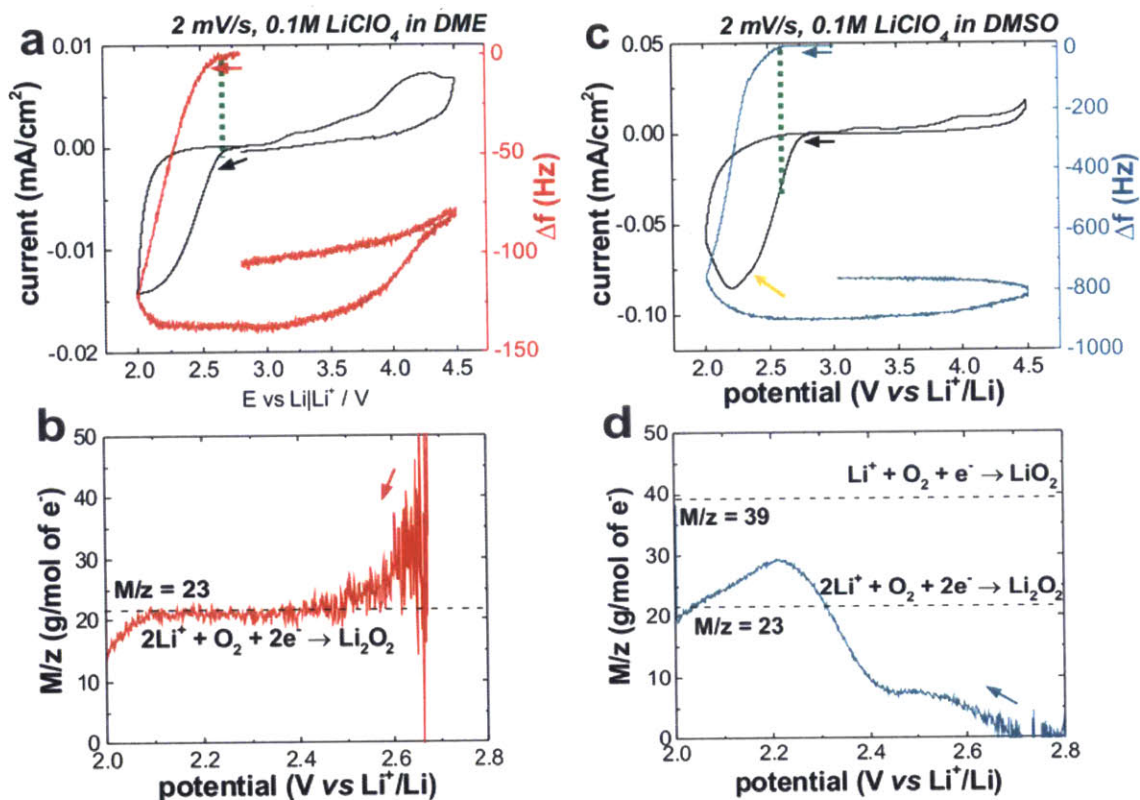


Figure 3-5. CVs showing ORR and OER reactions in 0.1M LiClO₄ in DME with potential plotted against (a) current and frequency and (b) M/z value of species deposited during ORR, and similar CVs in 0.1M LiClO₄ in DMSO with potential plotted against (c) current and frequency and (d) M/z value of species deposited during ORR. Dashed green lines in (a) and (c) indicate the delay between the ORR current onset and EQCM frequency decrease.

In both cases, the ORR is accompanied by a decrease in frequency that is mostly related to the mass change at the electrode surface, considering that there are small variations in motional resistance (see Appendix B). Thus, during ORR, the decrease in frequency corresponds to formation of a solid deposit on the electrode surface. A striking difference between DME and DMSO electrolytes can be seen at the beginning of the ORR process. Namely, in DME, the onset

of frequency decrease is close to the ORR current onset ($\Delta E \sim 50$ mV) while in DMSO, the frequency decrease is more significantly delayed with respect to the onset of ORR ($\Delta E \sim 200$ mV), as shown in dashed lines in Figure 3-5a and c. This is in accordance with RRDE measurements showing that ORR products are more soluble in DMSO, and would thus take a longer time to deposit as solid Li_2O_2 -type species on the electrode. Additionally, in DMSO, the frequency change during reduction (-900 Hz) is significantly higher than in DME (-140 Hz). This reflects a higher mass gain in the former case, likely resulting from disproportionation of a high concentration of solvated species, while a thinner and strongly blocking deposit is formed in DME. During oxidation, above 3.5 V the frequency starts to increase in both electrolytes, indicating the removal of the solid deposit from the electrode surface. Nevertheless, only partial oxidation of the deposit occurs, corresponding to ratios of mass removed to mass deposited of 42% and 15% in DME and DMSO, respectively. This indicates poor reversibility of the OER, in agreement with a previous report.¹⁴⁴ Comparing these ratios with the ratios of anodic vs cathodic charge of 103% and 25% for DME and DMSO, respectively, suggests that a considerable amount of side reactions occurred during the oxidation process. These strong side reactions in DME could explain the decrease in frequency when stepping from 4.5 to 3.0 V, as a result of etching of the electrode; however this phenomenon is not completely understood.

Consistent with RRDE results, EQCM measurements show that increasing the ORR overpotential results in increased deposition of solid species. We quantified the formation of solid species relevant to Li-O₂ electrochemistry by using the Sauerbrey equation¹⁴⁵ (see Experimental Methods) to calculate the mass, M , of deposits formed during ORR per unit mole of charge, z , passed (M/z value). Since specific reactions have precise M/z values (Table 3-1), we compared them with experimental ones to identify particular reactions at different ORR potentials.

Table 3-1. Possible Li-O₂ reactions during ORR and their corresponding M/z values.

Reaction	M/z (g/mol)
1) $O_2 + Li^+ + e^- \leftrightarrow LiO_{2(solid)}$	39
2) $O_2 + Li^+ + e^- \leftrightarrow Li^+-O_2^- (solution)$	0
3) $O_2 + 2Li^+ + 2e^- \leftrightarrow Li_2O_{2(solid)}$	23
4) $O_2 + 4Li^+ + 4e^- \leftrightarrow 2Li_2O (solid)$	15
5) $LiO_{2(solid)} + Li^+ + e^- \leftrightarrow Li_2O_{2(solid)}$	7
6) $Li_2O_{2(solid)} + 2Li^+ + 2e^- \leftrightarrow 2Li_2O (solid)$	7
7) $2LiO_{2(solution)} \leftrightarrow Li_2O_{2(solid)} + O_2$	∞
8) $LiO_{2(solution)} + Li^+ + e^- \leftrightarrow Li_2O_{2(solid)}$	46

The M/z value during ORR in DME was obtained by calculating it from the differential of frequency over charge. Instantaneous M/z values obtained with this method at each potential during the voltammetric scan, are shown in Figure 3-5d. Between 2.75 and 2.50 V, the M/z value was indeterminate, as a result of negligible deposition of solid species; this is likely to be the result of soluble species being formed. Between 2.50 and 2.05 V, however, the M/z rapidly stabilizes at 22 ± 2 g/mol. This value is close to the theoretical value for Li₂O₂ formation *via* either 2e⁻ reduction of O₂ ($O_2 + 2Li^+ + 2e^- \leftrightarrow Li_2O_{2(solid)}$) or disproportionation of solution-based Li⁺-O₂⁻. Given,

however, that (i) electron transfer to $\text{Li}^+\text{-O}_2^-$ has been estimated to have a lower kinetic barrier¹⁴⁶ and free energy⁷⁰ than disproportionation, and that (ii) small amounts of soluble $\text{Li}^+\text{-O}_2^-$ are detected by RRDE below 2.5 V, Li_2O_2 formation by direct/concerted electron transfer to O_2 ($\text{O}_2 + 2\text{Li}^+ + 2\text{e}^- \leftrightarrow \text{Li}_2\text{O}_{2(\text{solid})}$) is the more dominant mechanism. Below 2.05 V a decrease in M/z is observed, which could be due to the influence of Li_2O formation (M/z of either 15 g/mol, representing $\text{Li}_2\text{O}_{2(\text{solid})} + 2\text{Li}^+ + 2\text{e}^- \leftrightarrow 2\text{Li}_2\text{O}_{(\text{solid})}$ or 7 g/mol, representing $\text{O}_2 + 4\text{Li}^+ + 4\text{e}^- \leftrightarrow 2\text{Li}_2\text{O}_{(\text{solid})}$) or electrolyte decomposition.

M/z values during ORR in DMSO strongly reflect the influence of greater $\text{Li}^+\text{-O}_2^-$ solvation, as implied by RRDE results (Figure 3-5c-d). Firstly we can observe a change in current profile shape, in that the reduction peak has a shoulder at higher potentials (Figure 3-5c, orange arrow) unlike that of DME (lack of shoulder). The existence of a shoulder could be ascribed to a two-step reduction process of O_2 , as studied previously.^{67,98} M/z changes were calculated from the differential of $d\Delta f/dQ$ (Figure 3-5d). Between 2.7 and 2.4 V (the shoulder), M/z progressively increases and stabilizes at 8 ± 1 g/mol. Although this value is close to the one for reaction 5 ($\text{LiO}_{2(\text{solid})} + \text{Li}^+ + \text{e}^- \leftrightarrow \text{Li}_2\text{O}_{2(\text{solid})}$) and 6 ($\text{Li}_2\text{O}_{2(\text{solid})} + 2\text{Li}^+ + 2\text{e}^- \leftrightarrow 2\text{Li}_2\text{O}_{(\text{solid})}$), it cannot represent those processes as neither solid $\text{Li}^+\text{-O}_2^-$ nor Li_2O_2 , which are required reactants, are present at the onset of the ORR. Rather, considering the exceptionally high solubility of electrochemically produced $\text{Li}^+\text{-O}_2^-$ in DMSO above 2.4 V (Figure 3-3d), the small M/z represents the average result of both formation of soluble $\text{Li}^+\text{-O}_2^-$ ($\text{O}_2 + \text{Li}^+ + \text{e}^- \leftrightarrow \text{LiO}_{2(\text{solution})}$, with M/z = 0 g/mol, Table 3-1) and either solid Li_2O_2 ($2\text{LiO}_{2(\text{solution})} \leftrightarrow \text{Li}_2\text{O}_{2(\text{solid})} + \text{O}_2$, M/z = 22.9 g/mol) or adsorbed $\text{Li}^+\text{-O}_2^-$ (39 g/mol). It is proposed that the formation of small amounts of Li_2O_2 (~ 35% of ORR in Figure 3-3d) is more likely than the adsorption of $\text{Li}^+\text{-O}_2^-$, given the high solubility of $\text{Li}^+\text{-O}_2^-$ in

DMSO^{67,140} (Figure 3-3d), and the fact that Li⁺-O₂⁻ can readily disproportionate into Li₂O₂^{67,104} within the timescale of the cathodic scan (> 5 min). At potentials below 2.4 V (second process away from the shoulder) we observed an increase in M/z, going through a peak at M/z = 29 ± 1 g/mol, followed by a decrease to 21 ± 1 g/mol. This second process in the literature has been ascribed in the literature to direct electrodeposition of Li₂O₂ (O₂ + 2Li⁺ + 2e⁻ ↔ Li₂O_{2(solid)}),^{67,98} and should give theoretical M/z of 22.9 g/mol. The peak value of 29 ± 1 g/mol is therefore most probably due to the combined effect of direct Li₂O₂ formation by 2-electron transfer (23 g/mol, O₂ + 2Li⁺ + 2e⁻ ↔ Li₂O_{2(solid)}, Table 3-1) and 1-electron reduction of solvated Li⁺-O₂⁻ (46 g/mol, LiO_{2(solution)} + Li⁺ + e⁻ ↔ Li₂O_{2(solid)}, Table 3-1). Fast Li⁺-O₂⁻ disproportionation is possible, but likely a minority pathway due to its relatively unfavorable energetics,^{70,146} as discussed above. Below 2.05 V, the M/z decreases in a similar manner as in DME, which suggests that the decrease in M/z is more likely related to Li₂O formation rather than electrolyte decomposition.

To further assess the possibility that M/z values of ~ 23 g/mol observed at high overpotentials correspond to *fast* disproportionation of soluble Li⁺-O₂⁻ into Li₂O₂, we calculated the expected ring-disk charge for superoxide disproportionation in DMSO and DME, assuming first order reactivity (Figure 3-6, more discussion in Appendix B).^{66,67,147}

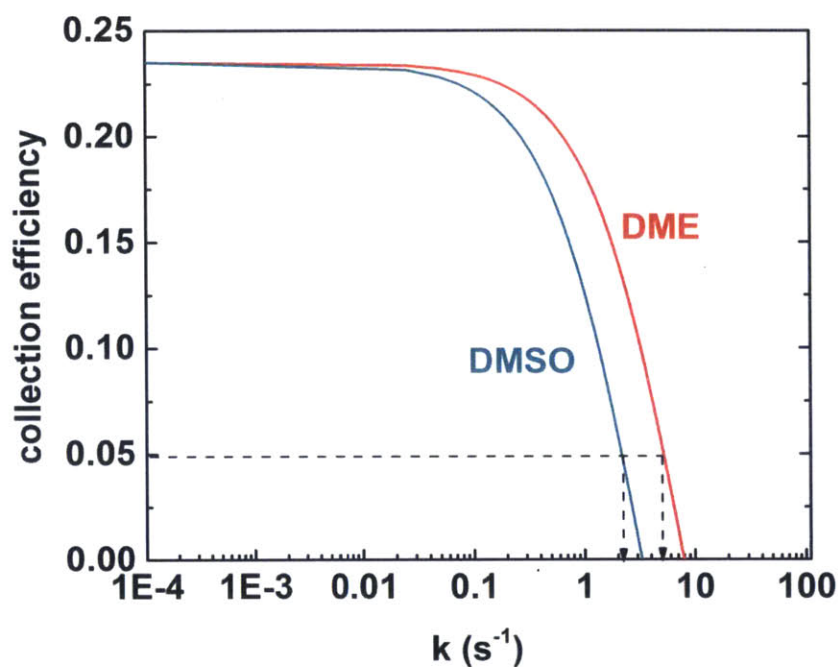


Figure 3-6. Calculated curves for the evolution of the RRDE collection efficiency vs the rate constant k of disproportionation at 900 rpm using equation S1 and viscosity of and superoxide diffusion coefficient in DMSO and DME. The dashed lines correspond to rate constants interpolated from 5% collection efficiency, and correspond to 2.3 and 5.0 s^{-1} in DMSO and DME, respectively.

The results show that the 5% ring-disk charge ratio observed in RRDE measurements at high overpotentials (Figure 3-3d) corresponds to first-order rate constants of 2.3 and 5.0 s^{-1} in DMSO and DME, respectively. These are higher than rate constants estimated from previous studies,^{66,67,147} and strongly suggest that the major reaction involved is $2e^{-}$ transfer, rather than disproportionation.

In addition to toroidal Li_2O_2 morphologies, high amounts of $\text{Li}^+\text{-O}_2^-$ promote the formation of superoxide-like domains within Li_2O_2 (Figure 3-7). We examined the influence of the amount of soluble $\text{Li}^+\text{-O}_2^-$ on the chemistry of the discharge product by discharging a carbon nanotube electrode in 0.1 M LiClO_4 in DMSO at a low rate of 10 mA per gram of carbon (i.e. mAh/g_C). At 10 mA/g_C (i.e. discharge potential ~ 2.78 V vs Li^+/Li , Figure 3-7a), Raman spectroscopy measurements on the discharge product featured peaks at 1121 and 1494 cm^{-1} (Figure 3-7b), which have been previously attributed to solid- state superoxide in discharged activated^{137,138} and Ir-loaded carbon cathodes.¹⁴⁸

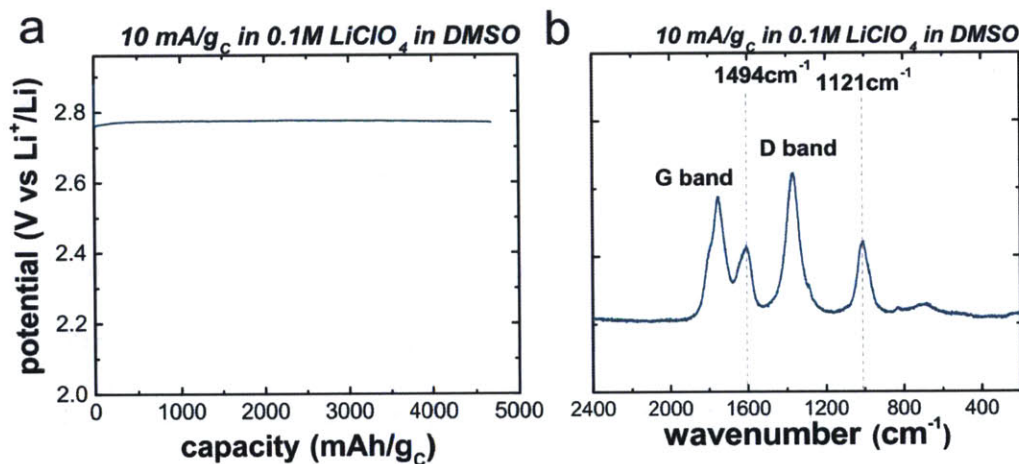


Figure 3-7. (a) Discharge profile and (b) Ex *situ* Raman spectra of CNT electrode discharged at 10 mA/g_C to ~ 4600 mAh/g_C in 0.1M LiClO_4 in DMSO.

These results are consistent with our recent work, which has indicated using sensitive X-ray absorption (XAS) measurements that Li_2O_2 toroids grown in DME at 10 mA/g_C exhibit O_2^- -like/ O_2 -rich surface chemistry, whereas Li_2O_2 formed at potentials below 2.6 V is largely stoichiometric.⁷¹ It is interesting to note that these results are broadly consistent with a Density Functional Theory (DFT) study by Hummelshøj *et al.*¹³² predicting thermodynamically stable oxygen-rich/superoxide surfaces of Li_2O_2 formed at low overpotentials (> 2.5 V vs Li^+/Li).

However, since that study did not consider the influence of electrolyte solvent, further studies are required to more fully map out the relationship between overpotential, Li_2O_2 growth mechanism and Li_2O_2 surface chemistries.

We note that as superoxide has been shown to react strongly with DMSO,^{37,110,111} its persistence in the form of $\text{Li}^+\text{-O}_2^-$ in the solid-state, as well as its high solubility in that solvent,^{67,140,149} correlates with pronounced side reactions with DMSO during solution-phase formation of Li_2O_2 at low discharge overpotentials. This is borne out by the greater prominence of flake-like agglomerates in the CNT cathode discharged above 2.75 V vs Li^+/Li in DMSO (Figure B 4b in Appendix B), which are reminiscent of LiOH ,^{110,150} than in the cathode discharged below 2.6 V. Indeed, several studies of Li-O_2 discharge in DMSO have shown that parasitic products such as LiOH and Li_2SO_4 form^{37,98,110,151,152} as a result of electrolyte decomposition.

Combining insights from both EQCM and RRDE provides a self-consistent picture of the influence of solvent and overpotential on the ORR mechanism, and how it can influence growth morphologies observed in prototypical cells (Figure 3-8). At high overpotentials, both the solvent-independent and low amount of $\text{Li}^+\text{-O}_2^-$ in RRDE and M/z values around ~ 23 g/mol clearly point to surface-mediated Li_2O_2 growth.

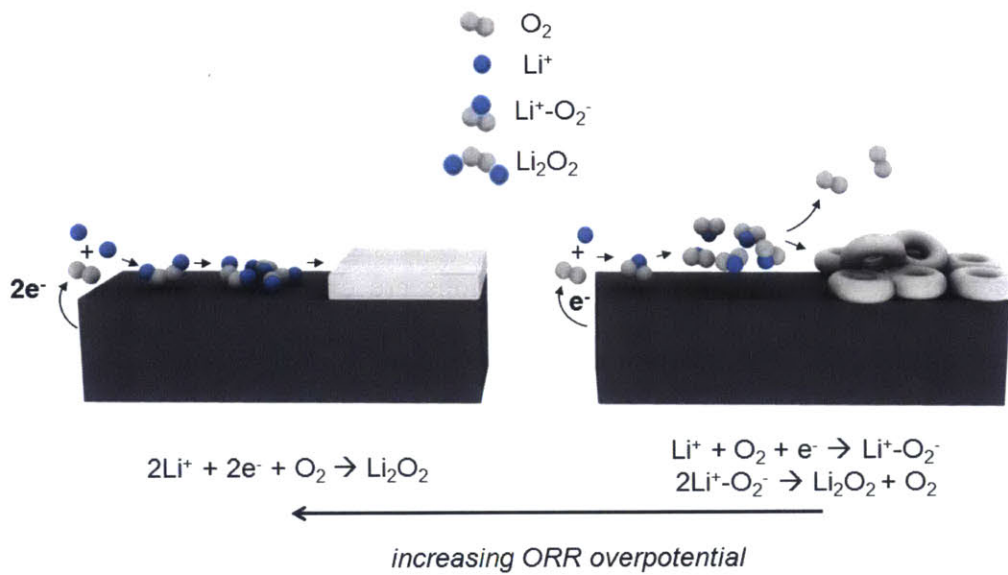


Figure 3-8. Schematic illustrating effect of ORR overpotential on predominant Li_2O_2 growth mechanisms.

This is supported by morphological studies of Li-O_2 discharge product in DMSO (Appendix B) and DME,⁷¹ where cathodes discharged at high overpotentials ($< 2.6 \text{ V vs Li}^+/\text{Li}$) show conformal, particulate morphologies. At low overpotentials ($> 2.6 \text{ V vs Li}^+/\text{Li}$), low M/z values and negligible mass gains from EQCM, and high ORR product solubilities in DMSO from RRDE point to the formation of high amounts of soluble $\text{Li}^+\text{-O}_2^-$. As toroidal Li_2O_2 has been observed in this voltage regime in DME⁷¹ and DMSO, this strongly supports a solution-mediated growth mechanism driven by self-assembly and aggregation of solvated $\text{Li}^+\text{-O}_2^-$ species. It is worth noting that non-classical self-assembly schemes have been proposed for the formation of inorganic crystals such as CaCO_3 , CeO_2 and CuO_2 ,^{153,154} where similarly layered, anisotropic shapes have been observed. These results also indicate that the adsorption energy/degree of interaction between

O_2^- and the reaction surface can be of critical importance to the reaction/growth mechanism. Indeed, a recent EQCM study studying ORR on Pt noted the formation of adsorbed $Li^+-O_2^-$ between 2.7 and 2.5 V,¹⁰⁰ rather than soluble $Li^+-O_2^-$. This difference likely originates from a ~ 2.5 eV higher O_2 adsorption energy on Pt than basal carbon sites,⁸⁴ which would favor the stabilization of O_2^- on the surface of Pt. Given that stronger interactions are expected between O_2^- and oxidized/defective carbon sites,^{50,155} systematic studies of the influence of more defective carbons on the surface stabilization of $Li^+-O_2^-$ might yield insights and strategies for tailoring Li_2O_2 morphologies for specific applications.

Thus, RRDE and EQCM are complementary techniques for exploring the participation of soluble and solid species in the Li-ORR in DMSO and DME. We found that the amount of soluble $Li^+-O_2^-$ species generated during ORR exhibits a potential dependence, such that more $Li^+-O_2^-$ is produced as a fraction of total ORR charge at low overpotentials than at high overpotentials. EQCM measurements confirm this picture, and show that at high overpotentials, direct surface-mediated O_2 reduction to Li_2O_2 is the dominant reaction mechanism regardless of solvent. Understanding the variation in $Li^+-O_2^-$ at different applied ORR potentials is particularly relevant to recent experimental studies suggesting that the growth processes of Li_2O_2 toroids formed at low overpotentials are governed by the aggregation and disproportionation of $Li^+-O_2^-$, while thin deposits/conformal coatings of Li_2O_2 originate chiefly from surface-mediated electron transfer to $Li^+-O_2^-$. Results presented herein are consistent with this growth mechanism, and also provide a path toward explaining why Li_2O_2 toroids have O-rich/superoxide-like surface chemistry, and conformal coatings are largely stoichiometric. These results shed light on strategies for rational design of Li- O_2 batteries that promote the formation of toroidal Li_2O_2 *via* the disproportionation

pathway, which is more desirable for high capacity and energy density than conformal Li_2O_2 coatings.

While the use of electrolyte solvents,⁶⁷ salts,^{126,127,156} and protic additives^{109,128,157} that increase $\text{Li}^+\text{-O}_2^-$ solubility has already emerged as one way to increase the terminal coulombic capacity of Li-O_2 batteries, the link between $\text{Li}^+\text{-O}_2^-$ solubility and Li_2O_2 morphology is not well understood. Indeed, several other considerations that potentially affect Li_2O_2 nucleation and growth kinetics and morphology are not fundamentally understood, including interactions between $\text{Li}^+\text{-O}_2^-$ and the electrode surface, supersaturation during discharge, and Li_2O_2 surface energy. In order to explore these questions, the influence of electrolyte solvent on Li_2O_2 morphology will be explored in the next section.

3.3.3 Solvent Influence on Li_2O_2 Morphology

The effect of different solvents on Li_2O_2 morphologies was systematically explored using CNT electrodes. CNTs were chosen because they are highly porous, binder-free and high surface area model electrodes that are almost ideal for the study of morphological studies of Li_2O_2 at large gravimetric capacities.^{71,120} Li_2O_2 morphologies were examined at both low (25 mA/g_C) and high (500 mA/g_C) gravimetric rates to 4000 mAh/g_C in MeCN, DME, DMSO and DMA-based solvents. The effect of these solvents on Li^+/Li and O_2/O_2^- redox potentials has already been investigated in **Chapter 2**, and their use here enables an examination of solvation effects on Li_2O_2 morphologies. Discharge profiles at both rates obtained are shown in Figure 3-9.

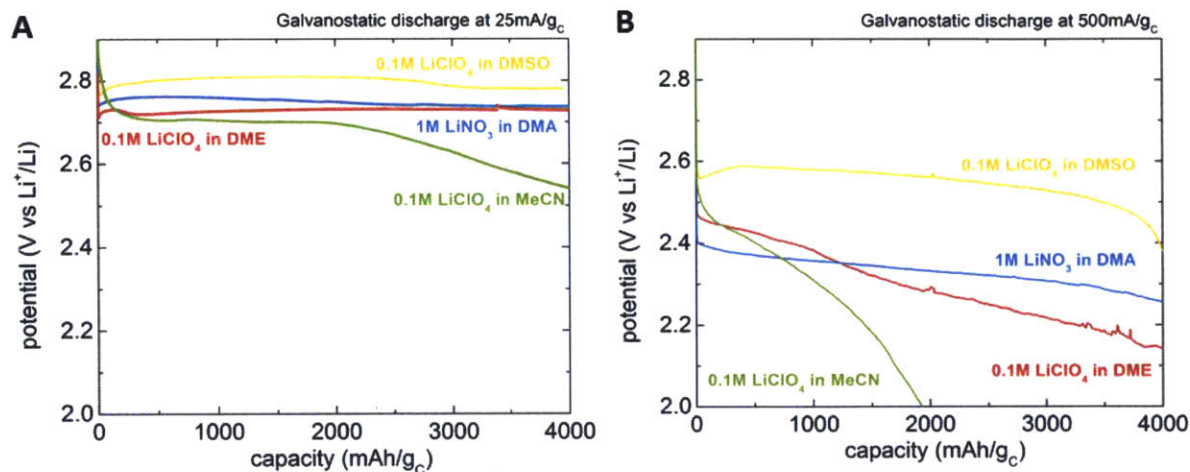


Figure 3-9. Galvanostatic discharge profiles using CNT electrodes at 25 and 500 mA/g_c to 4000 mAh/g_c in 0.1M LiClO₄ in MeCN, DME, DMSO and 1M LiNO₃ in DMA. An LiCoO₂-based anode was used for the MeCN electrolyte because of its chemical incompatibility with Li. 1M LiNO₃ was used in DMA instead of 0.1M LiClO₄ because the former has been shown to be compatible with Li metal,¹⁵⁸ which was used as the anode.

Li₂O₂ was obtained by XRD as the majority crystalline product after discharge at 25 mA/g_c (Figure B 6 in Appendix B), and the discharge voltages were arranged in the order: DMSO > DMA > DME > MeCN. This arrangement trends with the DN of these solvents, as has been recently shown,⁶⁷ but more importantly, their total solvation energies for Li⁺ and O₂⁻, as discussed in **Chapter 2**. Higher discharge potentials and capacities in greater Li⁺-O₂⁻ solvating media can be attributed to greater Li⁺-O₂⁻ solvation and solubility. Media that do not strongly solvate Li⁺-O₂⁻ promote its fast disproportionation to Li₂O₂ at the electrode surface and thus electrode passivation, whereas media that strongly solvate Li⁺-O₂⁻ facilitate its diffusion away from the electrode surface, resulting in both higher voltages and increased capacities.

A critical question relates to whether these solvent effects on discharge potential and gravimetric capacity are easily translatable to explaining Li_2O_2 morphologies. Johnson *et al.*⁶⁷ argue that in strongly $\text{Li}^+\text{-O}_2^-$ -solvating media, diffusion of $\text{Li}^+\text{-O}_2^-$ away from the electrode should result in more toroidal growth morphologies of Li_2O_2 , while in less strongly solvating media, conformal deposits should be obtained. They made this argument on the basis of direct observations of Li_2O_2 morphologies after discharge in various solvents, however two key observations militate against this hypothesis: (i) they compared Li_2O_2 morphologies at different discharge capacities, which conflates the solvent effect on morphology with the effect of higher discharge capacity and (ii) there did not appear to be a cleanly monotonic relationship between DN and toroid size, as DME, which has DN 24, supported the growth of toroids similar in size to DMSO (DN = 29.8), and larger than in methylimidazole (DN = 47). Clearly, a more complex relationship exists between Li_2O_2 morphology and $\text{Li}^+\text{-O}_2^-$ solvation than $\text{Li}^+\text{-O}_2^-$ solvation and Li-O_2 discharge capacity.

This claim is well supported by direct observations of Li_2O_2 morphologies in discharged CNTs limited to 4000 mAh/g_C at 25 mA/g_C (Figure 3-9a) in MeCN, DME, DMSO and DMA. Particulate and toroid-like morphologies are clearly observed in all solvents, with the largest toroids (~ 400 nm) appearing in MeCN and the smallest in DME. It is important to note also that in addition to microscopic toroidal morphologies, small particles of Li_2O_2 are typically observed on the CNT sidewalls. The observation, however, that the largest toroids in MeCN is surprising, given that it has the lowest DN and combined $\text{Li}^+\text{-O}_2^-$ solvation energy among all the solvents. This realization motivated the exploration of two alternative models governing Li_2O_2 toroid size, based on solvent reactivity with evolving Li_2O_2 , and a classical growth model where the nucleation rate is controlled by $\text{Li}^+\text{-O}_2^-$ supersaturation.

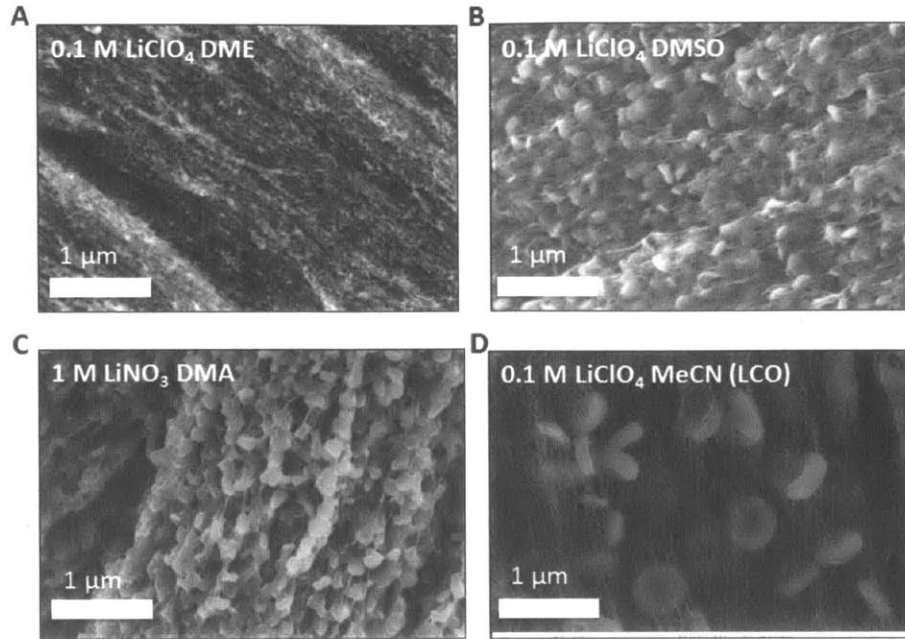


Figure 3-10. *Ex situ* SEM images of CNT electrodes discharged at 25 mA/g_C to 4000 mAh/g_C in (a) DME (b) DMSO (c) DMA and (d) MeCN.

We first consider the Li₂O₂ growth model, where the Li₂O₂ toroid size is driven by supersaturation, but impeded by reactivity between the free sites for Li₂O₂ addition and solvent molecules. Assuming that a Li₂O₂ toroid can be approximated as a sphere whose volume increases at a rate proportional to the surface area and molar flux of solvated growth precursors, the rate of change of the toroid volume is:

$$\frac{dV}{dt} = vAJ[3-1]$$

where v is the molar volume of Li₂O₂, A is the exposed surface area and J is the molar flux to the surface. Assuming the sphere grows with radius a and that J is driven by supersaturation, $J = k(C - C_s)$, where k is the effective crystal growth rate, C is the concentration of solvated Li₂O₂ growth precursors, and C_s is the equilibrium Li₂O₂ solubility, we can write

$$\frac{da}{dt} = vk(C - C_s)[3-2]$$

Assuming Li_2O_2 growth is inhibited by surface reactivity with the solvent, the rate constant for growth will correlate with the number of “free” sites on the toroid surface, such that $k = k_o(1 - \theta_e)$ where k_o is the native growth rate and θ_e is the fractional coverage by sites blocked due to reactivity with the electrolyte. This fractional coverage changes over time based on electrolyte reactivity:

$$\frac{d\theta_e}{dt} = k_e(1 - \theta_e)[3-3]$$

where $\theta_e(0) = 0$, $\theta_e = 1 - \exp(-k_e t)$, and k_e is the rate constant of Li_2O_2 reactivity with the electrolyte. By plugging equation [3-3] into [3-2], we obtain:

$$a(t) = \frac{vk_o(C - C_s)}{k_e} (1 - \exp(-k_e t)) [3-4]$$

Toroid size thus increases with higher native growth rate and supersaturation, but decreases with increasing electrolyte reactivity. In the limit of infinite discharge time,

$$a(\infty) = \frac{vk_o(C - C_s)}{k_e} [3-5]$$

Equation [3-5] suggests that the final toroid size is inversely proportional to electrolyte reactivity with Li_2O_2 , which has been studied in several recent reports of Li-O₂ electrochemistry in solvents used in this study (reactivity with DMSO is considered in **Chapter 5**).^{37,41,159-161} Given that electrolyte solvents have been shown to be susceptible to either proton abstraction or nucleophilic attack by Li_2O_2 , we may assume that rates of solvent degradation are related to $k \sim \exp(\frac{E_b}{kT})$, where E_b is the kinetic barrier to solvent decomposition. Plugging in barriers for nucleophilic attack by

Li_2O_2 on DMSO and DMA,¹⁵⁹ and proton/hydrogen abstraction from DME and MeCN^{159,161} computed by Density Functional Theory (DFT) results in the relationship between average toroid size and electrolyte decomposition rate shown in Figure 3-11.

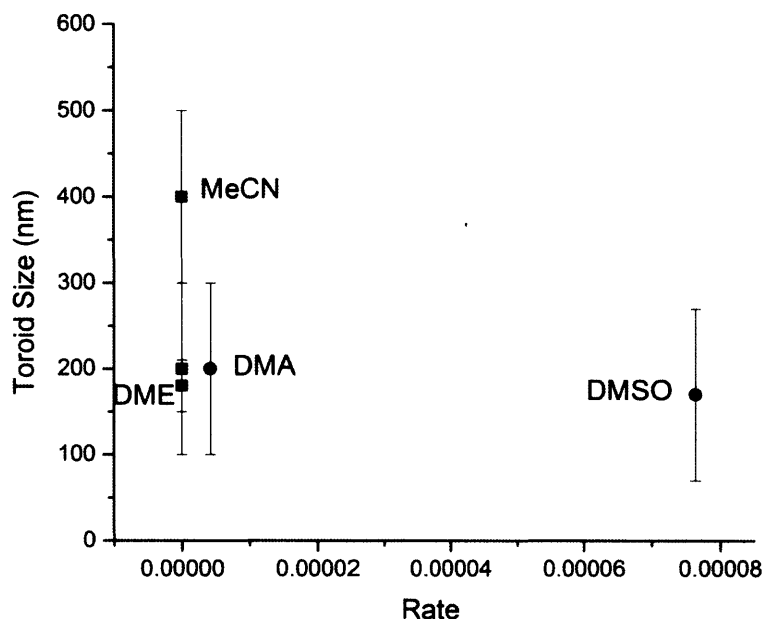


Figure 3-11. Li_2O_2 toroid size vs computed rate of electrolyte decomposition plotted according to equation [3-5] and assuming constant supersaturation.

This plot explains the difference between smaller toroid sizes in DMSO, which has a high degree of reactivity with Li_2O_2 , than in MeCN, where reactivity is much less. However, the power law relationship predicted by equation [3-5] is not observed, and toroid sizes in DMA and DME are smaller than expected given the large barriers to reactivity with Li_2O_2 predicted by DFT.

One possible origin of the discrepancies between predicted and actual toroid sizes could result from the assumption of constant supersaturation, which may not be warranted based on vastly different $\text{Li}^+\text{-O}_2^-$ solubilities examined in **Chapter 2**. We thus estimated differences in

supersaturation among these solvents based on differing $\text{Li}^+\text{-O}_2^-$ solubilities examined by RRDE.

An alternative definition of supersaturation to that given above is:

$$\frac{[a_{\text{Li}^+}]^2[a_{\text{O}_2^{2-}}]}{K_{sp}}$$

where a_{Li^+} and $a_{\text{O}_2^{2-}}$ are the solution activities of Li^+ and O_2^{2-} ions respectively, and K_{sp} is the solubility product of bulk Li_2O_2 . Standard K_{sp} values of Li_2O_2 in the solvents used above are not known from literature, and are thus estimated here. We assume that the bulk solid is in equilibrium with its solvated constituent ions such that:

$$2\mu_{\text{Li}^+}^{\circ} + \mu_{\text{O}_2^{2-}}^{\circ} - \mu_{\text{Li}_2\text{O}_2} = -RT \ln K_{sp}^{\text{Li}_2\text{O}_2}$$

where μ° is the standard state ion formation energy and μ is the chemical potential of the solid. The latter can be calculated from its standard value of 2.96 V vs Li^+/Li , while $\mu_{\text{Li}^+}^{\circ}$ and $\mu_{\text{O}_2^{2-}}^{\circ}$ can be inferred from the standard redox potentials of formation of Li^+ and O_2^{2-} . Given that the redox potential of solvated O_2^{2-} is not known in organic solvents, we approximate $\mu_{\text{O}_2^{2-}}^{\circ}$ as $2\mu_{\text{O}_2^-}^{\circ}$. Both $\mu_{\text{Li}^+}^{\circ}$ and $\mu_{\text{O}_2^{2-}}^{\circ}$ can be calculated from standard Li^+/Li and O_2/O_2^- redox potentials measured in **Chapter 2**, resulting in K_{sp} values shown in Table 3-2 for DME, DMSO, MeCN and DMA. DMSO has the highest solubility product at -21.7, which is expected given its high solvating power for Li^+ and O_2^- ions, while DME has the smallest, at -40.0. These values are several orders of magnitude lower than supersaturation for inorganic compounds such as MgCO_3 and CaCO_3 in aqueous media, where $\log_{10} K_{sp}$ is -7.8 and -8.5 respectively,^{162,163} consistent with the notion that Li_2O_2 exhibits negligible solubility in non-aqueous solvents.

In order to estimate supersaturation during discharge, solution activities of Li^+ and O_2^{2-} are approximated using the concentrations of Li^+ and O_2^- , which are estimated from RRDE measurements of soluble $\text{Li}^+\text{-O}_2^-$ and known O_2 solubilities in **Chapter 2**. The activity of Li^+ is thus 0.1, while that for $\text{O}_2^- = \text{O}_2$ solubility \times fraction of ORR charge composed of soluble $\text{Li}^+\text{-O}_2^-$ (a collection efficiency of 1% is assumed for MeCN given negligible $\text{Li}^+\text{-O}_2^-$ solubility in that solvent). Plugging supersaturation values obtained by this method into the expression for toroid size above yields a solvent-dependent relationship among toroid sizes shown in Table 3-2, where $\text{MeCN} \gg \text{DME} > \text{DMA} > \text{DMSO}$.

Table 3-2. Supersaturation and solubility products for Li_2O_2 in DME, DMSO, MeCN and DMA.

solvent	$\log_{10} K_{sp}$	$\text{Li}^+\text{-O}_2^-$ solubility (%)	σ	$a(\infty)$
DME	-40.0	1.6	$3.9\text{e}31$	$9.45\text{e}36$
DMSO	-21.7	20.2	$1.5\text{e}14$	$2.0\text{e}18$
MeCN	-39.3	--	$2.2\text{e}30$	$1.2\text{e}43$
DMA	-27.4	9.6	$1.8\text{e}19$	$7.7\text{e}34$

This ordering of toroid sizes is roughly consistent with what is observed in Figure 3-10; however the relative differences among toroid sizes are unrealistically large. This is a result of two factors. Firstly, there is considerable uncertainty regarding DFT-computed barriers to Li_2O_2 -induced electrolyte decomposition, where rates extracted from computed barriers vary by up to 10 orders of magnitude. Such a wide range of rates is unlikely to be borne out in experiment, and thus model chemical studies of Li_2O_2 reactivity with the solvents listed here will be expected to yield more accurate decomposition rates. Uncertainties regarding supersaturation comprise another

possibly significant source of error, with values varying by up to 11 orders of magnitude, as shown in Table 3-2. Rather than approximating O_2^{2-} activities using RRDE measurements of O_2^- solubility and the O_2/O_2^- redox potential, direct measurement of Li^+ and O_2^{2-} concentrations both at equilibrium and during discharge *via* Inductively Coupled Plasma or *in situ* measurements, is likely to prove fruitful in more accurately estimating supersaturation.

In summary, it has been shown that Li_2O_2 morphologies exhibit a strong dependence on applied potential, with large toroidal particles forming at high potentials (> 2.7 V vs Li^+/Li), while more conformal deposits are formed at lower potentials. This behavior has been rationalized in terms of different reaction pathways for Li_2O_2 formation, using RRDE and EQCM studies of the ORR. Solution-mediated disproportionation of $Li^+-O_2^-$ is likely to lead to toroidal Li_2O_2 , while surface-mediated electron transfer results in thinner, less space-filling morphologies. The dependence of Li_2O_2 morphology on solvent was shown to not depend on $Li^+-O_2^-$ solvation; and a growth model rationalizing particle size in terms of Li_2O_2 supersaturation and reactivity with electrolyte was introduced. This model could serve as a useful starting point for evaluating Li_2O_2 morphologies grown in different solvents with varying supersaturation and kinetic barriers to decomposition *via* deprotonation, hydrogen removal or nucleophilic attack. It is important to note in this regard that several other factors potentially affecting Li_2O_2 morphology remain to be understood, such as interactions between $Li^+-O_2^-$ and the electrode surface, and Li_2O_2 surface energy of evolving crystallites. In **Chapter 5**, the relationship between Li_2O_2 morphology, discharge product chemistry and electrolyte stability is explored in more detail, using the influence of water on these parameters as a test variable. Particular attention is paid to nucleation and growth processes of Li_2O_2 , rather than $Li^+-O_2^-$ solvation, in order to better bridge the gap between atomic scale investigations of reaction energetics and *ex situ* observations of Li_2O_2 morphologies.

Chapter 4: The Effect of Water on Discharge Product Growth and Chemistry in Li-O₂ Batteries

4.1 Introduction

One prominent strategy to promote Li-O₂ battery energy densities in the past few years has been the addition of water to the electrolyte or operation under high relative humidities, which is shown to increase capacity in ethereal solvents.^{109,128,157,164} Aetukuri *et al.*¹⁰⁹ have shown that adding up to 4000 ppm of water to the nominally anhydrous electrolyte based on dimethoxyethane (DME) can dramatically increase the terminal discharge capacity of Li₂O₂ in Li-O₂ cells. Moreover, Schwenke *et al.*¹²⁸ not only show that water addition increases discharge capacity, in agreement with Aetukuri *et al.*¹⁰⁹, but also that higher water concentrations are needed to promote discharge capacity at greater discharge rates. This increase in discharge capacity with water addition has been attributed to a change in the dominant reaction pathway for Li₂O₂ formation after the formation of Li⁺-O₂⁻ intermediate ($\text{Li}^+ + \text{O}_2 + \text{e}^- \rightarrow \text{Li}^+-\text{O}_2^-$), from surface e⁻ transfer-driven film growth ($\text{Li}^+-\text{O}_2^- + \text{Li}^+ + \text{e}^- \rightarrow \text{Li}_2\text{O}_2$) in the absence of significant amounts of water to solution-mediated growth of toroidal particles (up to ~ 1 μm) Li₂O₂ involving the disproportionation of soluble Li⁺-O₂⁻ in solution ($2\text{Li}^+-\text{O}_2^- \rightarrow \text{Li}_2\text{O}_2 + \text{O}_2$).¹⁰⁹

Unfortunately, how water affects the dominant reaction pathway in the formation of Li₂O₂ remains unclear. Li₂O₂ particle size increases upon water addition can result from a change in the pathway (i.e. from surface e⁻ transfer-driven to solution-mediated growth) or a *change* in the nucleation and growth rates for a given pathway for Li₂O₂ formation. Previous work has shown

that lowering the discharge rate can increase Li_2O_2 particle sizes,^{70,71,117} which can be explained by lowering nucleation rates for $\text{Li}^+\text{-O}_2^-$ formation ($\text{Li}^+ + \text{O}_2 + \text{e}^- \rightarrow \text{Li}^+\text{-O}_2^-$) and surface attachment, as suggested by Lau and Archer.¹¹⁷ Moreover, the fact that Li_2O_2 rather than LiOH is formed in Li-O_2 electrodes at high water concentrations (up to 1% water in the DME-based electrolyte¹²⁸), is rather puzzling. Previous work has shown that electrochemically formed superoxide (O_2^-) is chemically unstable in acidic media,¹⁶⁵ and reacts with water in both aqueous¹⁶⁵ and non-aqueous¹⁶⁶⁻¹⁶⁸ media such as DMSO, DMF and MeCN resulting in the formation of hydroxide (OH^-) and/or strongly basic hydroperoxy/hydroperoxyl ($\text{HO}_2^-/\text{HO}_2\cdot$) species.¹⁶⁵⁻¹⁶⁸ A more fundamental understanding of Li-O_2 electrochemistry in the presence of water is therefore required in order to understand: (i) whether the growth of large Li_2O_2 toroids is attributable to a change in reaction mechanism and (ii) what dictates Li-O_2 reaction product chemistry (Li_2O_2 vs LiOH) in the presence of water.

Here we propose that the capacity increase with water addition reported by Aetukuri *et al.*⁹ and Schwenke *et al.*¹⁰ can be attributed to the following two hypotheses: water could (i) lower surface Li_2O_2 nucleation rate *via* the surface e^- transfer pathway and (ii) increase the solubility of $\text{Li}^+\text{-O}_2^-$ by lowering the coupling strength of Li^+ to O_2^- ¹⁴⁰ which promotes the disproportionation of $\text{Li}^+\text{-O}_2^-$ to form large, toroidal Li_2O_2 . The second hypothesis is supported by the fact that water has a higher acceptor number than organic solvents,⁷⁸ and thus strongly solvates O_2^- .¹⁶⁵

In this chapter, we first show that the presence of water in a DME-based electrolyte decreases the surface Li_2O_2 nucleation rate during Li-O_2 battery discharge using potentiostatic measurements and *ex situ* microscopic observations of Li_2O_2 particle sizes. Potentiostatic tests have been widely used to study the nucleation and growth during metal electrodeposition, since nucleation and growth parameters can be extracted from the resulting current transients at fixed

overpotential using established kinetic models.¹²⁹ This strategy has been recently applied to studying Li₂S precipitation in Li-S batteries,^{169,170} but is lacking in most mechanistic studies of Li₂O₂ growth, where galvanostatic tests are more widely used.^{24,67,70,109,117} Avrami analysis of current transients from potentiostatic tests suggests that the geometry of Li₂O₂ growth stays the same, with and without water addition of 5000 ppm. In addition, we show that adding water to an MeCN-based electrolyte results in LiOH after discharge instead of Li₂O₂ in the absence of water addition. Using first principles calculations, we propose that solvents such as DME have low water solvation energy and high pK_a of solvated water, which imposes a high thermodynamic barrier for reactivity between superoxide ions and water molecules, and thus leads to Li₂O₂ formation in the presence of added water.

4.2 Experimental and Theoretical Methods

4.2.1 Cell Testing

Li-O₂ cells consisted of a lithium metal anode (Chemetall, Germany, 15 mm in diameter) and either carbon paper or freestanding vertically aligned few-walled CNTs (detailed preparation of the nanotubes have been previously reported^{14,120}) as the O₂ electrode (~ 1 × 1 cm). After weighing and vacuum-drying at 100 °C for 8 h, the electrodes were transferred to a glove box (H₂O < 0.1 ppm, O₂ < 0.1 ppm, Mbraun, USA) without exposure to ambient. CNT loadings were about 1 mg/cm² and all cells were assembled with 0.1 M LiClO₄ in DME (H₂O < 30 ppm, BASF, USA) or MeCN (H₂O < 30 ppm, Sigma Aldrich, USA). Electrodes with 5000 ppm of water were assembled by adding deionized water to the corresponding electrolyte. About 200 µl of electrolyte was used. A stainless steel mesh was used as the current collector. Following assembly, cells were transferred to a connected second argon glove box (Mbraun, USA, H₂O < 1 ppm, O₂ < 1%) without

exposure to air and pressurized with dry O₂ (99.994% pure O₂, Airgas, H₂O < 2 ppm) to 25 psi (gauge) to ensure that an adequate amount of O₂ was available to cells. Electrochemical tests were conducted using a Biologic VMP3. Galvanostatic discharge tests were performed by first resting at open circuit (~2.9 – 3.2 V vs Li⁺/Li) for 4 hours before applying current.

4.2.2 Scanning and Transmission Electron Microscopy

Scanning electron microscopy was carried out on a Zeiss Ultra 55, Zeiss Supra 55VP, and a Zeiss Merlin microscope (Carl Zeiss, Germany). Samples were sealed in argon and quickly placed in the vacuum chamber to minimize exposure to ambient atmosphere. Imaging was performed at a working voltage of 5 kV.

Transmission electron microscopy was carried out by a JEOL 2011 (JEOL, USA) and a FEI Tecnai microscope (FEI, USA). A selection of CNTs were placed in copper double grids (Ted Pella, USA) and sealed in argon until quick loading into the vacuum chamber to minimize exposure to ambient air. Images were taken with a working voltage of 80 kV.

4.2.3 *pKa and Solvation Free Energy Calculations*

As mentioned in the main manuscript text, $\Delta G_{\text{deprotonation,liq}}$ was estimated using the thermodynamic cycle shown in Figure 4-1. In this scheme which includes four explicit solvent molecules, $\Delta G_{\text{liq}} = \Delta G_{\text{deprotonation,liq}}$ and can be expressed by:

$$\Delta G_{\text{liq}} = \Delta G_{\text{gas}} + \Delta \Delta G_{\text{solvation}} = \Delta G_{\text{gas}} + \Delta G_s(\text{H}^+) + \Delta G_s(\text{OH}^-(\text{Solvent})_4) - \Delta G_s(\text{H}_2\text{O}(\text{Solvent})_4)$$

It should be noted that liquid-phase solvation free energy calculations use a reference state of 1 M, while gas-phase Gibbs free energy calculations use a reference state of 1 atm.

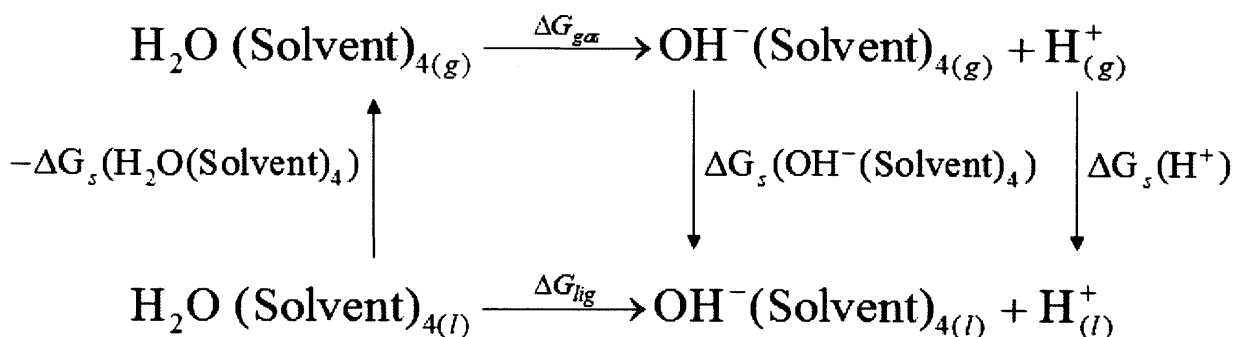


Figure 4-1. Thermodynamic cycle showing calculation of pKa of water in different aprotic solvents.

Utilizing the following unit conversion between the gas-phase free energy calculations and the solvation energy calculations,

$$\Delta G_{gas} (1 \text{ M}) = \Delta G_{gas} (1 \text{ atm}) + RT \ln(24.46)$$

we obtained the final expression for ΔG_{liq}

$$\begin{aligned}
 \Delta G_{liq} &= G(\text{H}^+_{(g)}) + G(\text{OH}^- (\text{Solvent})_{4(g)}) - G(\text{H}_2\text{O}(\text{Solvent})_{4(g)}) + RT \ln(24.46) + \Delta G_s(\text{H}^+) + \Delta G_s(\text{OH}^- (\text{Solvent})_4) - \Delta G_s(\text{H}_2\text{O}(\text{Solvent})_4) \\
 &= G(\text{H}^+_{(g)}) + G(\text{OH}^- (\text{Solvent})_{4(l)}) - G(\text{H}_2\text{O}(\text{Solvent})_{4(l)}) + RT \ln(24.46) + \Delta G_s(\text{H}^+)
 \end{aligned}$$

In the above equation $G(\text{H}^+_{(g)})$ was computed to be -6.28 kcal/mol using the CBS-QB3 theory. The values of $\Delta G_s(\text{H}^+)$ in a range of solvents were found from literature and shown in **Table C 1** with the solvents' dielectric constants. Plotting the $\Delta G_s(\text{H}^+)$ against the dielectric constant in **Figure C 1**, a linear relationship is observed. We used the fitted relation between the value of $\Delta G_s(\text{H}^+)$ and the solvent's dielectric constant as a first-order approximation for solvents whose proton solvation energy data is not reported in the literature. For DME, DMF and DMA, the values of $\Delta G_s(\text{H}^+)$ were estimated to be -220.1, -263.1 and -263.9 kcal/mol, respectively. Note that if we use this estimated $\Delta G_s(\text{H}^+)$ in DME, a pKa value of 86.0 is obtained, which is incomparable with the other solvents.

Therefore instead, we report in **Table 4-1** the pKa of water in DME calculated using the value of $\Delta G_s(\text{H}^+)$ in dimethylsulfoxide (DMSO). This gives the lower bound of the pKa of water in DME, since we expect the value of $\Delta G_s(\text{H}^+)$ in DME to be lower (smaller in absolute value) than that in DMSO.

The ground-state molecular structures were fully optimized at B3LYP/6-31G(d,p) level and verified by the absence of imaginary frequencies. The optimized geometries were utilized to perform single point energy calculations at the M06L/6-311++G(d,p) level of theory. The polarizable continuum model (PCM) solvation model was used for solution-phase calculations.¹⁷¹ The solvation free energy of water in different organic solvents were also investigated and calculated using the CCSD/aug-cc-pVTZ theory and the implicit PCM solvation model. All calculations were performed using the Gaussian 09 computational package.¹⁷²

4.3 Results

4.3.1 *The Effect of Water on Li₂O₂ Nucleation Rates on Low-Surface-Area Carbon Paper Electrodes*

We first show using potentiostatic Li-O₂ discharge tests (**Figure 4-2** and Figure 4-3) that the presence of water decreases the surface Li₂O₂ nucleation rate. We define nucleation as the formation of Li₂O₂ nuclei at active sites on the carbon electrode surface and growth as addition of Li₂O₂ to these nuclei *via* electrochemical processes.

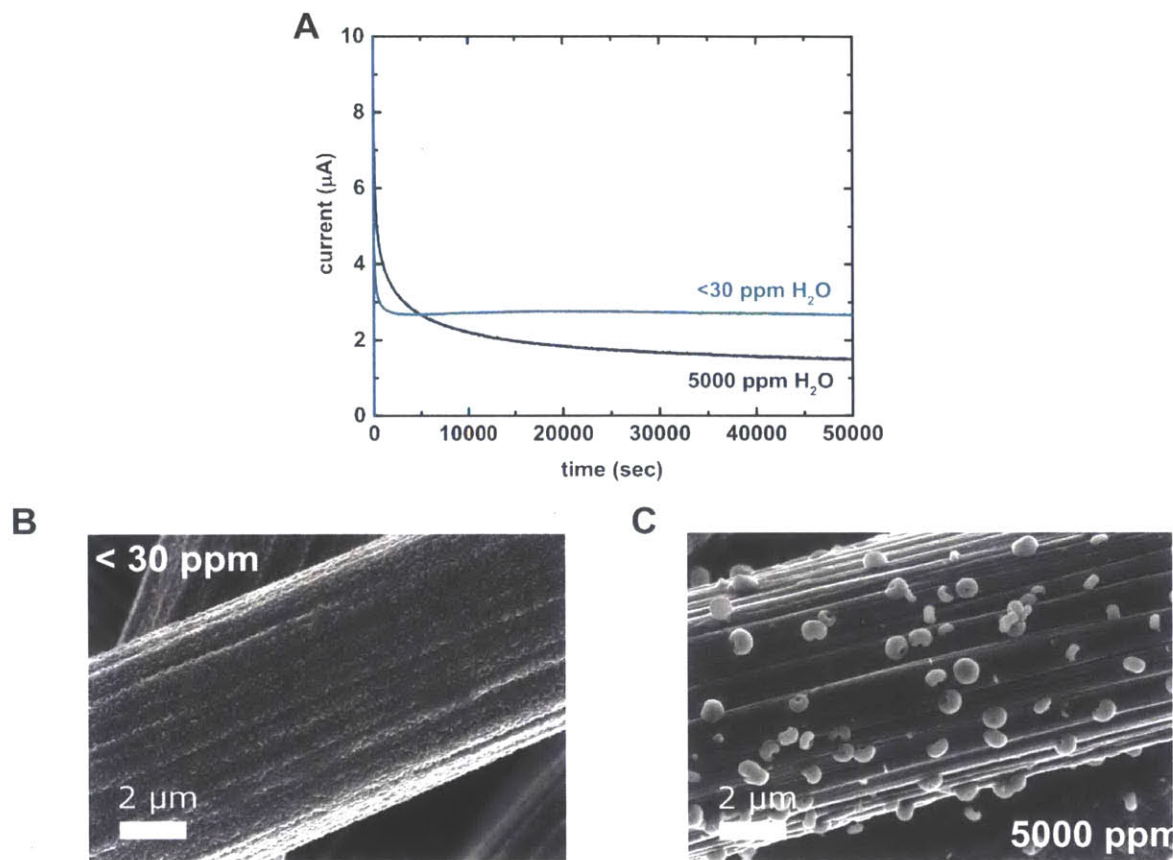


Figure 4-2. (a) Current transient responses to potentiostatic discharge at 2.6 V in 0.1M LiClO₄ in DME with < 30 and 5000 ppm of water (first 50,000 seconds of discharge shown). SEM images of potentiostatically discharged electrodes in 0.1M in LiClO₄ in DME with (b) < 30 ppm and (c) 5000 ppm of water. Both samples were discharged to ~0.055 mAh.

The nucleation and growth rates will be affected both by the activity of surface sites on the electrode and the relative contribution of solvent-mediated chemical processes such as disproportionation of solvated Li⁺-O₂⁻. **Figure 4-2** Figure 4-3 show electrochemical and morphological analysis of Li-O₂ cells with carbon paper electrodes discharged at 2.0 and 2.6 V vs Li⁺/Li in 0.1M LiClO₄ in DME respectively, in both anhydrous electrolyte (< 30 ppm water) and electrolyte with 5000 ppm of water. At 2.6 V, there was a steady current response (**Figure 4-2a**)

regardless of water content. At this potential, the overpotential for Li_2O_2 formation is modest (176 mV compared to the minimum potential for oxygen reduction of 2.76 V vs Li^+/Li in 0.1M LiClO_4 in DME⁷¹), and solution-mediated Li^+-O_2^- disproportionation is expected to be a significant reaction pathway for Li_2O_2 formation.^{102,173} Thus, similarly flat transients in both water-containing and anhydrous electrodes can be explained by the formation of solvated superoxide species that do not readily passivate the surface, but rather disproportionate and aggregate in solution before attaching to the electrode.¹⁰⁴ This is consistent with the formation of toroidal Li_2O_2 morphologies, as observed using *ex situ* Scanning Electron Microscopy (SEM) measurements of the electrodes after potentiostatic discharge. Consistent with previous work,^{109,128} much larger ($\sim 1 \mu\text{m}$) toroids are observed in the electrolyte with 5000 ppm water than in the nominally anhydrous case (**Figure 4-2b-c**). This is likely because water has an exceptionally high acceptor number (AN = 54.8) compared to most organic solvents,⁷⁸ resulting in high solubility of Li^+-O_2^- *via* lowered coupling of Li^+ to O_2^- ¹⁴⁰ which promotes the disproportionation of Li^+-O_2^- to form large, toroidal Li_2O_2 .

At 2.0 V, there is a much larger driving force for oxygen reduction and Li_2O_2 electrodeposition at the electrode surface,¹⁷³ and water clearly reduces Li_2O_2 nucleation and growth rates. In the anhydrous case, the current transient exhibits a monotonic decay from an initial peak at ~ 1.7 mA (Figure 4-3a), which is characteristic of electrodeposition onto a foreign substrate.^{174,175} We attribute this to the growth and impingement of insulating Li_2O_2 particles on the carbon paper surface, with progressively fewer active sites available for oxygen reduction. Upon addition of 5000 ppm of water, there is a longer delay before the peak current is observed, representing a significantly reduced surface Li_2O_2 nucleation rate, and thus a longer amount time until impingement occurs.¹²⁹ *Ex situ* SEM imaging of the electrodes discharged to the same capacity revealed that under anhydrous conditions, Li_2O_2 appeared to conformally coat the fibers

of the carbon paper (Figure 4-3c), while at 5000 ppm of water, toroids and porous deposits (Figure 4-3d) were observed. We confirmed the discharge product to be Li_2O_2 using XRD (Figure 4-4), though we cannot discount the possibility that some of the large deposits may be residual electrolyte. A similar morphological difference (i.e. from conformal coating to larger deposits) has recently been observed for Li_2S electrodeposition on a carbon cloth electrode in the presence of a soluble redox mediator.¹⁷⁰

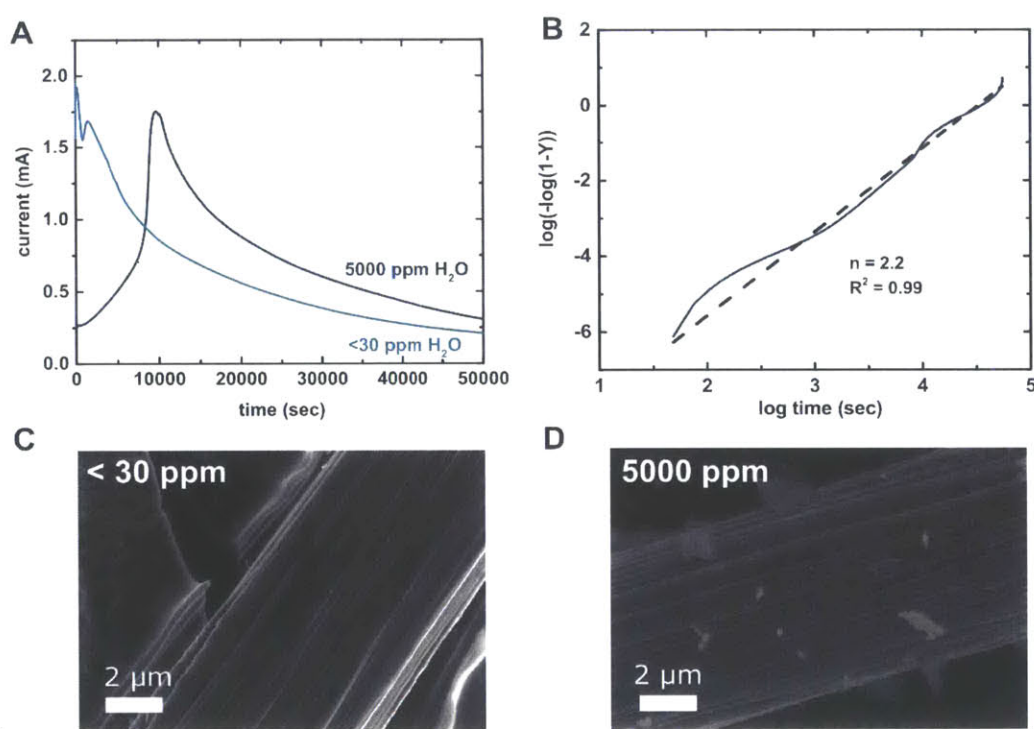


Figure 4-3. Current transient responses to potentiostatic discharge at 2.0 V in 0.1M LiClO_4 in DME with < 30 and 5000 ppm of water (b) Analysis of potentiostatic response in 5000 ppm H_2O to determine the Avrami exponent n , where $Y =$ fraction of species converted and n is the exponent in the Avrami equation $Y = 1 - \exp(-Bt^n)$ where B is a rate constant. SEM images of potentiostatically discharged electrodes in 0.1M LiClO_4 in DME with (c) < 30 ppm and (d) 5000 ppm of water. Both samples were discharged to ~ 10 mAh.

Peaks in the current transient data are clear indicators of surface nucleation and growth processes, though only an approximate quantitative analysis of the effect of water on the dimensionality of Li_2O_2 growth is possible at this time. The data in Figure 4-3 shows that in addition to the peak component, there are other processes that contribute to the observed current transients, including a decaying response at early times seen in the <30ppm H_2O data set, and an extended tail in the response at long times seen in both data sets. It is only the peak component of the current transient that corresponds to surface electron transfer-mediated nucleation and growth.¹⁶⁹ Following Fan *et al.*,¹⁶⁹ the peak component of the data can be analyzed using the Johnson-Mehl-Avrami (JMA) formalism:¹⁷⁶

$$Y = 1 - e^{-Bt^n}$$

where Y is the normalized discharge capacity, t is time, and B and n are a kinetic constant and the Avrami exponent respectively, the latter of which is related to the dimensionality and time dependence of the rates of nucleation and growth. Using an approximate treatment for isolation of the peak component of the 5000ppm H_2O data (see Figure C3 in Appendix C and corresponding discussion) and using a linear fit to a plot of $\log(-\log(1 - Y))$ as a function of t (Figure 4-3b), yields a slope of ~ 2 . This corresponds to an Avrami exponent of ~ 2 and is consistent with a process of simultaneous nucleation and two dimensional growth on the electrode surface, the latter of which was also seen for growth of Li_2S discharge products by Fan *et al.*¹⁶⁹ Extracting more accurate estimates of both the Avrami exponent and nucleation and growth rates is hindered by parallel solvent-mediated processes, such as $\text{Li}^+\text{-O}_2^-$ disproportionation and aggregation of Li_2O_2 growth precursors. The effects of these parallel processes on the current transient must be separately analyzed in order to more accurately isolate the peak component of the current transient for application of the JMA analysis.

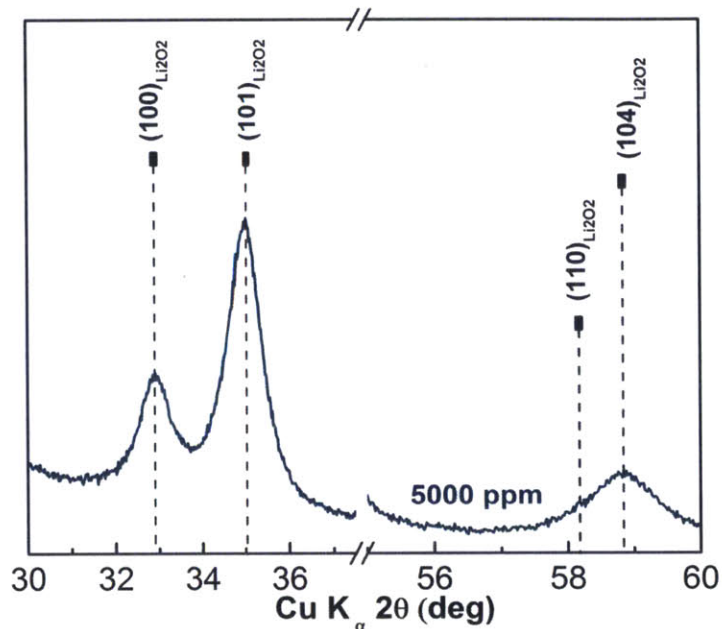


Figure 4-4. XRD pattern of Li-O₂ carbon paper electrode discharged at 2.0 V in 0.1M LiClO₄ in DME with 5000 ppm of water.

4.3.2 The Effect of Water on Li₂O₂ Morphologies in High-Surface-Area CNT Electrodes

We then used CNT electrodes with high specific surface area ($\sim 500 \text{ m}^2/\text{g}$) for detailed studies of Li₂O₂ morphological changes^{71,120} at high gravimetric capacities (Figure 4-5). Previous studies^{109,128} of the impact of water on Li₂O₂ morphology used low specific surface area electrodes, such as carbon paper ($\sim 1 \text{ m}^2/\text{g}$) and Super P ($< 100 \text{ m}^2/\text{g}$) where higher discharge capacities were achieved only upon addition of water. Figure 4-5a shows voltage profiles of CNT electrodes discharged at 25 mA/g_C (milliamperes per gram of carbon) to 4000 mAh/g_C with and without 5000 ppm of water. Both cells exhibited plateaus around $\sim 2.7 \text{ V}$ vs Li⁺/Li, which is characteristic of discharge at low current densities in ether-based electrolytes,^{70,98,147} and produced Li₂O₂ as the

only product detected by X-ray diffraction (Figure C2 and Appendix C). SEM imaging found that in 5000 ppm of water, Li_2O_2 formed in large, toroidal morphologies $\sim 1 \mu\text{m}$ in diameter among the CNTs (Figure 4-5b), while smaller particles ($< 100 \text{ nm}$) were obtained on the CNT electrode surface with no water added (Figure 4-5c). Transmission electron microscopy (TEM) imaging revealed that these small particles did not conformally coat the CNTs, but had disk-like morphologies, resembling early stages of more fully toroidal Li_2O_2 (Figure 4-5d).¹²⁰

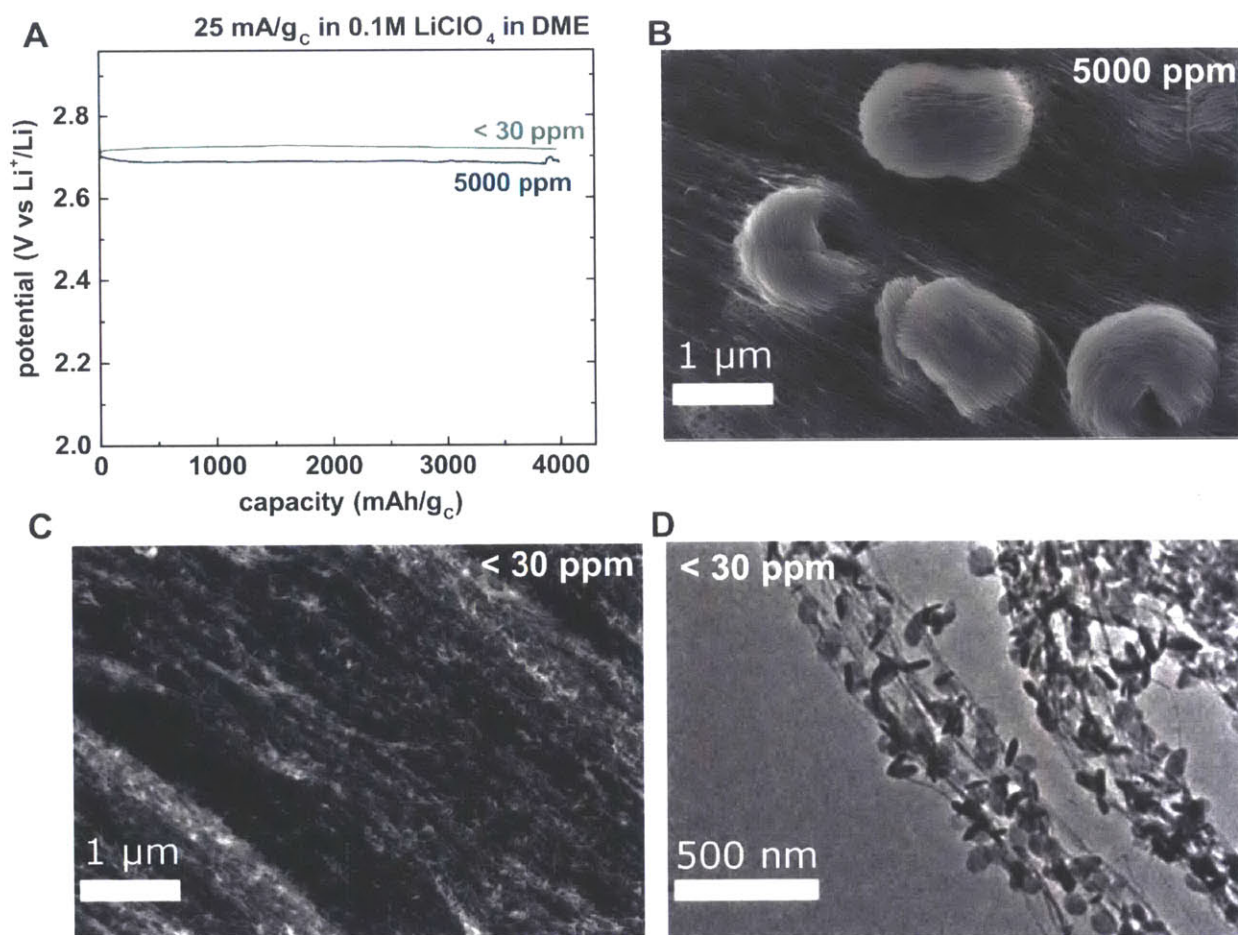


Figure 4-5. (a) Galvanostatic Li-O_2 discharge curves of CNT electrodes at 25 mA/g_c to 4000 mAh/g_c in 0.1 M LiClO_4 in DME with 5000 and $< 30 \text{ ppm}$ of water. SEM images of CNTs

discharged in 0.1M LiClO₄ in DME with (b) 5000 ppm and (c) < 30 ppm of water. (d) TEM images from CNT discharged in 0.1M LiClO₄ in DME with < 30 ppm of water.

Cell leakage or ambient air intrusion cannot be responsible for the phenomena observed in Figure 4-5, although the discharge experiments took a week each. Schwenke *et al.*¹²⁸ noted that the sensitivity of Li-O₂ cell discharge capacity and Li₂O₂ morphology increased with discharge time, and speculated that over the course of long discharge tests (lasting days or weeks), toroid growth is likely even in initially water-free cells, due to minute rates of water intrusion from ambient air. In addition, Guo *et al.*¹⁶⁴ have shown that discharge under moderate relative humidity (RH = 15%) results in the formation of toroidal Li₂O₂. In our study, however, since *both* water-free and water-containing Li-O₂ cells were discharged to the same capacity, they would have been subject to similar leakage/water accumulation rates. Thus, if the Li₂O₂ morphology were predominantly influenced by water, similar morphologies should have been observed in both cases; which is clearly not the case (Figure 4-5b-c). Moreover, all cells used were pressurized with O₂ to ~25 psi gage, thus making ingress of atmosphere unlikely. Furthermore, assuming that ambient water entered the cell at the rate of cell leakage, it would take ~ 20,000 h of discharge for the water content of an initially water-free cell to approach 5000 ppm, which is two orders of magnitude greater than the actual discharge time of 160 h (calculations in Appendix C).

We further show that the addition of up to 5000 ppm of water does not increase the terminal discharge capacity of CNT electrodes used in this study, but does increase Li₂O₂ toroid size at low rates (Figure 4-6). Figure 4-6a-b show Li-O₂ discharge profiles at gravimetric rates of 25, 250 and 500 mA/g_C with and without 5000 ppm of water in the electrolyte. Discharge capacities at 25 and 250 mA/g_C were between ~ 10000 and 12500 mAh/g_C regardless of water content, which stands

in contrast to behavior observed in lower surface area carbon paper¹²⁸ and VC electrodes,^{109,157} where substantially higher capacities were observed upon the addition of water. SEM imaging of CNT electrodes discharged at 25 mA/g_c to full capacity in DME (Figure 4-6c-d) revealed that large toroids were formed in the presence of 5000 ppm of water while much smaller particles formed in its absence.

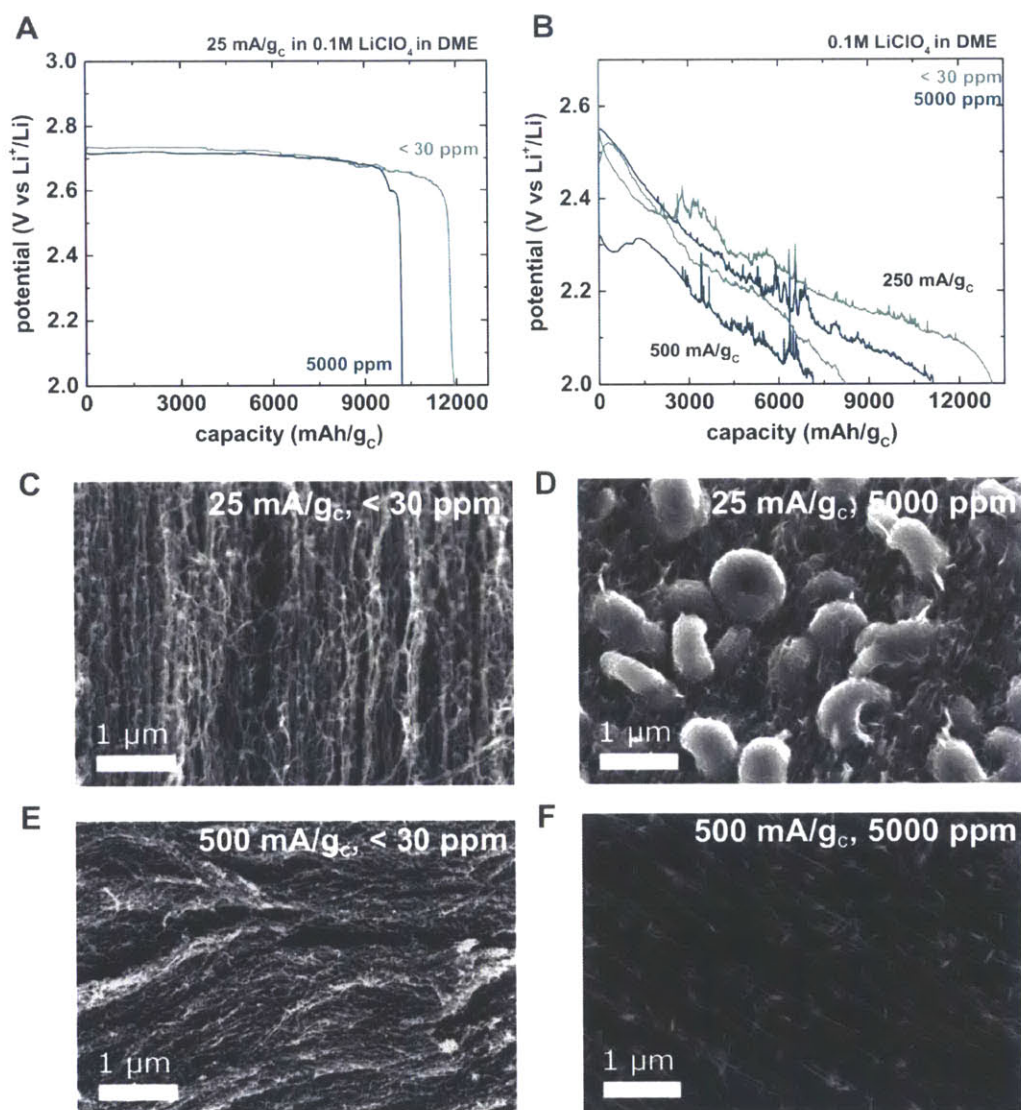


Figure 4-6. Galvanostatic Li-O₂ discharge curves of CNT electrodes at (a) 25 and (b,c) 250 and 500 mA/g_c in 0.1M LiClO₄ in DME with 5000 and < 30 ppm of water. *Ex situ* SEM images of

Li-O₂ electrodes discharged at (c,d) 25 and (e,f) 500 mA/g_c in < 30 and 5000ppm of water.

We rationalize this observation with the following arguments. It is hypothesized that the maximum discharge capacity is reached when all sites available for the ORR and nucleation of Li₂O₂ are passivated. High-surface-area CNT electrodes have an excess of highly active sites for ORR and Li₂O₂ nucleation, which results in a high driving force for surface attachment of reduced oxygen species. Thus, the introduction of water only marginally decreases the surface nucleation rate, causing the growth of more Li₂O₂ toroids that are observable by SEM (Figure 4-6d,f), but little change in the maximum discharge capacity (Figure 4-6a-b), since observable toroids comprise a small fraction of the overall discharge capacity.¹¹⁷ On the other hand, low-surface-area electrodes such as carbon paper have fewer defects and less active sites for surface Li₂O₂ nucleation, in which case adding water to the electrolyte leads to a substantial decrease in the surface nucleation rate, and higher discharge capacities (Figure 4-7).¹²⁸

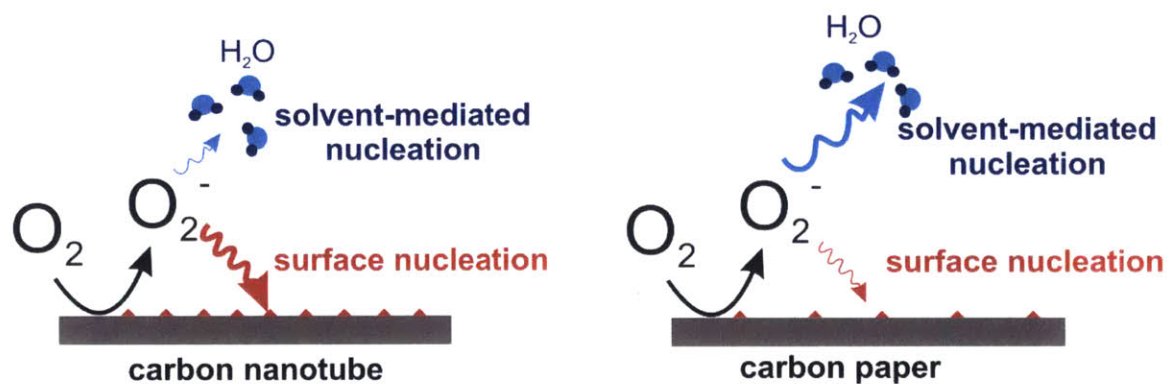


Figure 4-7. Schematic illustrating competition between surface and solvent-mediated nucleation of Li₂O₂ in the presence of water, which is modulated by electrode surface site concentration and activity. In the presence of water, high concentration and activity of surface sites in CNTs results

in greater surface-mediated nucleation, while lower concentration and activity of surface sites in carbon paper results in more solvent-mediated Li_2O_2 nucleation.

The above hypothesis is supported by a number of experimental observations. That CNT electrodes have an excess of highly active sites for ORR and nucleation compared to carbon paper is supported by Raman spectra of pristine electrodes, showing a higher D/G band ratio in CNTs than in carbon paper (Figure 4-8).

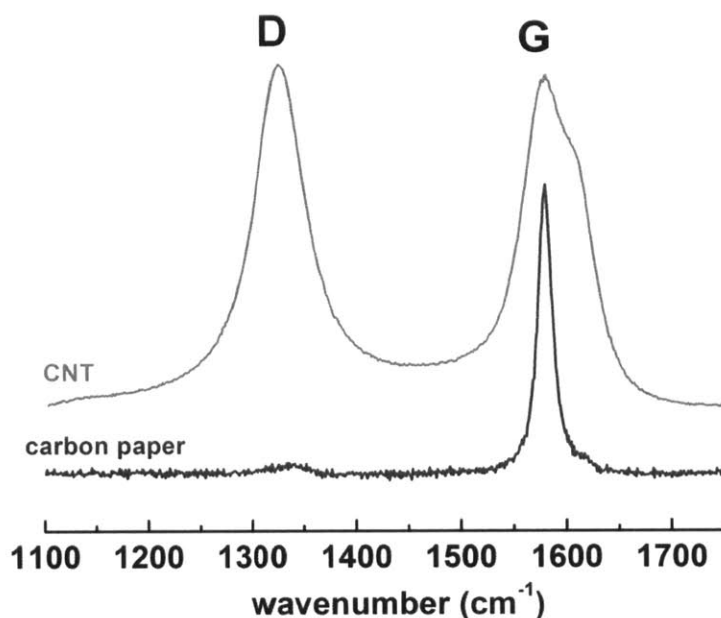


Figure 4-8. Raman spectra of pristine CNT and carbon paper electrodes, showing D and G bands from carbon.

This is consistent with the presence of more disorder in the CNT sp^2 carbon,¹⁷⁷ and thus more defects that can serve as ORR sites.¹⁵⁵ The presence of more active ORR sites results in

Brunauer-Emmett-Teller (BET)-normalized discharge capacities for CNTs at BET current rates $< 100 \mu\text{A}/\text{m}^2_{\text{BET}}$ about an order of magnitude higher than those in Vulcan carbon and carbon paper used in studies by Lau,¹¹⁷ Schwenke,¹²⁸ Adams⁷⁰ and co-workers (Figure 4-8). It is additionally worth noting that even with the addition of 1000 ppm – 1% (i.e. 10,000 ppm) of water, the BET-normalized capacity of carbon paper ($\sim 100 \text{mAh}/\text{m}^2_{\text{BET}}$) is less than that of CNTs ($250 \text{mAh}/\text{m}^2_{\text{BET}}$) without water. Lastly, that terminal discharge capacities are dictated by ORR sites on the electrode surface rather than electrode void volume is supported by calculations showing that the expected capacity from pore filling ($\sim 100,000 \text{mAh}/\text{g}_\text{C}$, see Appendix C) is an order of magnitude greater than actual capacities obtained.

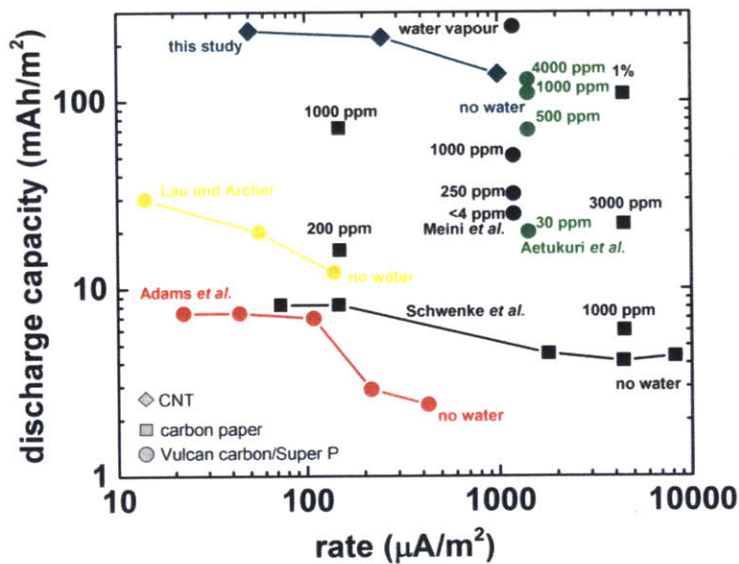


Figure 4-9. First discharge capacity as a function of current density and water content in the catholyte of cells with carbon paper (squares), VC/Super P (circles) and CNT (diamond)-based electrodes and glyme-based solvents, with assumed specific surface areas of 1, 100 and 500 m^2/g respectively. A similar plot is reported in the study by Schwenke *et al.*¹²⁸ with the data of Adams *et al.*⁷⁰ Data from Meini,¹⁵⁷ Lau,¹¹⁷ Aetukuri¹⁰⁹ and co-workers have been added for comparison.

4.3.3 The Influence of Water pKa and Solvation on the Reaction Product Chemistry – LiOH vs. Li₂O₂

We now show that adding water to a MeCN-based electrolyte leads to the formation of LiOH (Figure 4-10). Figure 4-10a shows discharge curves for Li-O₂ CNT electrodes discharged at 25 mA/g_c to ~4000 mAh/g_c in 0.1 M LiClO₄ in MeCN with and without 5000 ppm of water. Since MeCN reacts violently with Li, a LiCoO₂-based anode was used instead of Li metal. In MeCN, the presence of water in the electrolyte induces an increase in the discharge potential and a change in discharge product chemistry, from Li₂O₂ to a mixture of LiOH and Li₂O₂ (Figure 4-10b).

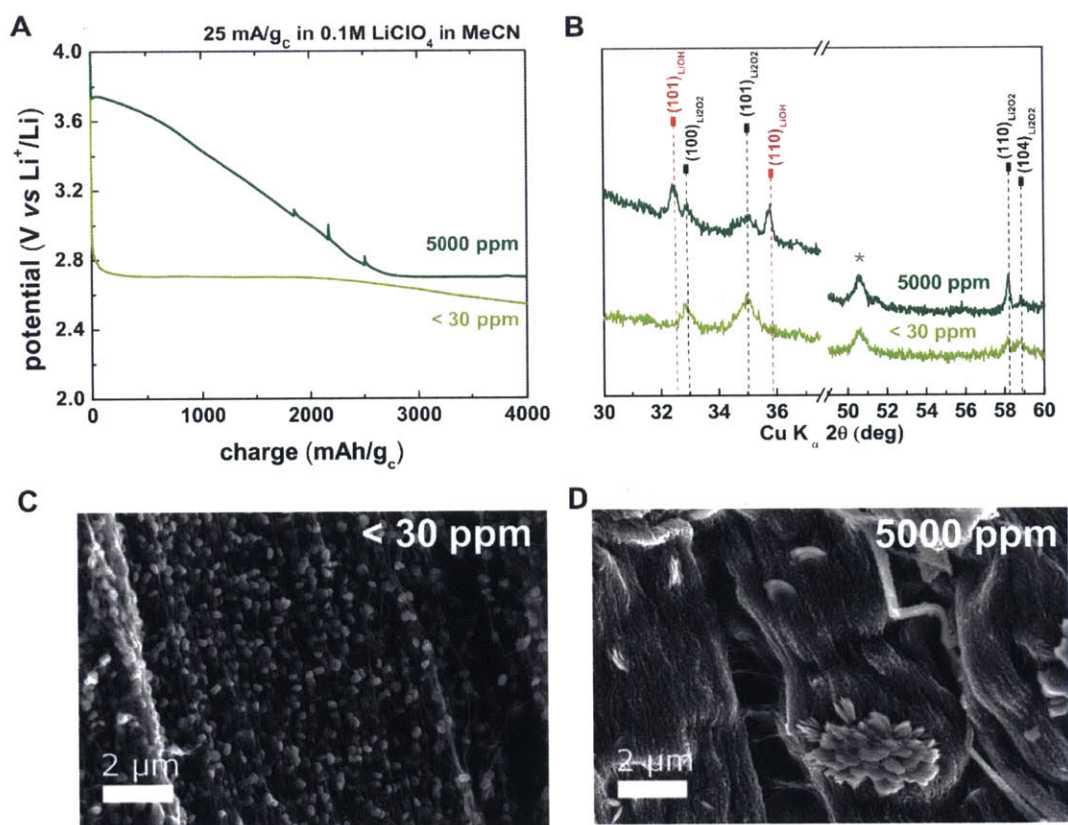


Figure 4-10. (a) Galvanostatic and (b) *ex situ* XRD measurements of Li-O₂ CNT electrodes discharged at 25 mA/g_c to 4000 mAh/g_c in 0.1M LiClO₄ in MeCN with 5000 and < 30 ppm of water. SEM images of CNTs discharged in 0.1M LiClO₄ in MeCN with (c) < 30 and (d) 5000 ppm

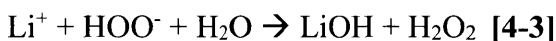
of water. The discharge potential in (a) is calculated assuming Li removal from LiCoO₂ occurs around 3.9 V vs Li⁺/Li.

SEM imaging clearly shows a corresponding change in morphology, from mainly toroidal (Figure 4-10c) to ~ 1 – 2 μm flower-like features (Figure 4-10d).

The formation of LiOH in water-containing MeCN electrolyte suggests that water or protons from water are consumed during discharge. In addition, water induces an increase in the discharge potential above ~3 V vs Li⁺/Li, which is consistent with O₂⁻ produced during the ORR (O₂ + e⁻ → O₂⁻) inducing deprotonation of water (H₂O → OH⁻ + H⁺) to form the hydroperoxyl radicals, as shown in reaction 1: ^{165,167,168}



The formation of LiOH can proceed from HOO[·] *via* the following reactions in the presence of Li⁺:



A competing pathway for LiOH formation after reaction 1 is direct reaction between Li⁺ and OH⁻ ions left over from water deprotonation.

A critical question is why LiOH is not formed in the presence of water-containing DME, but is in DMSO^{37,110} and, as now shown here, MeCN. This puzzle was raised by Schwenke *et al.*¹²⁸ previously, and is relevant to the current study. We believe that the main parameter determining discharge product chemistry (i.e. Li₂O₂/LiOH) is the tendency for the electrolyte to be deprotonated in the presence of superoxide, which, in this case, is influenced by proton availability from water. This hypothesis is supported by the fact that O₂⁻ disproportionation in the presence of

Brønsted acids is accelerated in proportion to the protic strength of the acid,^{178,179} which can vary in different solvents.^{166,167,180}

To examine the protic strength of water in different solvents, we calculated effective pKa values for water in DME, MeCN, DMF and DMA using first principles calculations, according to the equation:

$$pKa = \frac{\Delta G_{deprotonation}}{2.303RT} \quad [4-4]$$

where $\Delta G_{deprotonation}$ was estimated following the thermodynamic cycle in Figure 4-1. As shown in Table 4-1, the pKa value of water in MeCN using the M06L functional is 35.2 respectively, while that for water in DME is > 47.0 . This clearly suggests a greater tendency for superoxide-induced water dissociation in the former solvent than the latter, and accounts for LiOH formation after Li-O₂ discharge when they are used as electrolyte solvents.

Table 4-1. Computed pKa of water in DME, MeCN, DMF and DMA.

Solvent	Method/Basis set	
	B3LYP/6-31G(d,p)	M06L/6-311++G(d,p)//B3LYP/6-31G(d,p)
DME	$\geq 57.7^*$	$\geq 47.0^*$
MeCN	40.0	35.2
DMF	48.0	42.1
DMA	51.1	44.4

* Calculations assume that $\Delta G_s(H^+)$ in DME, though expected to be lower (smaller in absolute value), is the same as that in DMSO, leading to the lower bound of computed pKa of water in DME.

We note that experimental pKa values for water in organic solvents (e.g. 31.4 in DMSO¹⁸¹) can be lower than pKa values of the solvents themselves (e.g. 35 in DMSO¹⁸²), demonstrating that water can be a better proton donor than the solvents, and is consistent with the idea that the effective acidity of water is critical for enabling reaction [4-1].

It is important to note that an alternative to pathway to LiOH formation could begin with a direct reaction between Li₂O₂ and H₂O (Li₂O₂ + H₂O → LiOH + H₂O₂) in much the same way DMSO itself is likely to undergo deprotonation by Li₂O₂.³⁷ Schwenke *et al.*¹²⁸ point out that the free energy this reaction is in fact positive (+40 kJ/mol), however as Li₂O₂ is known to dissolve in aqueous solutions, it is likely that it may partially dissociate in water-doped electrolyte, giving rise to highly basic peroxide ions, which would then very easily deprotonate water. This could then result in the formation of hydroperoxyl monoanion (LiOOH), leading to LiOH formation *via* reactions [4-2] and [4-3].

We also calculated the solvation free energy of water in various solvents (Table C 2 in Appendix C), and found that they correlated with the differences in discharge product morphology between water-free and water-containing electrodes. Namely, greater (more negative) solvation energies of water (such as in MeCN, ~ -17 kJ/mol) promote less toroidal Li₂O₂ upon water addition than less solvation (DME, -12 kJ/mol). This difference is evident in the study by Aetukuri *et al.*,¹⁰⁹ who showed similarly drastic morphological changes in DME, but noted that in DMSO, while water promoted the formation of larger toroids, small Li₂O₂ toroids could be observed even in electrodes discharged under anhydrous conditions. This point can be appreciated by comparing the drastic morphological differences between the small (< 100 nm) Li₂O₂ particles formed in water-free (Figure 4-5c and Figure 4-6c) vs large toroids in water-containing electrodes in DME (Figure

4-5b and Figure 4-6d) to the smaller differences between discharge product in water-free and watery DMSO,¹⁰⁹ where the solvation of water is expected to be high.¹⁶⁷ We hypothesize that less strongly solvated water molecules in DME would be freer to solvate or otherwise interact with evolving growth precursors of Li_2O_2 , resulting in their solubilization and the growth of larger Li_2O_2 . On the other hand, more strongly solvated water molecules would be less activated, and would exert a smaller effect on final Li_2O_2 morphologies.

Thus, the effective pKa and solvation energy of water in various electrolyte solvents can explain whether Li_2O_2 or LiOH should be formed, and their morphology, respectively (Figure 4-11b): lower pKa values of water result in greater proton availabilities and the formation of LiOH , while weak solvation of water molecules results in more toroidal Li_2O_2 morphologies, notably in DME, in which water has a high pKa and lower solvation energy.

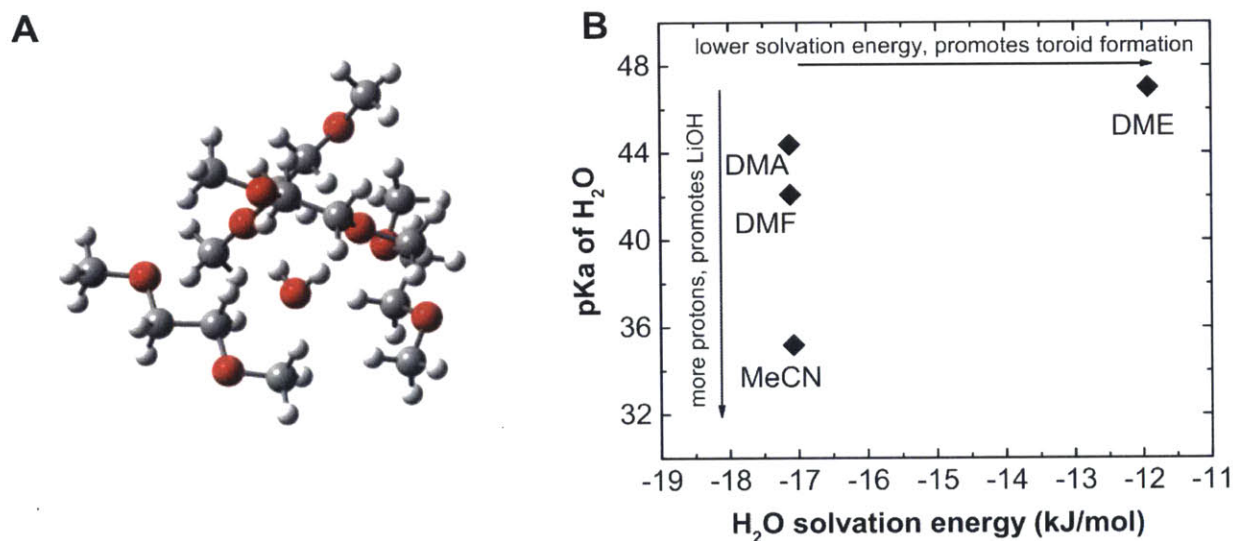


Figure 4-11. (a) Optimized structure of four DME solvent molecules surrounding water molecule. Color code: Red = Oxygen; Grey = Carbon; White = Hydrogen. (b) Plot showing relationship between computed pKa and solvation free energy of water in DME, MeCN, DMF and DMA. pKa

values were obtained from single point energy calculations at the M06L/6-311++G(d,p) level of theory performed on molecular structures fully optimized at B3LYP/6-31G(d,p) level.

This trend provides a useful vantage point for rationalizing the role of electrolyte additives on Li-O₂ growth and chemistry, but also in metal-air chemistries such as Na-O₂, where water has been shown to promote large cubic NaO₂ morphologies on discharge.¹⁸³ Likewise, the formation of LiOH has been reported in Li-O₂ batteries upon the addition of LiI to the electrolyte,^{184–186} and using Ru and/or MnO₂-loaded carbon electrodes.^{187,188} Understanding these chemical trends in terms of the effective acidities of electrolyte additives or even electrode surfaces¹⁸⁹ may prove fruitful for designing metal-air batteries tailored for a large variety of discharge product chemistries. More detailed future studies would be required to build upon and test these admittedly speculative ideas.

4.4 Conclusions

In summary, we show using electrochemical tests and direct observation of discharge product morphology, that the presence of water in DME-based electrolyte decreases the surface Li₂O₂ nucleation rate during Li-O₂ battery discharge, which is responsible for the previously observed formation of large Li₂O₂ growth morphologies and capacity increases. We also show that as proton availability from, and the activity of water increase, discharge product chemistry and morphology are biased toward LiOH and larger toroids, respectively. We support these claims

using first principles calculations of the effective pKa and solvation of water in a range of candidate electrolyte solvents. Combining electrokinetic and morphological analyses with first principles calculations has the potential to elucidate relationships between electrolyte/electrode surface composition and discharge product chemistry and growth mechanisms.

In Li-O₂ battery configurations where discharge product chemistry evolves over time, however, other approaches are required. This scenario is explored in **Chapter 5**, where the reactivity of discharged Li₂O₂ with DMSO is examined. In this case, controlled aging of discharge product in contact with the electrolyte, and the use of model chemical reactions can shed light on slow decomposition processes that traditional electrochemical techniques are not sensitive enough to elucidate.

Chapter 5: Chemical Instability of Dimethyl Sulfoxide in Li-O₂ Batteries

Reproduced in part with permission from David G. Kwabi, Thomas P. Batcho, Chibueze V. Amanchukwu, Nagore Ortiz-Vitoriano, Paula Hammond, Carl V. Thompson, and Yang Shao-Horn, Chemical Instability of Dimethyl Sulfoxide in Lithium-Air Batteries. *Journal of Physical Chemistry Letters*. **2014**, 5, 16, 2850-2856 (Copyright 2016, American Chemical Society)

5.1 Introduction

One of the most prominent challenges to the practical implementation of Li-O₂ batteries is the chemical instability of aprotic electrolytes^{41,190-192} and oxygen electrodes (e.g. carbon^{14,15,53,56}) toward ORR species (O₂⁻ and O₂²⁻) during both discharge and charge. Electrolyte and electrode oxidation typically results in the formation and build-up of resistive species during cell cycling, which contributes to low round-trip efficiency, poor rate capability and poor cycle life. The use of DMSO in Li-O₂ batteries has been shown to increase the solubility of reaction intermediates during discharge and strongly influence reaction mechanisms for Li₂O₂ formation, in **Chapters 2** and **3**. Recent reports have also suggested that DMSO-based electrolytes support the reversible formation of Li₂O₂ for up to ~100 cycles when combined with nanoporous Au¹⁵ or TiC⁵⁶ as the oxygen electrode. However, it is well known that DMSO is susceptible to oxidation by superoxide anions¹⁹³ such as in HO₂¹⁹⁴ and KO₂^{111,195} and by electrochemical oxidation¹¹¹ to produce dimethyl sulfone (DMSO₂). Moreover, several recent studies have reported the formation of LiOH in addition to Li₂O₂ with carbon-based cathodes in DMSO-based electrolytes,^{37,97,98,151} where the ratio of Li₂O₂ to LiOH vastly varies among these studies. While it has been suggested that trace

water in aprotic electrolytes containing ether-based solvents can lead to the formation of LiOH¹⁵⁷ via a reaction between Li₂O₂ and water ($Li_2O_2 + 2H_2O \rightarrow 2LiOH + H_2O_2$), we have shown in **Chapter 4** that the formation of LiOH is critically dependent on the pK_a of water in the electrolyte solvent, which is higher in DME than other commonly used organic solvents. One compelling explanation for the formation of considerable amounts of LiOH upon Li-O₂ cell discharge in DMSO is the chemical reactivity between species formed in the oxygen electrode upon discharge (e.g. Li₂O₂, solid-state^{71,132,138} and soluble⁶⁶ superoxide species) and DMSO itself. While Sharon *et al.*³⁷ have suggested that both Li₂O₂ and superoxide-like species can react with DMSO to form DMSO₂ and LiOH, Fourier transform infrared spectroscopy (FT-IR) detects no DMSO₂ after 2 months of prolonged exposure of Li₂O₂ in DMSO,¹¹¹ and factors that can influence relative amounts of LiOH and Li₂O₂ formed upon discharge of Li-O₂ cells, and conditions under which commercial Li₂O₂ powder can react with DMSO to form DMSO₂ and LiOH are not completely understood.

In this chapter, we examine the chemical stability of DMSO upon exposure to electrochemically formed Li₂O₂ on CNT oxygen electrodes, and commercial Li₂O₂ with and without KO₂, which acts as source of superoxide anions. We find that toroidal Li₂O₂ particles formed immediately after discharge gradually convert to LiOH upon exposure to the electrolyte and only LiOH was found upon prolonged exposure (380 hours). In addition, gas chromatography with mass spectroscopy (GC-MS) with greater sensitivity than FT-IR measurements clearly revealed the formation of DMSO₂ and thus the chemical instability of DMSO upon prolonged exposure of DMSO in presence of commercial Li₂O₂ powder. Moreover, the addition of KO₂ to the mixture of DMSO and Li₂O₂ accelerates the formation of LiOH and DMSO₂.

5.2 Experimental Methods

5.2.1 Electrochemical Measurements

Li-O₂ cells consisted of a lithium metal anode and freestanding vertically aligned few-walled CNTs (detailed preparation of the nanotubes have been previously reported^{14,120}) as the O₂ electrode (~ 1 × 1 cm). After weighing and vacuum-drying at 100 °C for 8 h, the electrodes were transferred to a glove box (H₂O < 0.1 ppm, O₂ < 0.1 ppm, Mbraun, USA) without exposure to ambient. Carbon loadings were about 0.5-1 mg/cm² and all cells were assembled with 0.1 M LiClO₄ in DMSO (H₂O < 30 ppm, BASF, USA). Cells were assembled with a lithium foil anode (Chemetall, Germany, 15 mm in diameter) and a Whatman GF/A separator soaked in 120 μl of electrolyte. A stainless steel mesh was used as the current collector. Following assembly, cells were transferred to a connected second argon glove box (Mbraun, USA, H₂O < 1 ppm, O₂ < 1%) without exposure to air and purged for 5 min with dry O₂ (99.994 pure O₂, Airgas, H₂O < 2 ppm). At the end of purging, the cells were pressurized to 25 psi (gage) to ensure that an adequate amount of O₂ was available to cells. Electrochemical tests were conducted using a Biologic VMP3. Galvanostatic discharge tests were performed by first resting at open circuit (~2.9 – 3.2 V vs Li⁺/Li) for 4 hours before applying current.

5.2.2 Ball-milling of commercial Li₂O₂

Ball-milling of commercial Li₂O₂ (Sigma Aldrich, St. Louis, USA) was done in a zirconium oxide milling crucible using a planetary ball mill (Pulverisette 6, Fritch Inc.) at 500

rpm at 15 hours, reversing every 30 minutes. Milling reversal was preceded by a 15-minute cooling phase. One-millimeter zirconia milling balls were dispersed in the Li_2O_2 powder prior to milling.

5.2.3 *Mixing of suspensions containing Li_2O_2 and KO_2 in DMSO*

Mixing of Li_2O_2 (ball-milled) and commercial KO_2 (Sigma Aldrich) in DMSO was performed in a nitrogen-filled glove box ($\text{H}_2\text{O} < 0.1$ ppm, $\text{O}_2 < 5$ ppm, Mbraun, USA). To obtain a 1:100 Li_2O_2 :DMSO ratio, 40 mg of commercial (ball-milled) Li_2O_2 was added to a 20 ml scintillation vial, followed by 6.2 ml of neat DMSO (4 ppm H_2O). For the experiment involving KO_2 , an additional 63 mg of commercial KO_2 was added to another 1:100 Li_2O_2 : DMSO mixture to obtain a 1:1:100 molar ratio of Li_2O_2 : KO_2 :DMSO. The resulting suspensions were stirred using a magnetic stir bar for the duration of the experiment. After 500 hours of mixing, each suspension was centrifuged and the resulting solids were collected and dried under vacuum overnight for analysis by XRD and Raman spectroscopy. The remaining liquid supernatant was analyzed by GC-MS.

5.2.4 *X-ray Diffraction Characterization*

XRD measurements on electrochemically discharged electrodes were conducted using a Rigaku Smartlab (Rigaku, Salem, NH) in the surface-sensitive parallel beam configuration. For XRD measurements taken immediately after discharge, the CNT electrode was extracted from the Li- O_2 cell immediately after discharge in an argon-filled glove box and sealed in an air-tight XRD sample holder (Anton Paar, Graz, Austria) with a dome that screwed on with a rubber O-ring fitting before being taken to the X-ray diffractometer in order to minimize exposure to atmospheric

contaminants. CNT electrodes that were aged in the electrolyte for extended periods were left in a capped vial together with the separator in an argon-filled glove box for the desired amount of time, before the XRD measurement. Solid precipitates extracted from suspensions containing Li_2O_2 and KO_2 in DMSO were analyzed on a Bruker Advance II diffractometer (Bruker, Billerica, MA) in the conventional Bragg-Brentano geometry. Samples were sealed in an air-tight holder (Bruker, Billerica, MA) with a dome that screwed on with a rubber O-ring fitting to avoid exposure to atmospheric contaminants.

5.2.5 Raman, FT-IR Spectroscopy and GC-MS Measurements

Raman spectroscopy was performed on the solid components of suspensions containing Li_2O_2 with and without KO_2 in DMSO on a LabRAM HR800 microscope (Horiba Jobin Yvon) using an external 20 mW He:Ne 633 nm laser (Horiba, Jobin Yvon), focused with a 50 \times long working distance objective and a $10^{-0.3}$ neutral density filter. A silicon substrate was used to calibrate the Raman shift. FT-IR was used to analyze soluble DMSO decomposition species in suspensions containing Li_2O_2 with and without KO_2 in DMSO. To analyze the mixtures, 10 μl of each suspension was deposited on a transparent KBr Infrared card (International Crystal Laboratories, USA) and removed from the nitrogen glove box. A JASCO 4100 Fourier Transform Infrared spectrometer (JASCO Analytical Instruments, USA) was then used at a resolution of 1 cm^{-1} and 100 accumulation scans to perform the measurements. GC-MS was used to examine molar masses of solution-based species related to DMSO decomposition. This was carried out on an Agilent 5973 Network Mass Selective Detector (Agilent Technologies, Santa Clara, CA). The supernatant obtained from centrifugation of suspensions containing Li_2O_2 with and without KO_2 in DMSO was mixed in excess acetonitrile, which was used as the carrier gas for GC-MS. 1 μl of

analyte was injected into the GC inlet, which was heated in progressive stages, beginning from 100 °C for 5 min to 250 °C for 3 min and, finally, 320 °C for 8 min, ramping between temperature set points at 20 and 30 °C/min respectively. Mass analysis was performed between 2 and 600 atomic mass units (a.m.u).

5.2.6 SEM Characterization

SEM images were taken using a Zeiss Supra55VP and Ultra55 (Carl Zeiss AG, Germany). Images were taken with an Inlens detector at 5 kV working voltage. To minimize air exposure, samples were sealed and stored in argon before being quickly placed into the SEM chamber. EDS was carried out on the Zeiss Supra 55VP with an EDAX EDS system (Ametek Inc., USA).

5.3 Results

5.3.1 Reactivity between electrochemically formed Li_2O_2 and DMSO

We first show that only Li_2O_2 was formed in lab-scale Li-O₂ cells after discharge, which was converted to LiOH in DMSO over time. Figure 5-1a shows X-ray diffraction (XRD) patterns of CNT-based electrodes discharged at 100 mA/g_C (i.e. 100 mA per gram of CNTs) to ~ 3000 mAh/g_C, and exposed to 0.1 M LiClO₄ in DMSO electrolyte for different amounts of time. While only Li_2O_2 was detected immediately after discharge (i.e. aged 0.5 hours), only LiOH was found after 380 hours of aging in contact with the electrolyte. It is likely that different resting/aging times

for the discharged electrodes between the end of discharge and XRD measurements in previous studies^{37,97,98,151}, which is not reported and not typically monitored, influences the relative amounts of LiOH and Li₂O₂ reported for electrodes discharged in DMSO-based electrolytes.

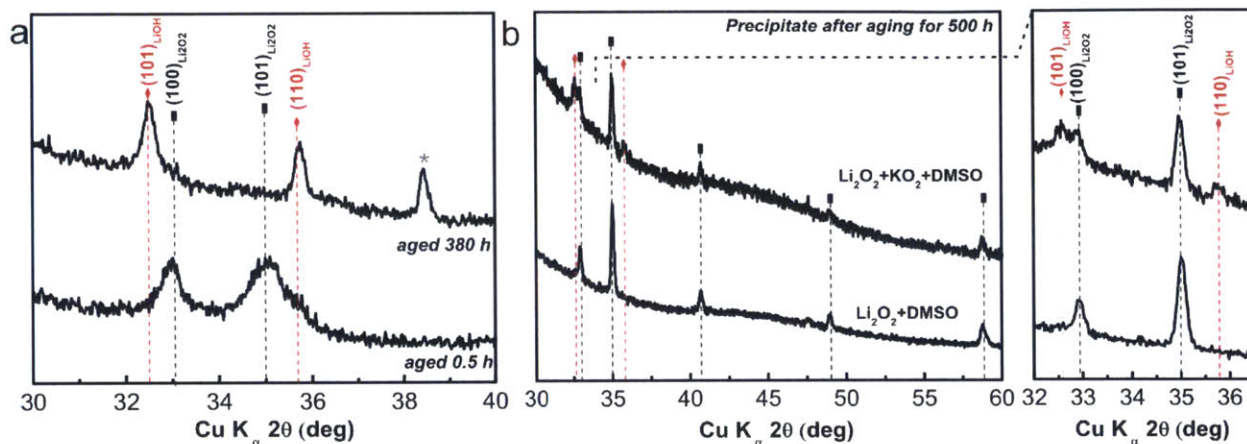


Figure 5-1. XRD patterns showing evolution of LiOH (red dashed lines) from (a) Li₂O₂ in a CNT electrode discharged at 100 mA/g_C to ~3000 mAh/g_C in 0.1 M LiClO₄ in DMSO after 0.5 h and 380 h of aging in electrolyte following the completion of discharge. The grey asterisk denotes a peak from the Al substrate. (b) Solid precipitates collected after centrifugation of suspensions containing commercial Li₂O₂, KO₂ and DMSO and Li₂O₂ and DMSO in mole ratios of 1:1:100 and 1:100 respectively after 500 hours of continuous stirring. The magnified section shows major peaks for Li₂O₂ and LiOH.

The conversion of Li₂O₂ to LiOH was accompanied by considerable morphological changes. Toroidal or disc-like Li₂O₂ particles (Figure 5-2a, marked by small circles) on the order of ~500 nm were found as the majority feature together with a few flake-like particles (Figure 5-2a, marked by large circles) immediately after discharge in 0.1 M LiClO₄ in DMSO. Similar toroidal morphologies have been reported for Li₂O₂ formed in ether-based

electrolytes^{12,55,71,118,120,138} upon discharge at low overpotentials (> 2.7 V vs Li^+/Li) and current densities. The number of flake-like particles (**Figure 5-2b-c**) was found to increase with increasing exposure to the DMSO electrolyte after 12 and 24 hours, finally becoming the dominant feature after 576 hours (**Figure 5-2d**). We attribute these flake-like particles to LiOH based on: (i) such particles not being present in pristine CNTs soaked in 0.1 M LiClO_4 in DMSO (Figure S1) (ii) XRD results showing the conversion from Li_2O_2 to LiOH with increasing exposure to DMSO (Figure 5-1) and (iii) energy dispersive X-ray (EDS) spectroscopy of the flake-like particles, revealing that they were not precipitates from the electrolyte salt (Figure D 1). This hypothesis is also supported by findings of Xu *et al.*,¹⁵² which show that the use of a tetramethylene sulfone-based electrolyte suppresses both the formation of flake-like particles *and* the appearance of LiOH, as compared to discharge in a DMSO-based electrolyte.

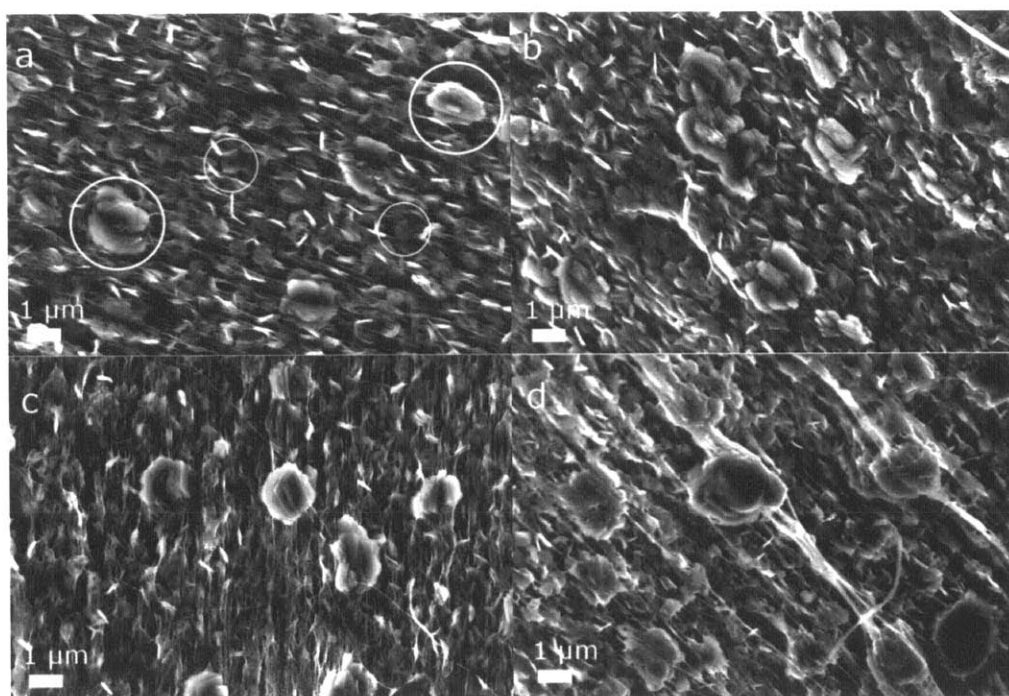


Figure 5-2. Scanning Electron Microscopy (SEM) images of CNT electrodes discharged at 25 mA/gc to ~ 4000 mAh/gc in 0.1 M LiClO_4 in DMSO imaged (a) 0.5 hours (b) 12 hours (c) 24 hours

(d) 576 hours after discharge. Examples of LiOH particles are marked by large circles and examples of Li₂O₂ discs by smaller circles.

The formation of LiOH cannot result from the reactivity between Li₂O₂ and H₂O in the pristine electrolyte as proposed earlier¹⁵⁷ as Karl-Fisher titration on the pristine electrolyte revealed a water content of 18 ppm, which is ~500 times smaller than that required for direct conversion of discharged Li₂O₂ to LiOH (see Appendix D for details of this calculation). A similar conclusion was reached by Trahan *et al.*⁹⁸ The addition of H₂O from ambient during discharge is negligible as the cell has insignificant cell leakage (~0.5 psi per day, see discussion in Appendix C), which is supported by the fact that Li₂O₂ is formed invariably upon first discharge^{14,71,120} with no LiOH peaks present in XRD with an electrolyte comprised of 0.1 M LiClO₄ in DME (see **Chapter 3**). This observation is in agreement with previous studies of Li-O₂ cathodes discharged in ether-based electrolytes.^{12,41,118} Further support comes from the fact that the Li metal anode in each cell exhibited no signs of corrosion or discoloration after discharge. Therefore, it is proposed that the observed conversion from Li₂O₂ to LiOH in the DMSO-based electrolyte results from the chemical reactivity between DMSO and ORR products. Although both soluble superoxide species and Li₂O₂ have been proposed previously³⁷ to react with DMSO to form DMSO₂ and LiOH, no unique evidence is available to support the chemical reactivity of Li₂O₂ with DMSO as the process of discharging Li-O₂ cells in the previous work³⁷ can produce both soluble and solid-state superoxide species, as well as Li₂O₂.

5.3.2 Analyzing reactivity between $\text{Li}_2\text{O}_2/\text{KO}_2$ and DMSO using chemical mixtures

To assess the chemical reactivity of DMSO with Li_2O_2 , we examined commercial Li_2O_2 exposed to DMSO with and without superoxide anions in KO_2 present. Two suspensions that contained commercial, ball-milled Li_2O_2 (300 nm – 1 μm) and DMSO in a Li_2O_2 : DMSO molar ratio of 1:100 and DMSO with commercial Li_2O_2 and KO_2 in a molar ratio of Li_2O_2 : KO_2 :DMSO of 1:1:100 were prepared, where KO_2 was used as a source of O_2^- ions. After different amounts of time in the suspension, the liquid components of each suspension were analyzed by FT-IR spectroscopy and GC-MS to identify soluble decomposition products of DMSO while the solid components were collected after centrifugation of the suspensions, vacuum-dried and then studied using XRD and Raman spectroscopy.

The addition of KO_2 led to significant conversion of Li_2O_2 to LiOH , which is supported by the appearance of a peak at 3665 cm^{-1} (corresponding to the OH stretch of LiOH ¹⁹⁶) by Raman spectroscopy (Figure 5-4a). In contrast, while no LiOH was detected by XRD in the solid component from the suspension of Li_2O_2 and DMSO after 500 hours (Figure 5-1b), Raman spectroscopy, which has greater sensitivity to particle surfaces than XRD, revealed a minute amount of LiOH . It is important to note that commercial, ball-milled Li_2O_2 particles were only partially converted to LiOH in DMSO even with KO_2 present for 500 hours, in contrast to the complete conversion noted for electrochemically formed Li_2O_2 in the discharged electrodes in DMSO after 380 hours in the electrolyte (Figure 5-1a), indicating greater reactivity of $\text{Li}^+\text{-O}_2^-$ species and/or electrochemically formed Li_2O_2 than KO_2 toward DMSO. This claim is supported by a recent study in which the combination of a Li^+ salt together with KO_2 caused the generation of $\text{Li}^+\text{-O}_2^-$, which was found to promote greater degradation of a number of candidate electrolyte

solvents than KO_2 alone.⁹⁶ It has been argued in **Chapter 3** that the formation of $\text{Li}^+\text{-O}_2^-$ during discharge at high potentials in DMSO is accompanied by more electrolyte decomposition than Li_2O_2 alone. As commercial Li_2O_2 particles had comparable particle sizes (shown in Figure 5-3) to electrochemical Li_2O_2 (**Figure 5-2a**), higher reactivity of electrochemically formed Li_2O_2 can also be attributed to commercial, ball-milled Li_2O_2 particles having larger crystallite sizes³⁰ and lower surface concentrations of superoxide¹³³ than discharged Li_2O_2 toroidal particles, with plate-like crystallites¹²⁰ (having largely (001) terminations with LiO_2 surface chemistry^{71,132,138,139}).

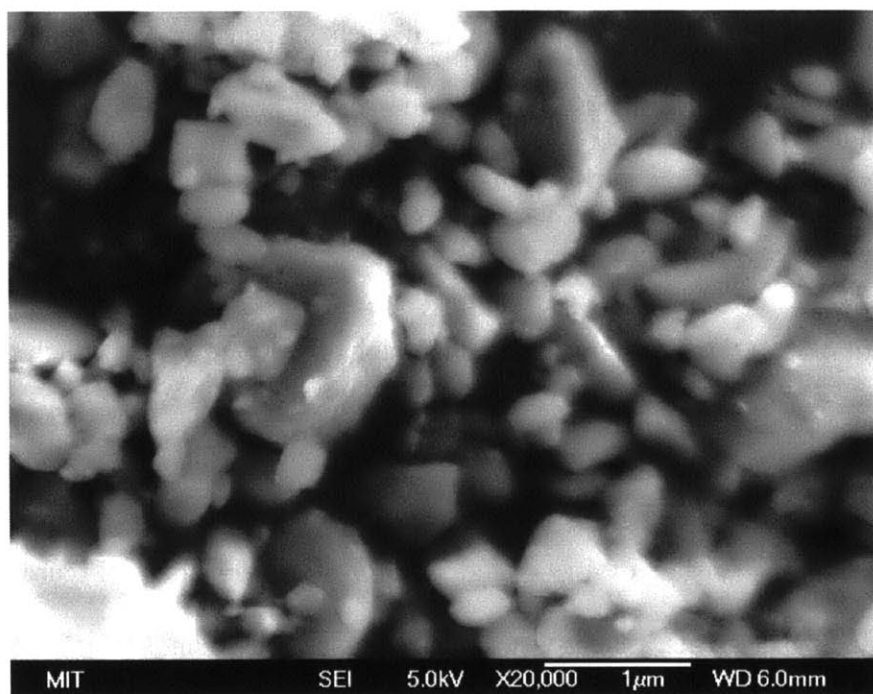


Figure 5-3. SEM images of ball-milled Li_2O_2 . Li_2O_2 particles have oval-shaped morphologies, and reach up to 1 μm in size.

A recent X-ray photoelectron spectroscopy (XPS) study detected Li_2CO_3 as a by-product of Li_2O_2 reactivity with DMSO, in addition to LiOH .¹⁹⁷ While significant quantities of Li_2CO_3

were not observed as a decomposition product in this study, it is possible to have Li_2CO_3 on the surface of LiOH particles, such that Li_2CO_3 is not detected by XRD, which is much less surface-sensitive than XPS. This hypothesis is supported by our previous work, where a surface layer of Li_2CO_3 was found to exist on commercial LiOH powder¹⁹⁸ and Figure 5-4a, in which a small peak around 1190 cm^{-1} in the Raman spectra of the $\text{KO}_2:\text{Li}_2\text{O}_2:\text{DMSO}$ mixture indicates the presence of some Li_2CO_3 .

FT-IR and mass spectrometry analysis shows that the generation of LiOH from Li_2O_2 detected by Raman was accompanied by an increase of DMSO_2 in the solution phase. FT-IR spectra of the suspension with KO_2 after 24 hours revealed the appearance of a new peak at 1142 cm^{-1} , which was absent in pristine DMSO , as shown in Figure 5-4b. This peak corresponds to the symmetric stretch of the SO_2 group in DMSO_2 , and this finding is in agreement with previous work by Mozhzhukhina *et al.*¹¹¹ In contrast, small intensities were found for the DMSO_2 peak from the suspension without KO_2 even after 336 hours of aging.

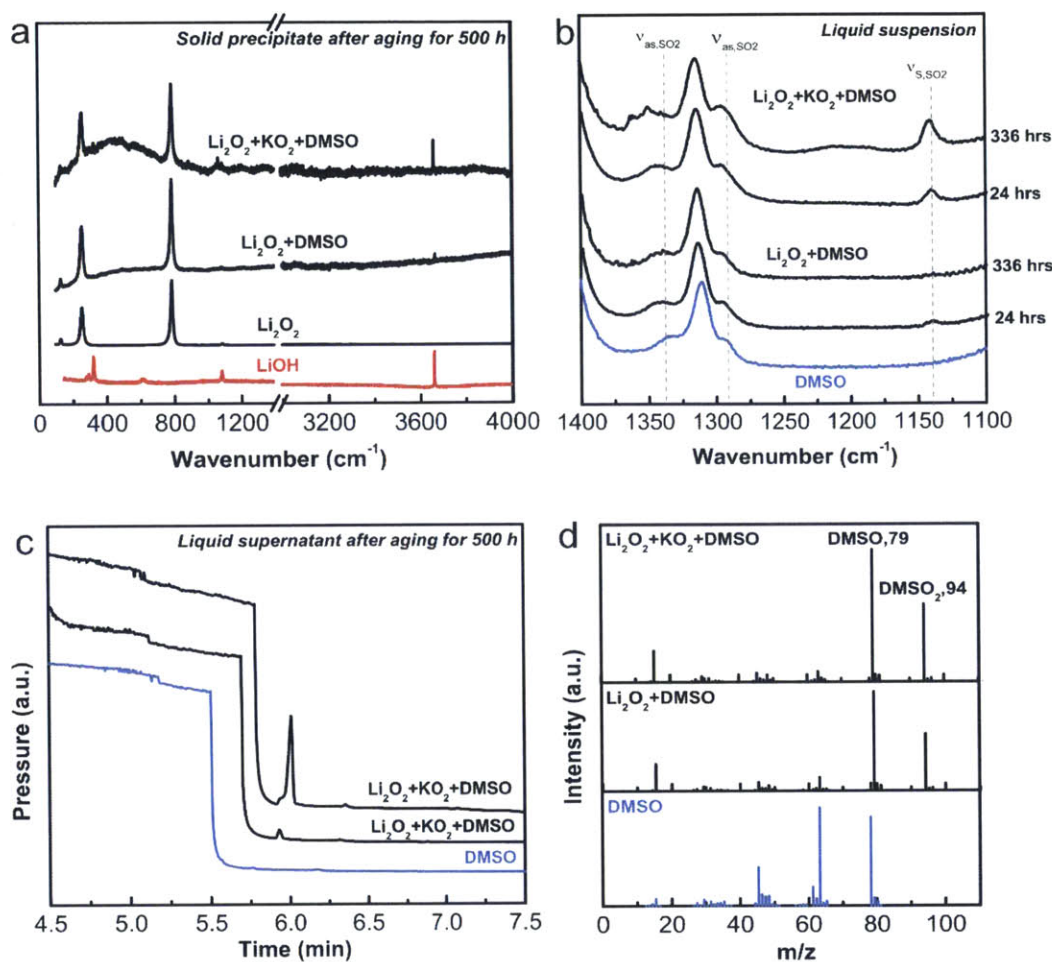


Figure 5-4 (a) Raman spectra of solid precipitates collected after centrifugation of suspensions of Li_2O_2 , KO_2 and DMSO and Li_2O_2 and DMSO in mole ratios of 1:1:100 and 1:100 respectively after 500 hours of continuous stirring. Spectra of commercial Li_2O_2 (ball-milled) and LiOH powders are shown for comparison. Spectra between 3000 and 4000 cm^{-1} have been background-corrected (see Figure S7). (b) FT-IR spectra of neat DMSO, and suspensions of Li_2O_2 , KO_2 and DMSO (with mole ratio of 1:1:100) and Li_2O_2 and DMSO (1:100) after 24 and 336 hours of mixing. The peak at 1142 cm^{-1} indicates the symmetric stretch of the SO_2 group in DMSO_2 (c) Gas chromatograms showing evolution of column pressure with time of analytes of neat DMSO and supernatants of suspensions of Li_2O_2 , KO_2 and DMSO and Li_2O_2 and DMSO in mole ratios of 1:1:100 and 1:100 respectively after 500 hours of continuous mixing and (d) mass spectra of neat

DMSO and after ~6 min of analyte evolution for supernatants of suspensions containing Li_2O_2 and DMSO and KO_2 , Li_2O_2 and DMSO.

The presence of DMSO_2 in the liquid component from the suspension with KO_2 was further confirmed using GC-MS, which has greater sensitivity than FT-IR and revealed the presence of DMSO_2 in the suspension without KO_2 after 500 hours of mixing (Figure 5-4c-d). Gas chromatograms of the supernatants of the suspensions with and without KO_2 displayed a broadened peak, which corresponds to an increase in column pressure, indicative of the production of DMSO. A secondary uptick in pressure at ~6 minutes was found for the liquid components from both suspensions with and without KO_2 (Figure 5-4c), where the peak intensity was much larger in the suspension with KO_2 than the one without. Mass spectra analysis of this peak (Figure 5-4d) reveals a parent species at an m/z value of 94, which corresponds to the molar mass of DMSO_2 at 94.13 g/mol, and a fragmentation pattern in good agreement with that reported previously for DMSO_2 .¹⁹⁹

The detection of DMSO_2 from the liquid component of the suspension without KO_2 , and accompanying conversion to LiOH , shows, for the first time, that DMSO is not stable against Li_2O_2 . This finding is further supported by the color change (from milky to yellowish, Figure D2 in Appendix D) and FT-IR detection of DMSO_2 in a suspension without KO_2 that was mixed with a much higher ratio of Li_2O_2 to DMSO (1:3 molar ratio vs. 1:100 used above) and after a longer time period (1440 hours), as shown in Figure D2b. This result contrasts with that reported by Mozhzhukhina *et al.*¹¹¹ who observed no DMSO decomposition when in contact with Li_2O_2 for a comparable 2 month (1440 hour) period, but do not report the Li_2O_2 : DMSO molar ratio used. FT-IR characterization of the higher Li_2O_2 : DMSO molar ratio suspension showing the presence of DMSO_2 thus highlights the importance of relative concentrations of electrolyte and active material

analogues in model chemical reactions to monitor electrolyte decomposition. The greater concentration of DMSO₂ in the liquid component from the suspension with KO₂ addition supports the high reactivity of O₂⁻ with DMSO reported previously^{111,166,195} and suggests greater reactivity of KO₂ than commercial Li₂O₂ particles with DMSO.

From XRD data showing complete conversion of Li₂O₂ in the discharged CNT cathodes to LiOH, it is clear that the electrochemical discharge product contains species that easily react with DMSO. Controlled studies using suspensions of Li₂O₂ and KO₂ in DMSO suggest that although limited DMSO decomposition occurs in the presence of Li₂O₂ alone, this process is greatly accelerated by the presence of superoxide species, and is strongly correlated with the evolution of LiOH. Although, as previously suggested by Mozhzhukhina *et al.*¹¹¹, nucleophilic attack of DMSO by superoxide can account for DMSO₂ evolution, it does not explain LiOH formation. Thus, we propose the following mechanism (Figure 5-5) as the dominant pathway for LiOH formation and DMSO decomposition: (i) the presence of superoxide promotes proton abstraction from DMSO, resulting in the formation of the dimsyl ion and a free proton (ii) a Li⁺ ion in Li₂O₂ couples strongly to the dimsyl ion and is replaced by the free proton, forming LiOOH which (iii) then attacks DMSO and forms LiOH and DMSO₂.

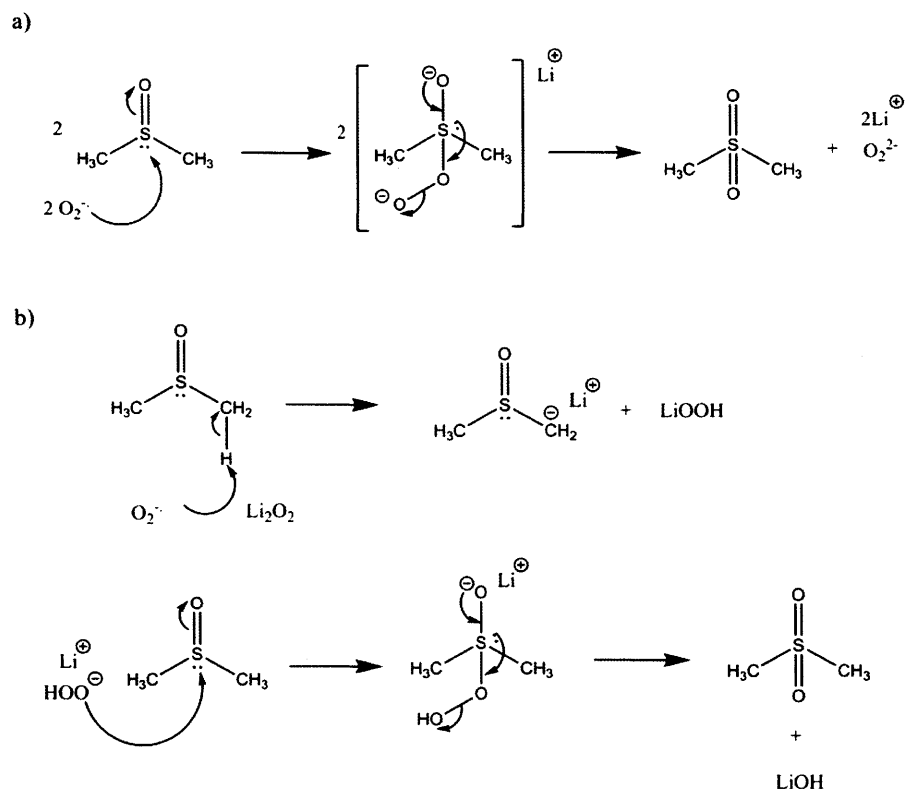


Figure 5-5. Schematic showing proposed mechanism for DMSO decomposition via either (a) nucleophilic attack by superoxide or (b) proton abstraction by superoxide ions followed by the formation of DMSO₂ and LiOH.

We note that LiOH can itself further decompose DMSO, resulting in the release of water, and the formation of lithium methylsulfonate and lithium sulfite species.³⁷ However, the analysis of solid-state decomposition products by XRD and Raman spectroscopy yielded LiOH only, and no secondary products related to LiOH decomposition. Further studies are required to assess the prominence of the reactivity between LiOH and DMSO.

This proposal is similar to that reported by Sharon *et al.*,³⁷ with the important difference that proton abstraction is facilitated by solid-state or near-surface superoxide-related species *after*

discharge, in addition to *residual* solution-based superoxide-like intermediates that were formed *during* discharge. This conclusion is obtained from the observation of Li_2O_2 immediately after the end of discharge - before a transformation to LiOH occurs - and is corroborated by the fact that the presence of KO_2 enhances decomposition of commercial Li_2O_2 to LiOH , while Li_2O_2 alone remains relatively stable against DMSO. While solution-based decomposition of DMSO by $\text{Li}^+\text{-O}_2^-$ is possible during discharge, it is important to note that $\text{Li}^+\text{-O}_2^-$ disproportionation (or electron transfer at higher overpotentials, see **Chapter 3**) to form solid Li_2O_2 is a competing process.⁶⁶ This possibility is borne out by a recent study by Zakharchenko *et al.*¹⁰⁴ where the evolution of Li_2O_2 was shown to follow upon the introduction of a Li salt to a suspension of KO_2 in DMSO. Decomposition of DMSO is therefore more likely to proceed by virtue of the presence of superoxide-like species on the surface of solid Li_2O_2 , the possibility of which has been discussed in **Chapter 3** and proposed by recent DFT¹³², Raman¹³⁸, magnetic¹³⁹ and X-ray absorption⁷¹ studies, in addition to residual $\text{Li}^+\text{-O}_2^-$ species in solution from the ORR. It is important to note that solid-state and soluble forms of superoxide might have different reactivities towards DMSO, which the present study does not distinguish, and further studies will be required to elucidate. We note, however, that recent DFT computations of the energetics of DME- Li_2O_2 cluster interactions suggest that the presence of unpaired spins in Li_2O_2 can lead to hydrogen abstraction from and decomposition of the solvent¹⁶¹ – and that a related interaction may exist between superoxide species and DMSO, whose protons become acidic in the presence of strong bases²⁰⁰ such as superoxide. Thus, although the very limited evolution of DMSO_2 from DMSO in the presence of ball-milled Li_2O_2 may be caused by Li_2O_2 directly,¹⁵⁹ it may also be caused by superoxide-like moieties which have been proposed to exist on the surface of ball-milled Li_2O_2 particles,¹³³ rather than Li_2O_2 itself.

An important implication of the time dependence of the chemical instability of DMSO in the presence of superoxide and/or Li_2O_2 is that short discharge times in lab-scale Li- O_2 batteries using DMSO-based electrolytes will likely result in insignificant DMSO and Li_2O_2 decomposition and thus, long cycle life. This is likely the case in previous studies reporting highly reversible Li_2O_2 formation for ~ 100 cycles using nanoporous Au¹⁵ and TiC⁵⁶ cathodes in DMSO-based electrolytes. Based on electrode masses, gravimetric capacities and current densities provided in refs. 15 and 17, we calculate discharge times of 40 min and 1 h 24 min per cycle for nanoporous Au and TiC cathode, respectively. According to the results presented herein, such short exposure times between Li_2O_2 and/or other discharge intermediates and DMSO are unlikely to result in any significant DMSO decomposition.

5.4 Conclusions

In summary, this chapter presents the time-dependent changes in the discharge product chemistry and morphology of a discharged carbon-based Li- O_2 positive electrode in a DMSO-based electrolyte. We show, for the first time, that Li_2O_2 is the only species detected by XRD immediately after discharge, but gradually decomposes completely into LiOH upon prolonged exposure to the electrolyte. Such time-dependent changes after discharge are not typically monitored in Li-air battery research, which can explain previous studies reporting different amounts of Li_2O_2 and LiOH after discharge.^{37,98,151,152} We further show that commercial Li_2O_2 powder can decompose DMSO to DMSO_2 and that the presence of KO_2 accelerates DMSO decomposition *and* the conversion from Li_2O_2 powder into LiOH. These experiments allow us to unambiguously probe the chemical reactivity of DMSO with ORR products, without the influence of carbon electrodes and other species formed during discharge of Li- O_2 cells. While both

superoxide-like species^{37,111,194,195} and Li_2O_2 ^{37,159} have been proposed to react and decompose DMSO to DMSO_2 and form LiOH , this work is the first to provide unique evidence for the chemical reactivity between DMSO and Li_2O_2 . Findings from this chapter suggest that DMSO might not be suitable for the oxygen electrode in the development of rechargeable Li-air batteries with long cycle life.

Chapter 6: Summary and Perspectives

This thesis explored the relationship between the energetics of O_2 redox processes, and nucleation, growth, and reactivity of Li-O products in Li- O_2 batteries. Keen attention was paid to the use of model systems (RDE, RRDE, model chemical mixtures) and first principles calculations to shed light on the influence of reaction intermediates on the growth of toroidal vs particulate Li_2O_2 morphologies and changes in discharge product chemistry. **Chapter 2** studied the influence of O_2^- and Li^+ ion solvation on the energetics of O_2/O_2^- and Li^+/Li redox processes using a combination of rotating disk techniques and first principles solvation energy calculations. The redox potential of the transient $Li^+-O_2^-$ intermediate was estimated for the first time using the RRDE, and we showed that both the coupling strength and solubility of $Li^+-O_2^-$ were rationalized using the combined solvation of Li^+ and O_2^- ions, with greater combined solvation increasing solubility but decreasing coupling energy, respectively.

Building on these insights, **Chapter 3** focused on understanding nucleation and growth of Li_2O_2 in Li- O_2 batteries, using high surface area, multi-walled CNT and VC electrodes as model systems. We reported the formation of large ~300 nm donut-shaped particles of Li_2O_2 at high applied potentials during Li- O_2 discharge, and smaller particles (< 50 nm) at lower potentials, showing that the applied discharge potential can have an impact on mechanisms for Li_2O_2 growth. Using RRDE and EQCM, it was shown that surface-mediated reaction pathways were dominant at low potentials, while the solution-mediated disproportionation pathway was more operative at high potential. Within this framework, solvent was found to play a major role in dictating the point of transition between the two reaction mechanism regimes: as $Li^+-O_2^-$ solvation decreased (from

DMSO to DME), the switch from solution-mediated disproportionation to surface-mediated mechanism occurred at higher applied potentials.

Despite correlations between $\text{Li}^+\text{-O}_2^-$ solvation and discharge potential and capacity, it was shown that $\text{Li}^+\text{-O}_2^-$ solvation does not scale with Li_2O_2 particle size, particularly at low applied potentials. A growth model incorporating the effect of Li_2O_2 supersaturation and Li_2O_2 -electrolyte reactivity on toroid size was therefore introduced. While qualitative agreements with experiments were found, further studies are needed to establish a more predictive quantitative relationship between Li_2O_2 size and solvent properties.

Chapter 4 highlighted the importance of electrolyte deprotonation more generally to decomposition reactions during Li- O_2 discharge by showing that the effective pKa of water in non-aqueous solvents influences discharge product chemistry: low pKa is indicative of a lower barrier to deprotonation by ROS, leading to LiOH formation during discharge, while high pKa is likelier to result in Li_2O_2 . **Chapter 5** investigated the long-term stability of discharge product chemistry upon aging with the electrolyte, using DMSO as a model case. We showed that aging electrochemically formed Li_2O_2 in DMSO induced a change to LiOH over time, and supported this conclusion using detailed structural and spectroscopic analysis of suspensions of Li_2O_2 and KO_2 in DMSO, which successfully mimicked the evolution observed under electrochemical conditions. We showed, moreover, that superoxide ions accelerate the deprotonation and subsequent decomposition of DMSO. The relevance of aging to discharge product decomposition has been recently demonstrated in Na- O_2 batteries, where it was shown that longer aging of NaO_2 with a glyme-based electrolyte promotes its decomposition to $\text{Na}_2\text{O}_2 \cdot 2\text{H}_2\text{O}$.²⁰¹

This thesis raises several important questions that future studies are well-positioned to address. Firstly, there is a need for more accurate first principles calculations of O_2^- solvation that would more closely reflect changes in O_2/O_2^- potential measured experimentally. Several strategies are possible in this regard, such as modeling $TBA^+-O_2^-$ rather than naked O_2^- ions in solution, and more explicit modeling of the ion-solvent relationship, such as with molecular dynamics simulations, from which solvation free energies can be computed.

Following on from this, one exciting possible avenue of research has to do with investigating the influence of O_2^- and Li^+ solvation on ORR and OER kinetics. Indeed, understanding and controlling the kinetics of electron transfer during energy conversion reactions is in a general sense critical for promoting efficient energy storage and conversion. The operation of most advanced energy conversion systems involves multiple electron-transfer steps, with many reaction intermediates. Thus, catalyzing these reactions relies on a precise understanding *both* of intermediate energetics and the position of the transition state in the reaction's free energy landscape.

Marcus theory and related semi-classical theories of electron transfer by Levich and Dogonadze are ideally suited to serve as a starting tool for such investigations.^{202,203} In outer sphere reactions, reaction rates are dictated by solvent reorganization around donor/acceptor (closely related to solvation energies computed in **Chapter 2**), density of states of the electrode, and both electrostatic and quantum-mechanical interactions between electrode and redox-active species. Thus, the possibility exists for rational design of electrode-electrolyte systems optimized for fast kinetics. Combining experimental measurements of ORR/OER kinetic currents with DFT or molecular dynamics simulations will prove fruitful, and likely indispensable, for a comprehensive understanding of design principles. Theoretical studies have already suggested that

important deviations from Marcus theory are expected for electrochemical reactions involving neutral species, such as changes in solvent reorganization energy as a result of solute charge, electrostriction, dielectric saturation and non-uniform potentials at the double layer.²⁰⁴⁻²⁰⁶ Other questions surrounding the degree of outer sphere character of the O₂ ORR²⁰⁷ and also its non-adiabaticity are crucial to investigate.²⁰⁸

Questions about electrochemically induced phase transformations raised in **Chapter 3** also need further exploration. This problem has wide appeal, as phase transformations occur in several energy storage systems which have been identified as promising ingredients in the mix of energy options needed for a more carbon-free economy. While the formation of electrochemically-induced solid phases during battery reactions has been studied in several lithium-ion cathodes such as LiCoO₂ and LiFePO₄,^{209,210} similarly detailed understanding in Li-O₂ batteries has proven elusive. The difficulty of studying such reactions is compounded by the possibility that non-traditional nucleation and growth pathways based on mesocrystallization i.e. meso-scale assembly of amorphous/nanocrystalline growth precursors, might be operative. Thus, in the case of Li₂O₂ formation, much remains unclear about how the observed morphologies are controlled by fundamental parameters that can more fully describe their growth, including electrode surface chemistry, reactant supersaturation and thermodynamic/kinetic nucleation barriers. The classical growth model discussed in **Chapter 3** and potentiostatic experiments performed in **Chapter 4** comprise an attempt to lay the groundwork for such studies.

In the future, a more precise understanding of the morphological evolution of Li₂O₂ in response to measurable, local parameters is needed to optimize specific and volumetric energy densities in these systems. It would be interesting to study the electrodeposition of Li₂O₂ by bridging the gap between well-developed models of electrodeposition (such as for metals) and

insights from the study of bio-mineralization where, for instance, morphologies of CaCO_3 and BaSO_4 precipitated under certain conditions bear striking resemblance to that of electrochemically formed NaO_2 and Li_2O_2 in Na- and Li- O_2 batteries respectively.^{62,120,154} Novel application of experimental techniques such as extended x-ray absorption fine structure, electron microscopy, and optical scattering techniques has the potential to elucidate fundamental mechanisms behind the nucleation and growth of insulating phases relevant to battery operation. Model systems will be useful to study, as well. During Li_2O_2 , the overall reaction rate can be monitored by the rate of O_2 gas consumption and release, while the precipitation of the solid phase is typically accompanied by solution-phase changes in ion concentration, which can be monitored with a judicious choice of reference electrode. By combining such electrochemical measurements with a direct probe of the evolving structure, a fuller picture of how Li_2O_2 forms will emerge.

In summary, elucidating fundamental electrochemical mechanisms of Li- O_2 battery operation, with a particular focus on understanding interfacial electron transfer and electrochemically driven phase transformations, has the potential to shed light on fundamental mechanistic principles driving metal-air battery electrochemistry and enable rational design of future energy storage and conversion systems tailored for high performance at low cost.

Appendix A

Nernstian corrections to Li⁺/Li and O₂/TBA⁺-O₂⁻ redox potentials

Experimentally measured Li⁺/Li redox potentials (otherwise known as formal potentials) were corrected to the standard scale using the Nernst equation²¹¹: $E_{Li^+/Li} = E_{Li^+/Li}^o + \frac{RT}{F} \ln[Li^+]$, where $E_{Li^+/Li}$ is the experimentally measured equilibrium potential, $E_{Li^+/Li}^o$ is the standard potential, F is Faraday's constant (96,485 C/mol) and Li metal is assumed to have an activity of 1. Since all Li⁺/Li potentials were measured in electrolytes containing 0.1 M Li⁺ rather than the standard concentration of 1 M Li⁺, the standard potential was obtained by subtracting the $\frac{RT}{F} \ln[Li^+]$ factor of 59 mV from all measured formal Li⁺/Li potentials. O₂/TBA⁺-O₂⁻ and O₂/Li⁺-O₂⁻ potentials were similarly corrected based on varying O₂ solubilities in the different electrolyte solvents used, since the definition of standard state implies an equality of concentrations of electroactive species in solution.⁸³ A correction term equal to $\frac{RT}{F} \ln \left[\frac{1}{k_H^{cp}} \right]$ was subtracted from all formal O₂/TBA⁺-O₂⁻ potentials, where k_H^{cp} is the Henry's law constant in M/bar, computed based on the O₂ solubility in the solvent under consideration. O₂ solubilities and the resulting corrections were obtained from literature for DMSO, DME, MeCN and DMF (Table A 1).^{76,212} The value for DMA was assumed to be the same as DMSO, due to their structural similarity.

Table A 1. Literature values of oxygen solubility in various organic solvents in mM, and corresponding standard potential corrections in mV.

Electrolyte solvent	[O ₂] _{lit} (mM)	Correction
		(RT/F)ln(1/k _H ^{cp}) (mV)
MeCN	8.1 ⁷⁶	124
DMSO	2.1 ⁷⁶	158
DMA	2.1	158
DME	8.8 ²¹²	120
DMF	4.8 ⁷⁶	137

Table A 2. Solvation free energies of the Li⁺ ion in organic solvents (kJ/mol) calculated using the thermodynamic cycle shown in Figure 3a (n = 2 - 4) and the pure dielectric continuum model (n = 0). ^aUsing the default Li van der Waals radii in Jaguar (r_{Li} = 1.226 Å). ^bDME is coordinated to Li⁺ as a bidentate ligand.

solvent	$\Delta G^*_{\text{solv}}(\text{Li}^+)$					DN
	n = 0 ^a	n = 2	n = 3	n = 4	expt	
DMSO	-562			-557	-566	29.8
DME	-494	-481 ^b	-537 ^d			24.0
MeCN	-558			-509	-514 ⁹⁰	14.1
DMA	-559			-550		27.8

Table A 3. Solvation free energies of the superoxide ion in organic solvents (kJ/mol) calculated using the thermodynamic cycle shown in Figure 2-6a (n = 4–8) and the pure dielectric continuum model (n = 0). ^aUsing the default Li van der Waals radii in Jaguar (r_O = 1.600 Å). ^bThe calculated pK_a values of the C–H acids in DMSO.²¹³

solvent	$\Delta G^*_{\text{solv}}(\text{O}_2^-)$					AN	pK _a ^b
	n = 0 ^a	n = 4	n = 6	n = 8	expt		
DMSO	-341	-298	-315		~280	19.3	35.0
DME	-300	-230	-259			10.2	51.8
MeCN	-340	-296	-308	-316	~279	18.9	30.3
DMA	-340	-279	-305			13.6	34.4

Table A 4. Comparison of the calculated reduction potentials for the O_2/O_2^- couple in aprotic solvents (V) using pure dielectric continuum ($n = 0$) and most stable clusters found for O_2^- and Li^+ in the cluster/continuum solvation model. ^aObtained from the thermodynamic cycle shown in Figure 2-6a using calculated ionization free energies, the experimental sublimation free energy of Li metal, and the solvation energies. ^bThe absolute potential is defined relative to an electron at rest in vacuum under the condition that the surface potential of solution is equal to zero.

solvent	dielectric continuum model		cluster/continuum model	
	vs Li^+/Li^a	absolute ^b	vs Li^+/Li^a	absolute ^b
DMSO	2.97	3.85	2.59	3.60
DME	1.84	3.43	1.80	3.03
MeCN	2.91	3.83	2.10	3.61
DMA	2.92	3.84	2.42	3.50

Table A 5. Comparison of standard experimental $O_2/TBA^+-O_2^-$ and calculated O_2/O_2^- vs Li^+/Li potentials against Gutmann DN and ANs. Calculated potentials were obtained using thermodynamic cycle shown in Figure 2-6a using the calculated ionization free energies given in the experimental²¹⁴ sublimation free energy of the Li metal (30.26 kcal/mol), and the solvation free energies listed in Table A 2 and Table A 3.

solvent	AN	DN	Expt	Calculated
DMSO	19.3	29.8	2.35	2.59
DME	10.2	24.0	1.79	1.80
MeCN	18.9	14.1	1.79	2.10
DMA	13.6	27.8	2.14	2.42
DMF	16.0	26.6	2.23	

Table A 6. Computed solvation free energies for $Li^+-O_2^-$, computed Gibbs free energies for $Li^+ + O_2^- \rightarrow Li^+-O_2^-$, and computed potentials for reduction of oxygen to superoxide in the absence and presence of an Li^+ salt in aprotic solvents. ^aEnergies are in kJ/mol, reduction potentials are in V (vs Li^+/Li).

solvent	$\Delta G_{solv}^*(Li^+-O_2^-)$	ΔG_r^* $Li^+ + O_2^- \rightarrow Li^+-O_2^-$	E_1^* for O_2/O_2^-	E_1^* for $O_2/(O_2^-$ or $Li^+-O_2^-)$
DMSO	-159	5.82	2.59	2.59
DME	-134	-51.9	1.80	2.27
MeCN	-139	-21.1	2.10	2.27
DMA	-149	-0.80	2.42	2.42

Table A 7. Estimated Gibbs free energies for $\text{Li}^+ \text{-O}_2^-$ coupling ($\text{Li}^+ + \text{TBA}^+ \text{-O}_2^- \rightarrow \text{Li}^+ \text{-O}_2^- + \text{TBA}^+$) in different solvents, which were obtained from the difference between standard $\text{O}_2/\text{Li}^+ \text{-O}_2^-$ (E_1^* for $\text{O}_2/\text{Li}^+ \text{-O}_2^-$) potentials measured using RRDE and $\text{O}_2/\text{TBA}^+ \text{-O}_2^-$ potentials (E_1^* for $\text{O}_2/\text{TBA}^+ \text{-O}_2^-$).^a Coupling energy was estimated by assuming 96.2 kJ/mol (23 kcal/mol) per V. ^aEnergies are in kJ/mol with kcal/mol equivalent in brackets, reduction potentials are in V (vs Li^+/Li).

solvent	ΔG_r^*	E_1^*	E_1^*
	$\text{Li}^+ + \text{TBA}^+ \text{-O}_2^- \rightarrow \text{Li}^+ \text{-O}_2^- + \text{TBA}^+$	for $\text{O}_2/\text{TBA}^+ \text{-O}_2^-$	for $\text{O}_2/\text{Li}^+ \text{-O}_2^-$
DMSO	-21(-5.0)	2.35	2.57
DME	-120(-28.7)	1.79	3.03
DMA	-47(-11.2)	2.14	2.63

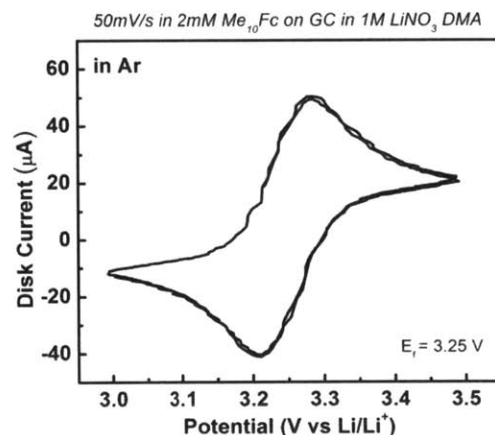


Figure A 1. Steady-state CVs at 50 mV/s showing the $\text{Me}_{10}\text{Fc}^+/\text{Me}_{10}\text{Fc}$ redox process at a formal potential of 3.25 V vs Li^+/Li in argon-saturated DMA containing 2 mM Me_{10}Fc and 1 M LiNO_3 . CVs were obtained with a Li metal reference electrode.

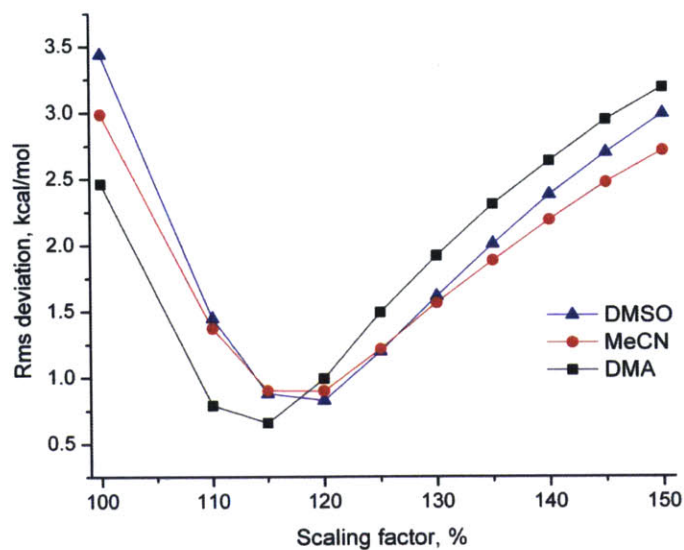


Figure A2. The accuracy of solvation calculations for neutral organic molecules in aprotic solvents as a function of a scaling factor for solute van der Waals radii.

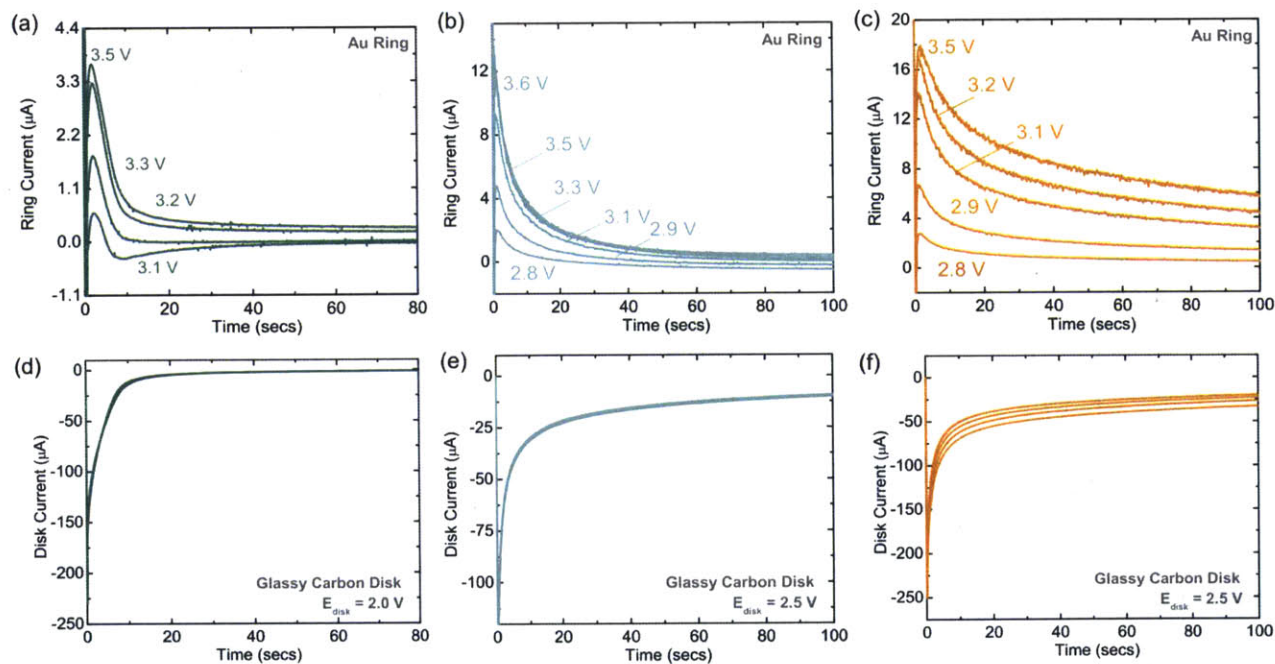


Figure A3. Ring current transients during RRDE measurements in 0.1 M LiClO₄ in (a) DME (b) DMA and (c) DMF at 900 rpm and disk current transients during similar measurements in (d) DME (e) DMA and (f) DMF at 900 rpm with disk held at 2.0, 2.5 and 2.5 V vs Li⁺/Li respectively.

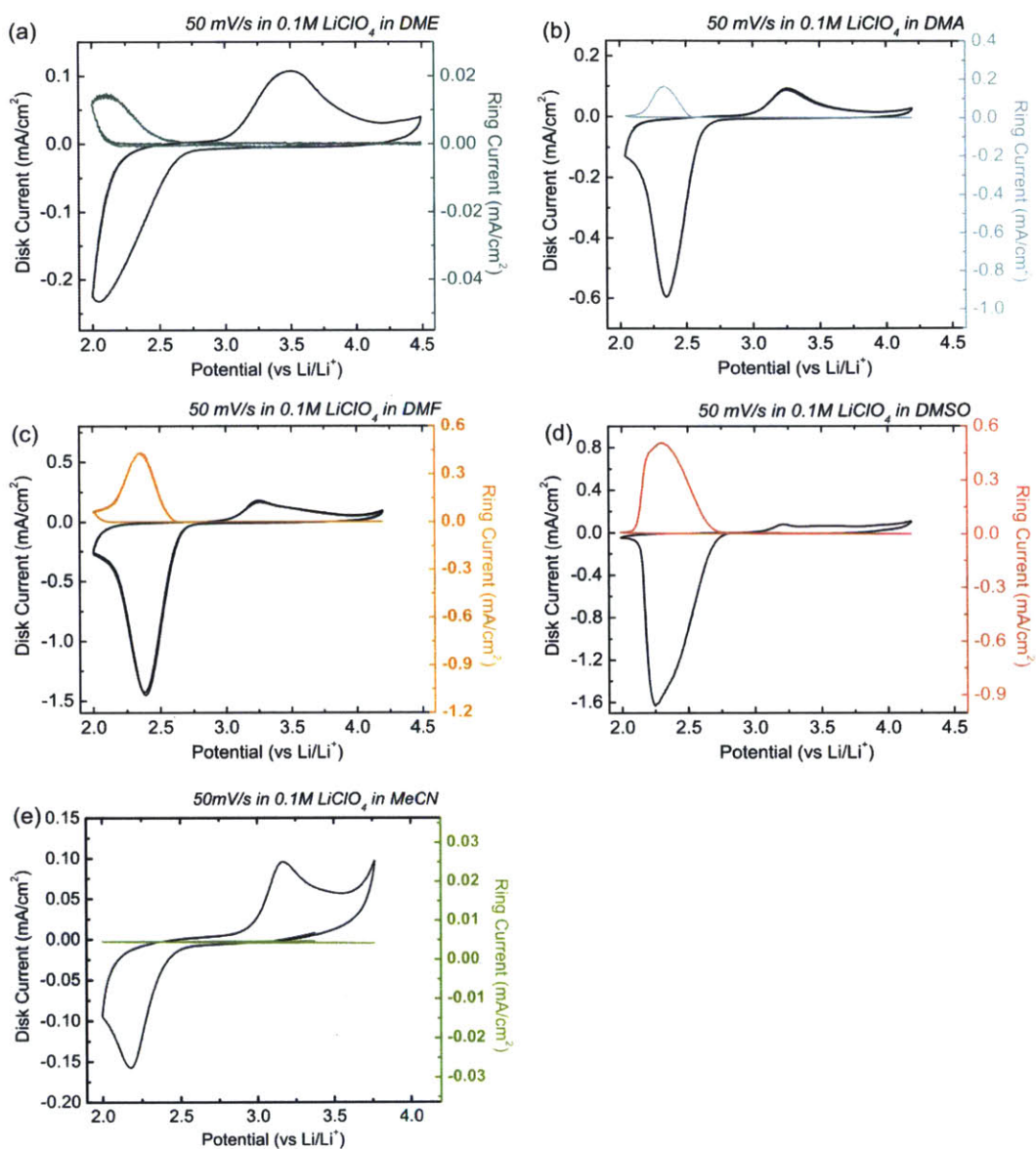


Figure A4. CVs obtained with RRDE at 50 mV/s at 900rpm in oxygen-saturated electrolytes containing 0.1M LiClO₄ in (a) DME (b) DMA (c) DMF (d) DMSO and (e) MeCN with ring polarized at 3.5 V vs Li⁺/Li. Black and colored curves denote disk and ring current responses respectively.

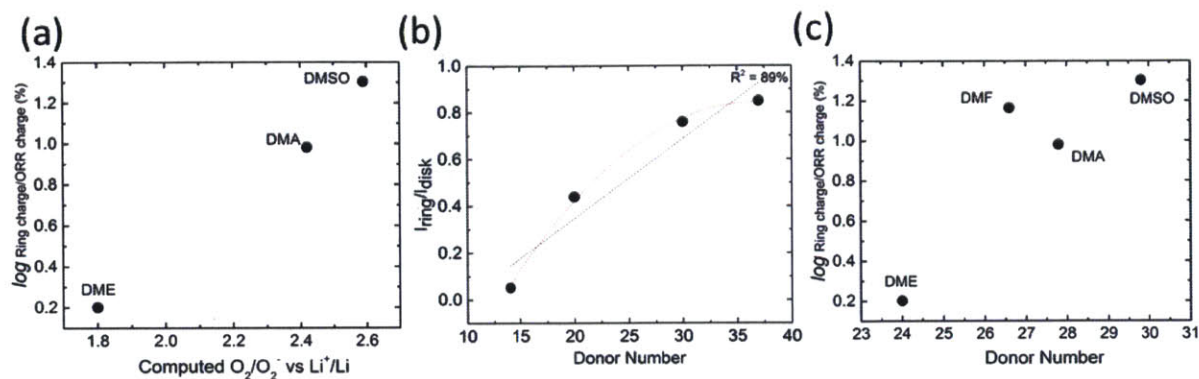


Figure A5. Comparison between (a) logarithm of ring-to-disk charge ratios obtained by integrating ring and disk current transients during Li-ORR and computed O_2/O_2^- vs Li^+/Li potentials (b) solvent DN and peak ring-to-disk currents during CV scans reported in Johnson *et al.*⁶⁷ There is a linear trend (black dash) with an R^2 value of 89% and a polynomial fit (red dash) of 99% (c) Comparison between logarithm of ring-to-disk charge ratios obtained by integrating ring and disk current transients during Li-ORR and solvent DN for DMSO, DME, DMA and DMF.

Appendix B

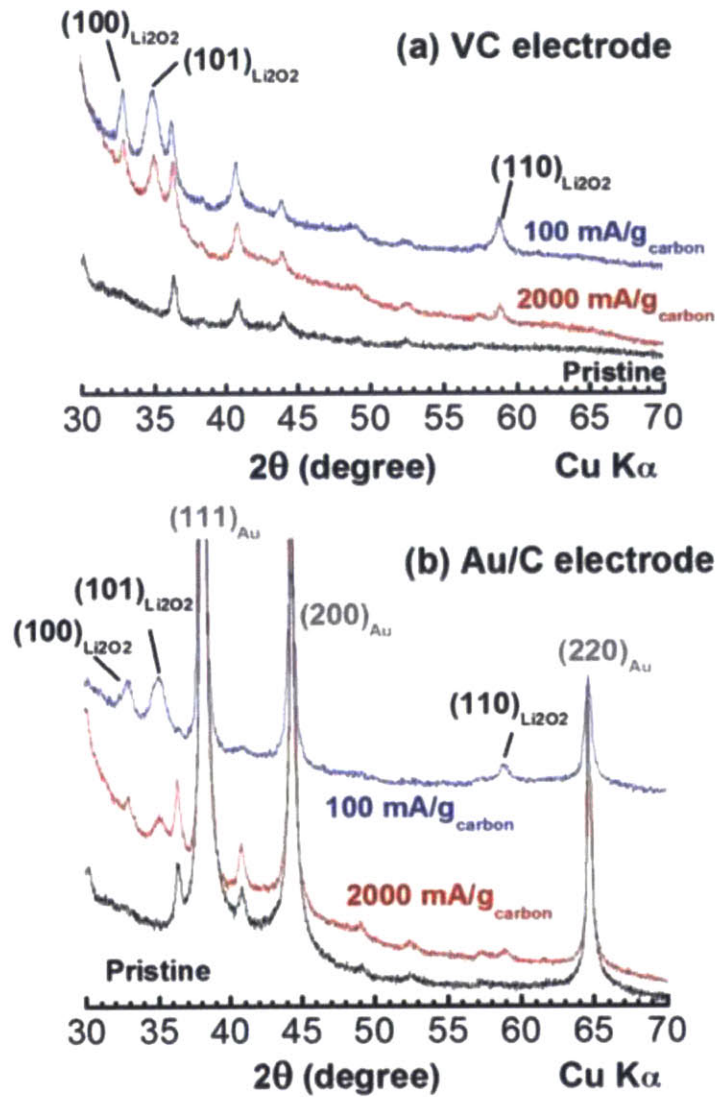


Figure B 1. XRD patterns of pristine and discharged electrodes supported on a Celgard C480 (100 and 200 mA/g_C) for (a) VC and (b) Au/C. Reflections appearing in pristine VC electrode came from the Celgard C480 separator, while those from the pristine Au/C electrode came from both Au nanoparticles and the separator.

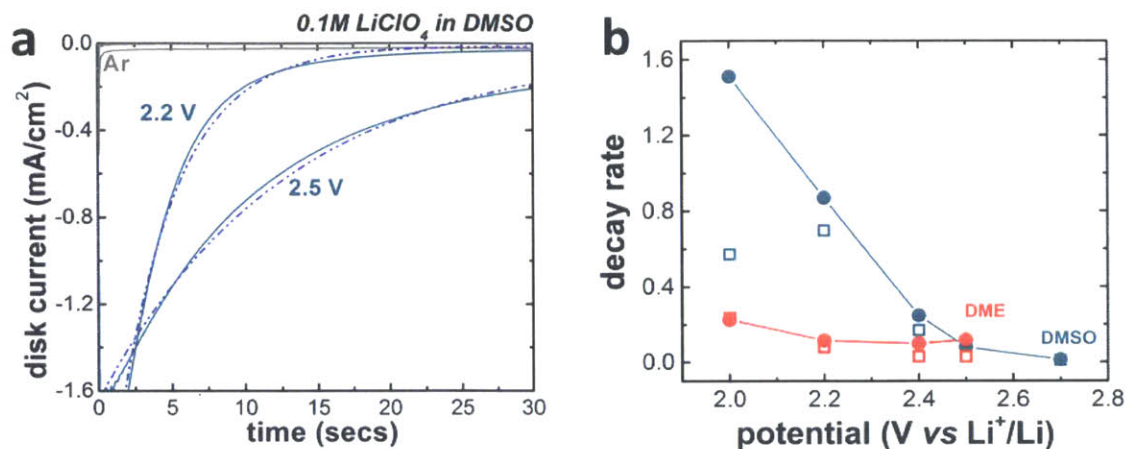


Figure B 2. (a) Examples of exponential fitting with disk current transients at 2.2 and 2.5 V vs Li⁺/Li in DMSO. Transient were fit to a formula $y = y_0 + Ae^{R_0x}$, where R_0 is taken as the decay rate. (b) Absolute decay rates for disk (filled circle) and ring (open squares) current transients vs disk potential in 0.1M LiClO₄ in DMSO and DME.

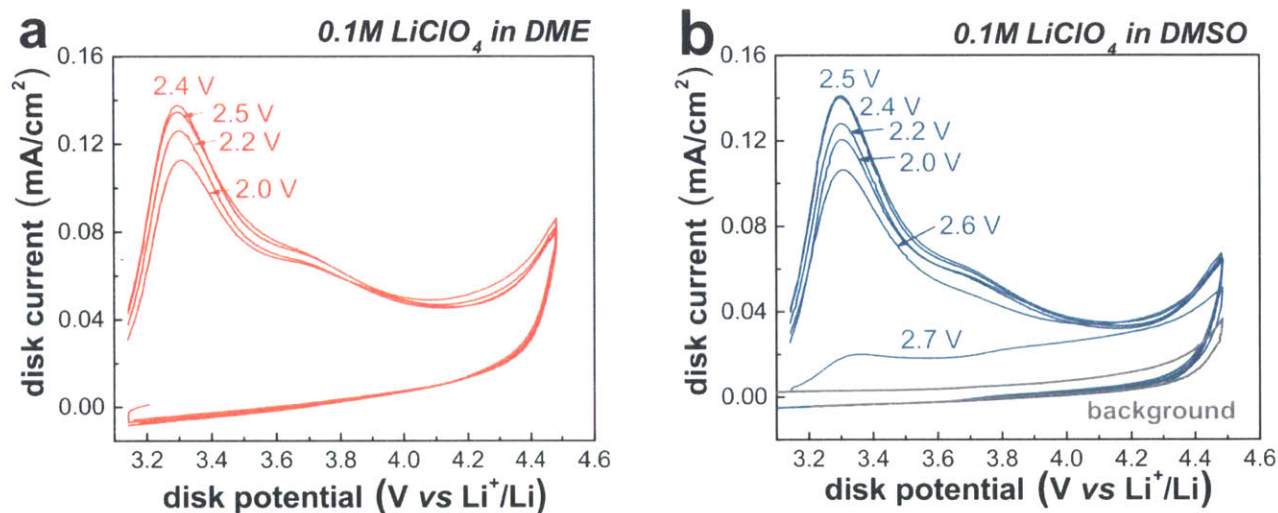


Figure B 3. Linear sweep measurements at 50 mV/s following potentiostatic ORR at selected potentials between 2.0 and 2.7 V on glassy carbon in O₂-saturated 0.1M LiClO₄ in (a) DME and (b) DMSO to oxidize electrodeposited species. The grey profile in (b) is the background scan under O₂.

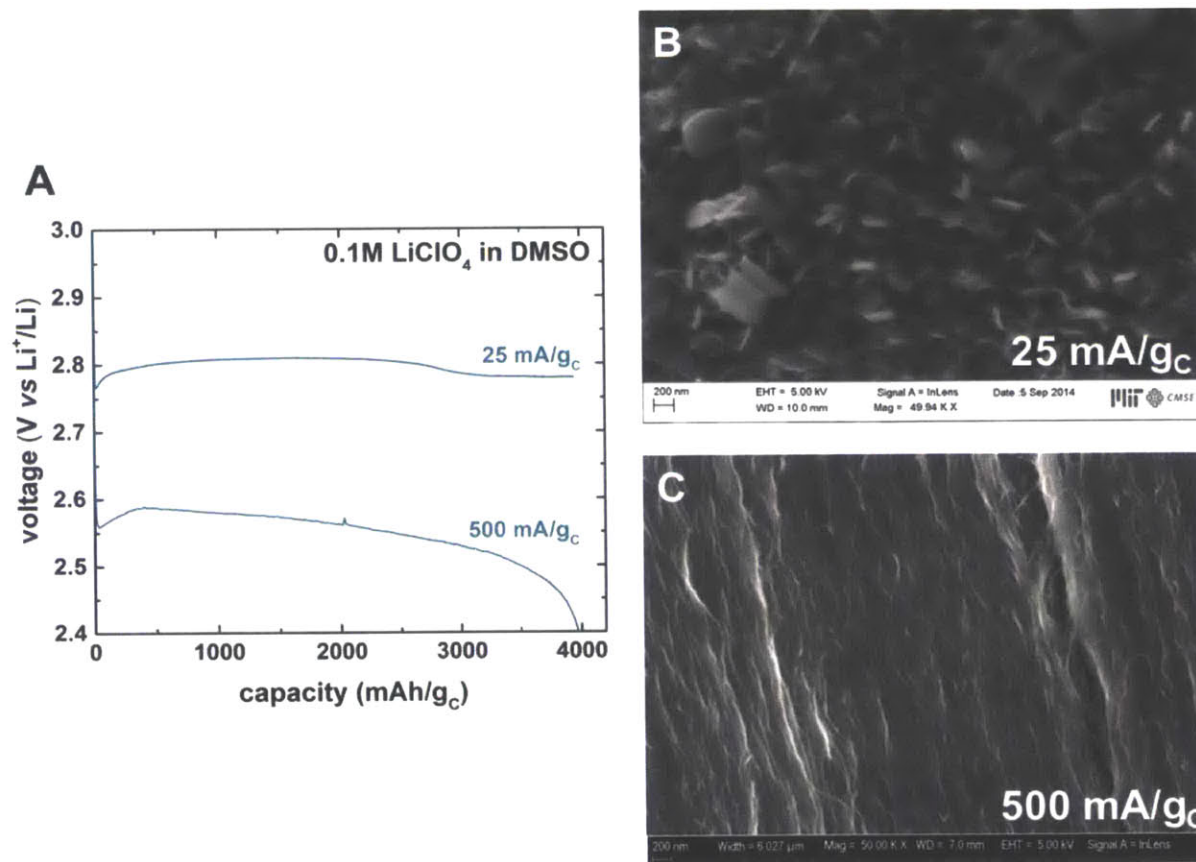


Figure B 4. (a) Galvanostatic discharge curves and (b,c) *ex situ* scanning electron microscopy (SEM) images of CNT electrodes discharged at 25 and 500 mA/g_c to ~4000 mAh/g_c, respectively. The results show toroidal discharge product morphologies at 25 mA/g_c, where the discharge potential remained above 2.75 V vs Li⁺/Li whereas at 500 mA/g_c (discharge < 2.6 V), the CNT sidewalls are conformally coated.

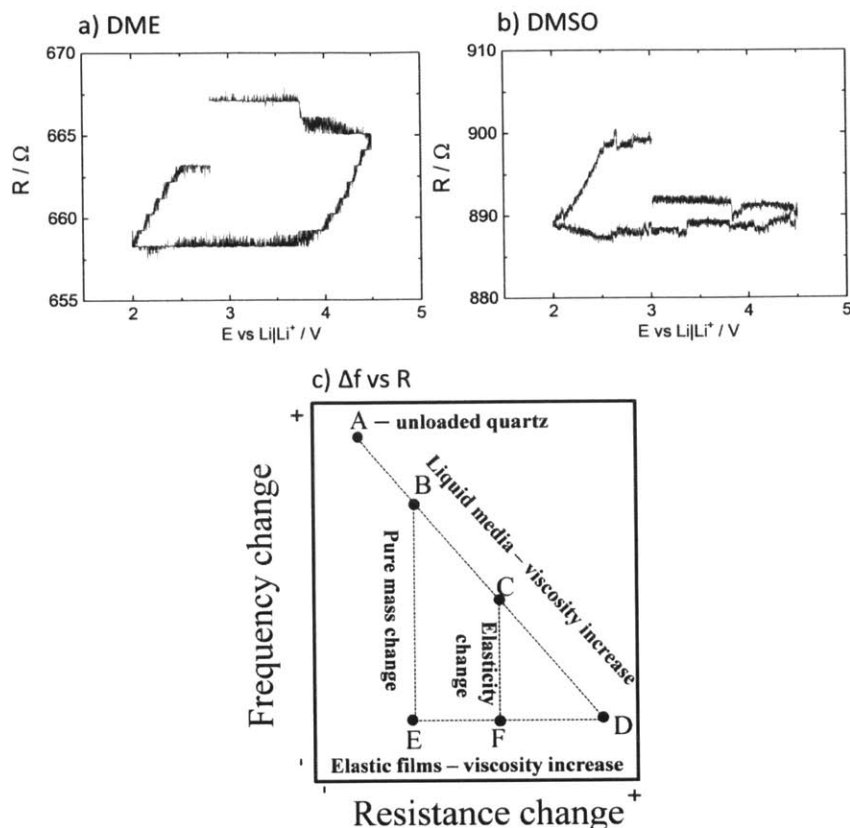


Figure B 5. Motional resistance changes for the CV EQCM experiments in (a) DME and (b) DMSO. (c) Schematic graph showing the possible reasons for frequency and resistance changes.²¹⁵ The addition of any elastic thin film over a perfectly smooth crystal should theoretically result in either no change in resistance or a small increase (when the deposit is rough or viscous). This was not the case in our experiments, where a small decrease in R is observed when deposition of mass starts. Since, however, we used graphite-coated quartz with exceptionally high roughness ($0.6 \mu\text{m}$, according to Bio-Logic), the electrolyte is likely trapped within pores on the electrode surface, which causes additional vibrational energy dissipation, resulting in high starting motional resistances (DME – 660Ω and DMSO – 900Ω).²¹⁶ Deposition of mass within the pores will then result in pore clogging and consequently, a decrease in motional resistance. Nevertheless, the resistance change is very small (6Ω in DME and 10Ω in DMSO) thus its effect on the frequency

change is minor, and we can ascribe frequency changes during O₂ reduction mostly to mass changes.

Discussion of Figure 3-6

Following Albery *et al.*,⁸¹ the expected collection efficiency of an RRDE, N detecting a reactive species with rate constant k is:

$$N = N_g - \beta^{\frac{2}{3}} \left(1 - \frac{U}{A_1} \right) + \frac{1}{2A_1} A_2^2 \kappa^2 U \beta^{\frac{4}{3}} - 2A_2 \kappa^2 T_2$$

where N_g is the geometrical collection efficiency of 0.235, $\beta = 3 \ln \frac{r_3}{r_2}$, $T_2 = 0.718 \ln \frac{r_2}{r_1}$, (with r_1 , r_2 and r_3 representing the disk radius, and internal and external ring radii respectively), $\kappa = k^{1/2} \omega^{-1/2} D^{-1/6} \nu^{1/6} 0.51^{-1/3}$, $A_2 = 0.643 \nu^{1/6} D^{1/3}$, and $U = \frac{1}{\kappa} \tanh(A_1 \kappa)$. ω , D and ν are the rotation rate (in s⁻¹) superoxide diffusion coefficient in and kinematic viscosity of the solvent. Kinematic viscosities of DME and DMSO are 5.4×10^{-7} m²/s and 1.8×10^{-6} m²/s respectively, however Li⁺-O₂⁻ diffusion coefficients are not available from literature. We therefore assume, following O₂⁻ diffusion coefficient measurements by Herranz *et al.*⁸² that Li⁺-O₂⁻ diffusivity is roughly 10× less than its O₂ diffusion counterpart. Thus, using an O₂ diffusion coefficient of 4×10^{-5} cm²/s²⁴ in 0.1M Li⁺ in DME results in an Li⁺-O₂⁻ diffusivity of 4×10^{-10} m²/s. We obtain the corresponding Li⁺-O₂⁻ diffusivity in DMSO by taking advantage of the Stokes-Einstein relation which dictates an inverse relationship between species diffusivity and dynamic viscosity of the

solvent. DME and DMSO have dynamic viscosities of 0.47 and 1.99 cP respectively, resulting in an $\text{Li}^+\text{-O}_2^-$ diffusivity in DMSO of $9.5 \times 10^{-11} \text{ m}^2/\text{s}$.

Plugging the above values into the above expression for N with a rotation rate of 900 rpm results in the relationship between N and k shown in Figure 3-6. For very low values of k ($\ll 0.01 \text{ s}^{-1}$), all superoxide generated at the disk will be collected at the ring, and the collection efficiency remains constant at the geometric value. In contrast, as k increases above 0.1 s^{-1} , lower collection efficiencies start to result due to high superoxide reactivity. The RRDE collection efficiency of $\sim 5\%$ at high overpotentials (Figure 3-3d) is consistent with first order superoxide reaction rate constants of 2.3 and 5.0 s^{-1} in DMSO and DME respectively. These constants are much higher than experimental $\text{Li}^+\text{-O}_2^-$ disproportionation rate constants estimated in DMSO,⁶⁷ acetonitrile⁶⁶ and tetraglyme¹⁴⁷ at 0.07 s^{-1} , $2.9 \times 10^{-3} \text{ s}^{-1}$ and $2.4 \times 10^{-5} \text{ s}^{-1}$ respectively. A possible exception is a recent study of Li^+ -induced O_2^- disproportionation in DMSO which reported a second-order rate constant of $24.6 \text{ M}^{-1} \text{ s}^{-1}$.¹⁰² For 100 mM Li^+ , this translates to a first-order constant of 2.46 s^{-1} which is on par with 2.3 s^{-1} . The study, however, only reported first-order behavior in Li^+ concentration between 0 and 40 mM ; higher concentrations of Li^+ may result in a lower rate constant. This, in addition to the energetics considerations presented in the main text, leads us to believe that the ORR at high overpotentials more direct $2e^-$ reduction of O_2 , rather than fast $\text{Li}^+\text{-O}_2^-$ disproportionation, although disproportionation is likely to occur to some degree, for species not in direct contact with the electrode.

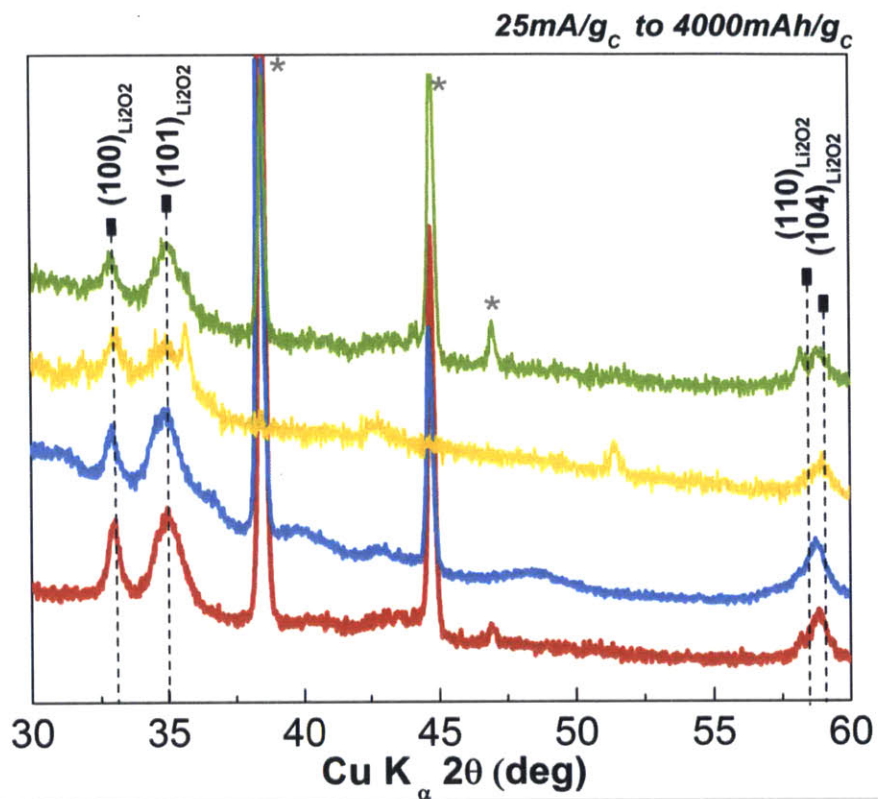


Figure B 6. XRD spectra of CNT electrodes discharged at 25 mA/g_c to 4000 mAh/g_c in 0.1M LiClO₄ in DME (red), 1M LiNO₃ in DMA (blue), 0.1M LiClO₄ in DMSO (yellow) and MeCN (green). Li₂O₂ was detected as the major crystalline product in all discharged electrodes.

Appendix C

Table C 1. Proton solvation energies in a range of organic solvents and the solvents' dielectric constants

Solvent	$\Delta G_s(\text{H}^+)$, kcal/mol	ϵ
DMSO	-273.31 ⁸⁹	46.7
MeCN	-260.2 ⁸⁹	36.64
MeOH	-253.6 ⁸⁹	32.63
EtOH	-250.2 ²¹⁷	24.85
Benzene	-211.5	2.271
Chloroform	-209.6	4.711
Acetone	-251.0	20.49

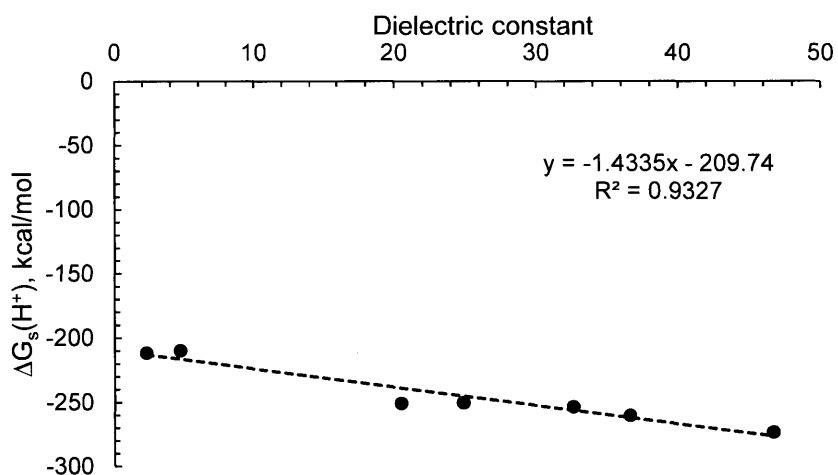


Figure C 1. The proton solvation energy, $\Delta G_s(\text{H}^+)$, in organic solvents plotted against the solvents' dielectric constants.

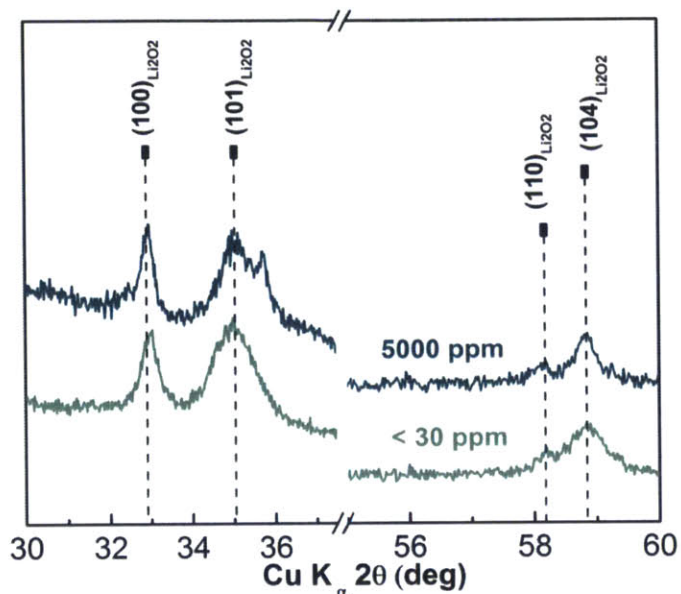


Figure C2. XRD patterns of Li-O₂ CNT electrodes discharged at 25 mA/g_C in 0.1M LiClO₄ in DME with < 30 ppm and 5000 ppm of water.

Calculation of water addition to electrolyte through cell leakage

As noted previously, all Li-O₂ cells were pressurized to 25 psi gage, and were noted to have a leak rate of ~ 0.5 psi/day. This translates to a molar loss that can be calculated with the ideal gas equation:

$$\frac{dN}{dt} = \frac{dP}{RT} V$$

where dN/dt is the molar rate of gas loss, dP/dt is the pressure loss, V is internal cell volume, and R and T are the molar gas constant and temperature respectively. For an internal cell volume of 3.5 ml at room temperature, this results in 3.38 nmole/min.

Assuming that water from ambient air leaks into the cell at a similar rate, we can calculate the rate of water addition to the electrolyte. The saturated vapor pressure of water at 25 °C and 1 atm is 0.023 bar. For a relative humidity of 50%, this results in a mole fraction of water in air =

$$\frac{RH \times 0.023 \text{ bar}}{\text{total pressure}} = 0.011. \text{ Thus, the number of moles of water per minute is } 0.011 \times$$

$$3.38 \text{ nmole/min} = 0.038 \frac{\text{nmole}}{\text{min}}. \text{ The mass of water added after 160 h is}$$

$$0.038 \text{ nmole/min} \times 18 \frac{\text{g}}{\text{mol}} \times 160 \text{ h} = 6.64 \mu\text{g}$$

In contrast, the mass of water required for a 5000 ppm water concentration is $5000 \text{ ppm} \times 200 \mu\text{l of dimethoxyethane} \times 0.867 \text{ g/cm}^3 = 867 \mu\text{g}$, which is two orders of magnitude greater than the estimated amount added.

It is important to note that although this calculation does not consider water ingress by diffusion through the Teflon spacers of the air cell, the actual amount of water in the electrolyte would be much less than the value calculated here, mainly because (i) the real rate of water entry will be much less than the rate of gas leakage from the cell, due to the adverse pressure differential and (ii) not all the water that enters the cell in vapor phase will dissolve in the electrolyte, i.e. some of it will remain in the gas phase, in equilibrium with solvated water.

Calculation of theoretical CNT discharge capacity assuming void volume filling

CNT electrodes used in this study averaged $1 \text{ cm} \times 1 \text{ cm} \times 500 \mu\text{m} = 0.03 \text{ cm}^3$ and $500 \mu\text{g}$ in mass. Assuming 60% of the volume of the electrode was available for Li_2O_2 filling (given a void volume of 90%, and the rest occupied by electrolyte) would result in a charge per electrode of

$$Q = \frac{2.36 \frac{g}{cm^3} \times 0.03 \text{ cm}^3 \times 0.6 \times 2 \times 96485 \text{ C/mol}}{46 \text{ g/mol}} = 50 \text{ mAh}$$

For an electrode mass of 500 μg , this results in a discharge capacity of 100, 000 mAh/gc.

Table C 2. Computed solvation energies of water in DME, MeCN, DMF and DMA using the CCSD/aug-cc-pVTZ level of theory.

Solvent	ΔG_{sol} (kJ/mol)
DME	-11.92
MeCN	-17.07
DMF	-17.11
DMA	17.12

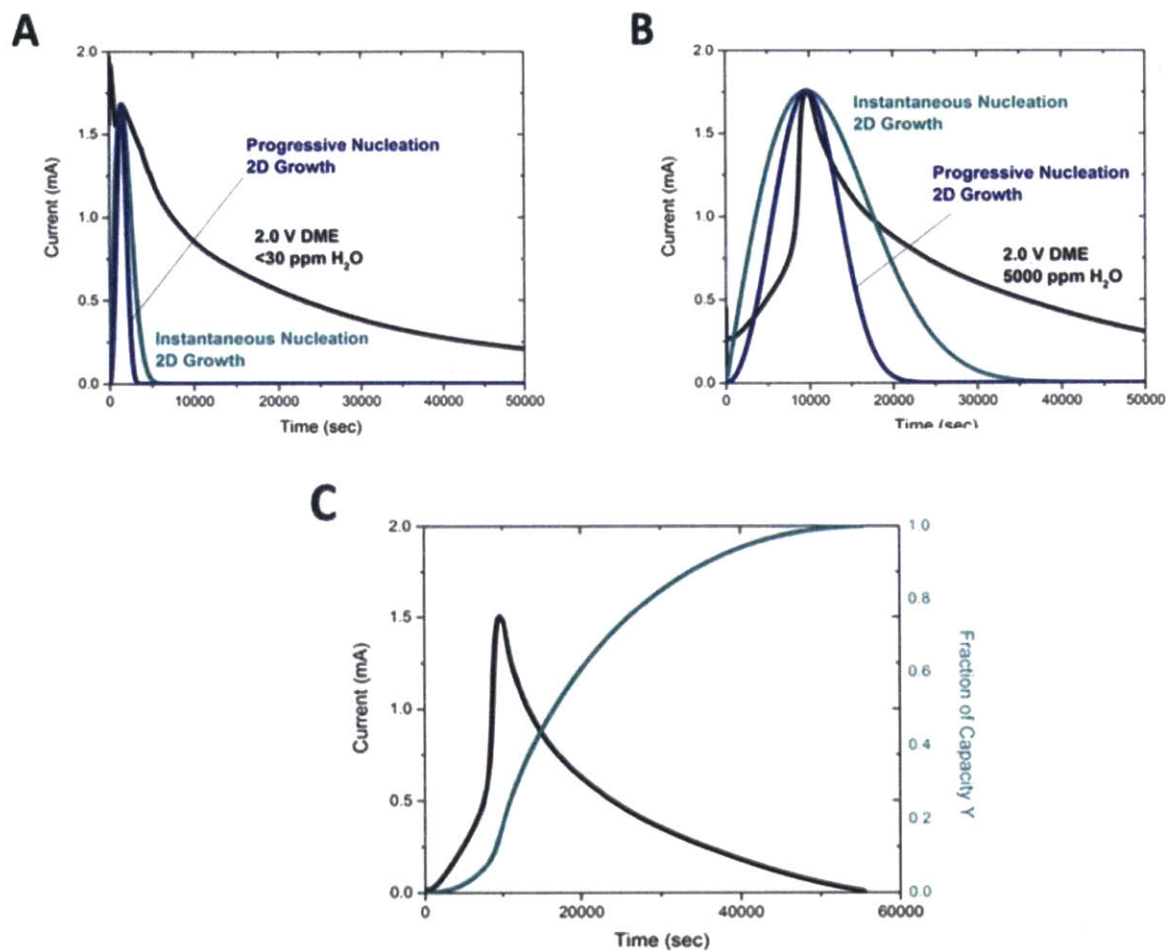


Figure C3. Current transients fitted with models for 2-dimensional growth and instantaneous or progressive nucleation for a carbon paper electrode discharged at 2.0 V in 0.1 M LiClO₄ DME with (a) <math><30\text{ ppm H}_2\text{O}</math> and (b) $5000\text{ ppm H}_2\text{O}$. (c) Current transient in (b) adjusted so that the local minimum represents the point of zero current and capacity.

Discussion of Figure C3.

The equations used for fitting the transients in Figure 4-3a were $I/I_m = t^2/t_m^2 \cdot \exp[-2/3 \cdot (t^3/t_m^3 - 1)]$ for progressive nucleation and 2D growth and $I/I_m = t/t_m \cdot \exp[-2/3 \cdot (t^2/t_m^2 - 1)]$ for instantaneous nucleation and 2D growth, where I and t are current and time, and I_m and t_m are the maximum current and the time it occurs in the peak, respectively.^{170,175,218} These fits can roughly

describe the transients in the vicinity of the current peaks but fail to account for the slow current decay at long times (Figure C3a-b). We hypothesize that the experimental data is a composite of currents related to solvent and surface-mediated processes. Solvent-mediated processes would be expected to generate a slowly monotonic decaying current, as solvated $\text{Li}^+\text{-O}_2^-$ disproportionates and aggregates in solution,^{104,173} before precipitating on and passivating the surface. Current related to direct surface-mediated growth of Li_2O_2 , on the other hand, creates a peak and sharp current decay, as predicted by electrodeposition models of nucleation and growth. Since the solvent-mediated current was not incorporated, the analysis overestimates the magnitude of the surface mediated current peak and it is not possible to unambiguously distinguish between behavior typical of an Avrami exponent of $n=2$ (instantaneous nucleation with 2-D growth) or $n=3$ (constant progressive nucleation with 2-D growth), which both roughly fit the peak shape. In order to try to determine which behavior was present, the peak was isolated by considering capacity and current to be zero at the local minimum in the current transient before the peak and considering the total capacity to be reached when the current returned to this value after the peak. The analysis assumes that there is a constant current due to a solution-mediated process that does not contribute to the peak and is not included in the fractional capacity calculation. This assumption follows from positing that changes in the surface mediated current dominate over changes in the solvent mediated current in the time regime under the peak in total current. The plot in Figure C3c based on fractional capacity in 5000 ppm H_2O allows an estimate of n by fitting the slope of the line, as seen in Figure 4-3b. This preliminary result that $n\sim 2$ suggests that either the nucleation rate or the growth rate decays with time. For a constant growth rate, a value of $n=2$ suggests that the nucleation rate decreased rapidly with time, such that all nucleation events were essentially simultaneous. Analogous analysis is not shown for the anhydrous DME case as the peak occurred

in an earlier time regime where the assumption of a relatively constant solution current is not reasonable. The assumption is invalid because the amplitude of the peak is small relative to the total current. This can be seen in Figure C3a where a fit was produced based on I_m and t_m for $n=2$ and $n=3$; the modeled current transients only fit the raw data in a small time regime. Further efforts will be needed to refine this analysis to properly fit the contribution of solution-mediated current in order to make rigorous statements about the nature of surface-based nucleation and growth.

Appendix D

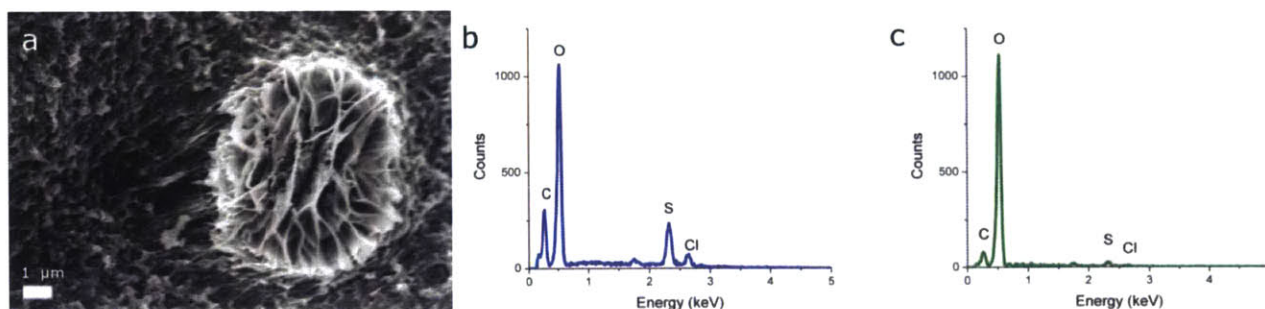
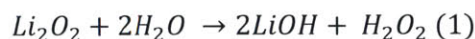


Figure D 1. (a) Flaky particle in a CNT cathode discharged in 0.1 M LiClO₄ DMSO at 25 mA/g_c to ~4000 mAh/g_c (b) energy dispersive x-ray spectroscopy (EDS) spectrum from region of CNTs on left of Figure S2a c) EDS spectrum from region of particle on right of Figure S2a. The lower sulfur and chlorine signal of the particle demonstrates that the particle is not composed of the electrolyte or salt, and the high oxygen signal is consistent with a composition of LiOH.

Calculation of expected LiOH formation from complete conversion of electrochemically formed Li₂O₂.

The reaction expected to form LiOH from Li₂O₂ was assumed to be:



The amount of Li₂O₂ formed electrochemically can be calculated based on the discharge capacity of 3000 mAh/g_c. For a typical electrode mass of 500 μg, this results in a capacity of

$$3000 \frac{\text{mAh}}{\text{g}} \times 500 \mu\text{g} = 1.5 \text{ mAh} \times 3.6 \frac{\text{C}}{\text{mAh}} = 5.4 \text{ C}$$

We can convert this into a molar value (i.e. number of moles of Li₂O₂) via Faraday's Law of Electrolysis. Assuming Faraday's constant of 96,485 C/mol and 2 electrons transferred per mol of Li₂O₂ formed,

$$n = \frac{Q}{F \times Z_r} = 5.4 \frac{C}{96,485 \frac{C}{mol} \times 2} = 2.8 \times 10^{-5} mol$$

Given the 2:1 H₂O:Li₂O₂ stoichiometry implied by equation (1), complete conversion of Li₂O₂ to LiOH would require 5.6×10^{-5} mol of water. A water content of 18 ppm of water (measured by Karl Fischer titration) in 120 μ l of electrolyte used during cell preparation would result in 0.00216 μ l of water in contact with Li₂O₂ in the electrode. Assuming a

$$18 \text{ ppm} \times 120 \mu\text{l} = 2.16 \times 10^{-3} \mu\text{l} \times \frac{0.001 \text{g}}{\mu\text{l}} = 2.16 \times 10^{-6} \text{g} \times \frac{1}{18.02 \text{g/mol}}$$

$$= 1.2 \times 10^{-7} \text{ moles of water}$$

This is roughly 500 times less than what is required for a complete conversion of Li₂O₂ to LiOH.

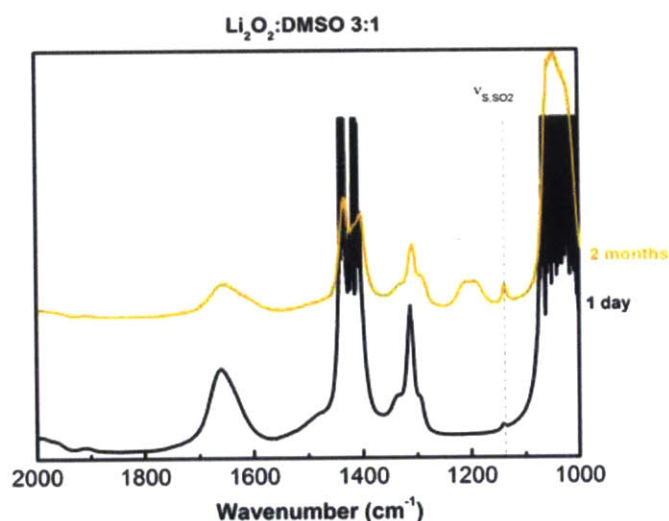
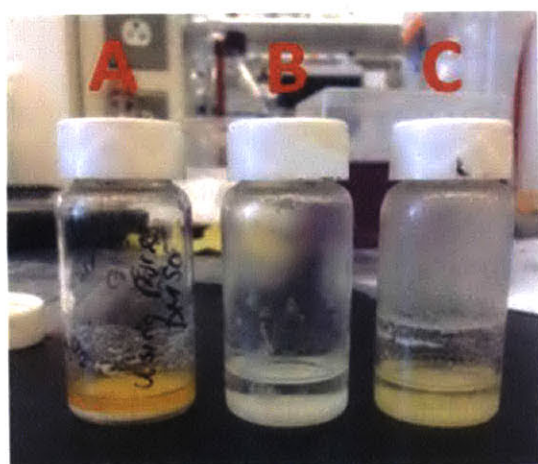


Figure D2. (a) Photographs showing suspensions with molar ratios of A- 1:3 Li₂O₂: DMSO B - 1:1:100 Li₂O₂: DMSO and C - 1:1:100 KO₂: Li₂O₂: DMSO after 1440 hours of mixing. The dark yellow/golden color of mixture A is characteristic of dimethyl sulfone, while mixture C retains the lighter yellow color of KO₂ (b) FTIR spectra of 1:3 Li₂O₂: DMSO after 1 day and 2 months of mixing.

Appendix E – Safety Considerations

There are several safety considerations associated with working with many of the materials used in electrochemical studies of Li-O₂ reactions. In general, extreme caution should be taken in working with hazardous materials, and containment procedures should be strictly observed where necessary. All RDE experiments and cell assembly were done in a sealed Ar-filled glovebox, and personal protective equipment (PPE) was worn at all times (gloves, lab coat and goggles with side shields). A few important material-specific concerns are listed below. Further information can be obtained from the relevant Materials Safety Data Sheets, which are available online at www.sciencelab.com and/or Environmental Health and Safety (EHS).

Lithium

Lithium is highly flammable, reactive and toxic when inhaled, swallowed or put in contact with skin and eyes. It should only be handled in a contained environment, such as an Ar-filled glovebox, away from heat and ignition sources. Lithium waste should be disposed first by immersion in mineral oil, before transport outside the glovebox to a satellite accumulation area for prompt disposal by EHS. In case of a small fire, use dry chemical powder. Large fires should not be fought with water – call EHS and evacuate the area immediately.

Lithium Peroxide

Lithium peroxide is corrosive and a strong oxidizer, and thus biologically harmful. Bulk Li₂O₂ powder used in this study was kept in a glovebox, and cells containing electrochemically discharged Li₂O₂ were opened only in the glovebox.

Organic Solvents

All organic solvents used in this study should be stored in the glovebox and kept away from sources of heat and ignition. There is considerably variability surrounding other precautionary measures necessary. DMSO is combustible but slightly toxic – extra care should however be taken in handling it, as it can readily absorb water and other potentially more hazardous species and absorb through the skin (DMSO absorption through the skin is accompanied by a faint garlicky taste). DME is highly volatile and acutely toxic – particular attention should be paid to the amount of time it has been stored, as it is susceptible to autoxidation and the formation of explosive organic peroxides. Small spills can be diluted with water and mopped up with absorbent. In case of large spills, prevent entry into sewers and contact with ignition sources where possible, and evacuate the area and call EHS. Do not induce vomiting if swallowed.

Carbon Nanotubes

CNTs are an acute respiratory hazard, particularly when not fixed to a substrate, and can cause a dust explosion. Weighing outside the glovebox should be done in a nanoparticle containment hood, and PPE should be supplemented with a respirator if possible.

REFERENCES

1. H. B. Gray, *Nat. Chem.*, **1**, 7 (2009).
2. N. S. Lewis and D. G. Nocera, *Proc. Natl. Acad. Sci. U. S. A.*, **103**, 15729–35 (2006).
3. R. F. Service, *Science (80-.)*, **324**, 1257–1259 (2009).
4. H. A. Gasteiger and N. M. Marković, *Science*, **324**, 48–9 (2009).
5. B. Dunn, H. Kamath, and J.-M. Tarascon, *Science*, **334**, 928–35 (2011).
6. M. Armand and J.-M. Tarascon, *Nature*, **451**, 652–7 (2008).
7. J.-M. Tarascon and M. Armand, *Nature*, **414**, 359 (2001).
8. P. G. Bruce, S. A. Freunberger, L. J. Hardwick, and J.-M. Tarascon, *Nat. Mater.*, **11**, 19–29 (2012).
9. Y.-C. Lu et al., *Energy Environ. Sci.*, **6**, 750 (2013).
10. N. Imanishi, A. C. Luntz, and P. Bruce, *The Lithium Air Battery* N. Imanishi, A. C. Luntz, and P. Bruce, Editors, p. 121-158, Springer New York, New York, NY, (2014).
11. K. G. Gallagher et al., *Energy Environ. Sci.*, **7**, 1555–1563 (2014).
12. Z.-L. Wang, D. Xu, J.-J. Xu, L.-L. Zhang, and X.-B. Zhang, *Adv. Funct. Mater.*, **22**, 3699–3705 (2012).
13. R. R. Mitchell, B. M. Gallant, C. V. Thompson, and Y. Shao-Horn, *Energy Environ. Sci.*, **4**, 2952 (2011).
14. B. M. Gallant et al., *J. Phys. Chem. C*, **116**, 20800–20805 (2012).
15. Z. Peng, S. A. Freunberger, Y. Chen, and P. G. Bruce, *Science*, **337**, 563–6 (2012).
16. H. Chen et al., *ChemSusChem*, **1**, 348–355 (2008).
17. K. Kang, Y. S. Meng, J. Bréger, C. P. Grey, and G. Ceder, *Science (80-.)*, **311**, 977–980 (2006).
18. M. Radin and D. Siegel, *Energy Environ. Sci.*, **6**, 2370–2379 (2013).
19. A. C. Luntz et al., *J. Phys. Chem. Lett.*, 3494–3499 (2013).
20. V. Viswanathan et al., *J. Chem. Phys.*, **135**, 214704 (2011).
21. K. B. Knudsen, A. C. Luntz, S. H. Jensen, T. Vegge, and J. Hjelm, *J. Phys. Chem. C*, **119**, acs.jpcc.5b08757 (2015).

22. M. D. Radin, C. W. Monroe, and D. J. Siegel, *J. Phys. Chem. Lett.*, **6**, 3017–22 (2015).
23. J. M. Garcia-Lastra, J. D. Bass, and K. S. Thygesen, *J. Chem. Phys.*, **135**, 121101 (2011).
24. Y.-C. Lu et al., *Energy Environ. Sci.*, 2999–3007 (2011).
25. D. G. Kwabi et al., *MRS Bull.*, **39**, 443–452 (2014).
26. A. M. Ullman et al., *Inorg. Chem.*, **53**, 5384–91 (2014).
27. Y. Chen, S. A. Freunberger, Z. Peng, O. Fontaine, and P. G. Bruce, *Nat. Chem.*, **5**, 489–94 (2013).
28. G. V. Chase et al., (2012).
29. Y. Wang, Z. Liang, Q. Zou, G. Cong, and Y.-C. Lu, *J. Phys. Chem. C*, acs.jpcc.6b00984 (2016).
30. J. R. Harding, Y.-C. Lu, Y. Tsukada, and Y. Shao-Horn, *Phys. Chem. Chem. Phys.*, **14**, 10540–10546 (2012).
31. A. Débart, A. J. Paterson, J. Bao, and P. G. Bruce, *Angew. Chem. Int. Ed. Engl.*, **47**, 4521–4 (2008).
32. K. P. C. Yao et al., *Energy Environ. Sci.* (2015).
33. D. Kundu et al., *J. Phys. Chem. Lett.*, 150501105350002 (2015).
34. S. A. Freunberger et al., *J. Am. Chem. Soc.*, **133**, 8040–7 (2011).
35. V. S. Bryantsev and M. Blanco, 379–383 (2011).
36. J. P. Vivek, N. G. Berry, G. Papageorgiou, R. J. Nichols, and L. J. Hardwick, *J. Am. Chem. Soc.* (2016).
37. D. Sharon et al., *J. Phys. Chem. Lett.*, **4**, 3115–3119 (2013).
38. Y. Chen, S. A. Freunberger, Z. Peng, F. Barde, and P. G. Bruce, *J. Am. Chem. Soc.*, **134**, 7952–7957 (2012).
39. V. S. Bryantsev and F. Faglioni, *J. Phys. Chem. A*, **116**, 7128–38 (2012).
40. B. D. Adams et al., *Adv. Energy Mater.*, **5**, 1400867 (2015).
41. S. A. Freunberger et al., *Angew. Chem. Int. Ed. Engl.*, **50**, 8609–13 (2011).
42. J. R. Harding, C. V. Amanchukwu, P. T. Hammond, and Y. Shao-Horn, *J. Phys. Chem. C*, **119**, 6947–6955 (2015).
43. Z. Zhang et al., *J. Phys. Chem. C*, 111114162059002 (2011).
44. D. Sharon et al., *J. Phys. Chem. C*, 140624170836000 (2014).

45. V. S. Bryantsev et al., *J. Phys. Chem. C*, 130520171032004 (2013).
46. S. Monaco et al., *Electrochim. Acta*, **83**, 94–104 (2012).
47. S. Monaco, F. Soavi, and M. Mastragostino, *J. Phys. Chem. Lett.*, 1379–1382 (2013).
48. K. U. Schwenke, J. Herranz, H. A. Gasteiger, and M. Piana, *J. Electrochem. Soc.*, **162**, A905–A914 (2015).
49. W. Walker et al., *J. Am. Chem. Soc.*, **135**, 2076–9 (2013).
50. D. M. Itkis et al., *Nano Lett.*, **13**, 4697–701 (2013).
51. E. Y. Kataev et al., *ACS Nano*, **9**, 320–6 (2015).
52. B. D. McCloskey et al., *J. Phys. Chem. Lett.*, **3**, 997–1001 (2012).
53. M. M. Ottakam Thotiyl, S. A. Freunberger, Z. Peng, and P. G. Bruce, *J. Am. Chem. Soc.*, **135**, 494–500 (2012).
54. R. Younesi et al., *J. Phys. Chem. C*, 120807123830006 (2012).
55. R. Black et al., *J. Am. Chem. Soc.*, **134**, 2902–5 (2012).
56. M. M. Ottakam Thotiyl et al., *Nat. Mater.*, **12**, 1050–1056 (2013).
57. L. Nazar, D. Kundu, R. Black, and E. Jämstorp, *Energy Environ. Sci.* (2014).
58. D. Wittmaier, N. A. Cañas, I. Biswas, and K. A. Friedrich, *Adv. Energy Mater.*, **5**, n/a–n/a (2015).
59. W. Yang et al., *Electrochem. commun.*, **28**, 13–16 (2013).
60. N. S. Lewis and D. G. Nocera, *Proc. Natl. Acad. Sci. U. S. A.*, **104**, 20142 (2007).
61. G. M. Whitesides and G. W. Crabtree, *Science*, **315**, 796–8 (2007).
62. P. Hartmann et al., *Nat. Mater.*, **advance on** (2012).
63. R. F. Service, *Science*, **324**, 1257–9 (2009).
64. D. T. Sawyer and M. J. Gibian, *Tetrahedron*, **35**, 1471–1481 (1979).
65. D. L. Maricle and W. G. Hodgson, *Anal. Chem.*, **37**, 1562–1565 (1965).
66. Z. Peng et al., *Angew. Chem. Int. Ed. Engl.*, **50**, 6351–5 (2011).
67. L. Johnson et al., *Nat. Chem.*, **6**, 1091–9 (2014).
68. C. O. Laoire, S. Mukerjee, K. M. Abraham, E. J. Plichta, and M. A. Hendrickson, *J. Phys. Chem. C*, **114**, 9178–9186 (2010).
69. B. D. McCloskey, R. Scheffler, A. Speidel, G. Girishkumar, and A. C. Luntz, *J. Phys. Chem.*

- C, **116**, 23897–23905 (2012).
70. L. Nazar et al., *Energy Environ. Sci.*, **6**, 1772–1778 (2013).
71. B. M. Gallant et al., *Energy Environ. Sci.*, **6**, 2518 (2013).
72. Y. Qiao and S. Ye, *J. Phys. Chem. C*, 1932–7447 (2015).
73. R. Cao et al., *ChemSusChem*, **7**, 2436–40 (2014).
74. C. O. Laoire, S. Mukerjee, K. M. Abraham, E. J. Plichta, and M. A. Hendrickson, *J. Phys. Chem. C*, **113**, 20127–20134 (2009).
75. V. Gutmann, *Coord. Chem. Rev.*, **18**, 225–255 (1976).
76. D. T. Sawyer, G. Chiericato, C. T. Angells, E. J. Nanni, and T. Tsuchiya, *Anal. Chem.*, **2**, 1720–1724 (1982).
77. V. S. Bryantsev et al., *J. Phys. Chem. A*, **115**, 12399–409 (2011).
78. U. Mayer, V. Gutmann, and W. Gerger, *Monatshefte fur Chemie*, **106**, 1235–1257 (1975).
79. G. Gritzner, *J. Phys. Chem.*, **90**, 5478–5485 (1986).
80. I. Noviandri et al., 6713–6722 (2006).
81. W. J. Albery, J. S. Drury, and M. L. Hitchman, *Trans. Faraday Soc.*, **67**, 161 (1971).
82. J. Herranz, A. Garsuch, and H. A. Gasteiger, *J. Phys. Chem. C*, **116**, 19084–19094 (2012).
83. V. S. Bryantsev, D. Addison, and G. V. Chase, *J. Electrochem. Soc.*, **160**, H818–H819 (2013).
84. Y.-C. Lu, H. A. Gasteiger, and Y. Shao-Horn, *J. Am. Chem. Soc.*, **133**, 19048–19051 (2011).
85. V. S. Bryantsev, M. S. Diallo, and W. A. Goddard, *J. Phys. Chem. B*, **112**, 9709–19 (2008).
86. A. A. Isse and A. Gennaro, *J. Phys. Chem. B*, **114**, 7894–9 (2010).
87. A. V Marenich, A. Majumdar, M. Lenz, C. J. Cramer, and D. G. Truhlar, *Angew. Chem. Int. Ed. Engl.*, **51**, 12810–4 (2012).
88. A. Frumkin and B. Damaskin, *Dokl. Akad. Nauk SSSR*, **221**, 395–398 (1975).
89. C. P. Kelly, C. J. Cramer, and D. G. Truhlar, *J. Phys. Chem. B*, **111**, 408–22 (2007).
90. V. S. Bryantsev, *Theor. Chem. Acc.*, **131**, 1250 (2012).
91. Y. Zhao and D. G. Truhlar, *J. Chem. Phys.*, **125**, 194101 (2006).
92. Y. Zhao and D. G. Truhlar, *Theor. Chem. Acc.*, **120**, 215–241 (2007).
93. M. J. Blanco, *Comput. Chem.*, **12**, 237–247 (1991).

94. N. G. Tsierkezos, *J. Solution Chem.*, **36**, 289–302 (2007).
95. D. Aurbach, M. Daroux, P. Faguy, and E. Yeager, *J. Electroanal. Chem. Interfacial Electrochem.*, **297**, 225–244 (1991).
96. V. S. Bryantsev et al., *J. Electrochem. Soc.*, **160**, A160–A171 (2012).
97. D. Xu, Z. Wang, J. Xu, L. Zhang, and X. Zhang, *Chem. Commun. (Camb.)*, **48**, 6948–50 (2012).
98. M. J. Trahan, S. Mukerjee, E. J. Plichta, M. A. Hendrickson, and K. M. Abraham, *J. Electrochem. Soc.*, **160**, A259–A267 (2012).
99. C. J. Allen et al., *J. Phys. Chem. C*, **116**, 20755–20764 (2012).
100. D. Sharon et al., *J. Phys. Chem. Lett.*, **4**, 127–131 (2013).
101. U. Das, K. C. Lau, P. C. Redfern, and L. A. Curtiss, *J. Phys. Chem. Lett.*, **5**, 813–819 (2014).
102. Y. Zhang et al., *J. Phys. Chem. C*, [acs.jpcc.5b12338](https://doi.org/10.1021/acs.jpcc.5b12338) (2016).
103. E. J. Calvo and N. Mozhzhukhina, *Electrochem. commun.*, **31**, 56–58 (2013).
104. T. K. Zakharchenko, A. Y. Kozmenkova, D. M. Itkis, and E. A. Goodilin, *Beilstein J. Nanotechnol.*, **4**, 758–62 (2013).
105. R. Black et al., **134**, 2901–2905 (2012).
106. R. G. Pearson, *Inorg. Chem.*, **27**, 734–740 (1988).
107. M. Okoshi, Y. Yamada, A. Yamada, and H. Nakai, *J. Electrochem. Soc.*, **160**, A2160–A2165 (2013).
108. M. J. Ziegler and J. D. Madura, *J. Solution Chem.*, **40**, 1383–1398 (2011).
109. N. B. Aetukuri et al., *Nat. Chem.*, **7**, 50–56 (2014).
110. D. G. Kwabi et al., *J. Phys. Chem. Lett.*, 2850–2856 (2014).
111. N. Mozhzhukhina, L. P. Méndez De Leo, and E. J. Calvo, *J. Phys. Chem. C*, 18375–1830 (2013).
112. A. Khetan, A. Luntz, and V. Viswanathan, *J. Phys. Chem. Lett.*, **6**, 1254–1259 (2015).
113. K. Ueno et al., *Phys. Chem. Chem. Phys.*, **17**, 8248–57 (2015).
114. K. Ueno et al., *J. Phys. Chem. B*, **116**, 11323–31 (2012).
115. K. Fujii et al., *J. Phys. Chem. C*, 19314–19324 (2013).
116. P. Albertus et al., *J. Electrochem. Soc.*, **158**, A343 (2011).

117. S. Lau and L. A. Archer, *Nano Lett.*, **15**, 5995–6002 (2015).
118. W. Fan, Z. Cui, and X. Guo, *J. Phys. Chem. C*, 2623–2627 (2013).
119. Y.-C. Lu, H. A. Gasteiger, E. Crumlin, R. McGuire, and Y. Shao-Horn, *J. Electrochem. Soc.*, **157**, A1016 (2010).
120. R. R. Mitchell, B. M. Gallant, Y. Shao-Horn, and C. V. Thompson, *J. Phys. Chem. Lett.*, **4**, 1060–1064 (2013).
121. C. Xia et al., *ACS Appl. Mater. Interfaces*, **6**, 12083–92 (2014).
122. B. Horstmann et al., *J. Phys. Chem. Lett.*, 4217–4222 (2013).
123. M. D. Radin, J. F. Rodriguez, F. Tian, and D. J. Siegel, *J. Am. Chem. Soc.*, **134**, 1093–103 (2012).
124. S. Ong, Y. Mo, and G. Ceder, *Phys. Rev. B*, **85**, 2–5 (2012).
125. J. S. Hummelshøj et al., *J. Chem. Phys.*, **132**, 071101 (2010).
126. C. M. Burke, V. Pande, A. Khetan, V. Viswanathan, and B. D. McCloskey, *Proc. Natl. Acad. Sci. U. S. A.*, **112**, 9293–8 (2015).
127. D. Sharon et al., *ACS Appl. Mater. Interfaces*, **7**, 16590–16600 (2015).
128. K. U. Schwenke, M. Metzger, T. Restle, M. Piana, and H. A. Gasteiger, *J. Electrochem. Soc.*, **162**, A573–A584 (2015).
129. E. Budevski, G. Staikov, and W. J. Lorenz, Eds., *Electrochemical Phase Formation and Growth*, Wiley-VCH Verlag GmbH, Weinheim, Germany, (1996).
130. H. Zheng et al., *Nano Lett.*, **14**, 4245–4249 (2014).
131. J. Varley, V. Viswanathan, J. K. Nørskov, and A. Luntz, *Energy Environ. Sci.*, **7**, 720–727 (2013).
132. J. S. Hummelshøj, a C. Luntz, and J. K. Nørskov, *J. Chem. Phys.*, **138**, 034703 (2013).
133. O. Gerbig, R. Merkle, and J. Maier, *Adv. Mater.*, **25**, 3129–33 (2013).
134. W. T. Geng, B. L. He, and T. Ohno, *J. Phys. Chem. C*, 25222–25228 (2013).
135. J. M. Garcia-Lastra, J. S. G. Myrdal, R. Christensen, K. S. Thygesen, and T. Vegge, *J. Phys. Chem. C*, 5568–5577 (2013).
136. M. D. Radin, C. W. Monroe, and D. J. Siegel, *Chem. Mater.*, **27**, 839–847 (2015).
137. D. Zhai et al., *J. Phys. Chem. Lett.*, **5**, 2705–2710 (2014).
138. J. Yang et al., *Phys. Chem. Chem. Phys.*, **15**, 3764–71 (2013).
139. J. Lu et al., *ChemSusChem*, **6**, 1196–202 (2013).

140. D. G. Kwabi et al., *Angew. Chem. Int. Ed. Engl.*, **9**, 3129–34 (2016).
141. J. Agrisuelas et al., *J. Electrochem. Soc.*, **154**, F134 (2007).
142. N. Ortiz-Vitoriano et al., *J. Phys. Chem. Lett.*, **6**, 2636–2643 (2015).
143. S. Meini et al., *Phys. Chem. Chem. Phys.*, **15**, 11478–93 (2013).
144. S. Schaltin, G. Vanhoutte, M. Wu, F. Bardé, and J. Fransaer, *Phys. Chem. Chem. Phys.*, **17**, 12575–12586 (2015).
145. G. Sauerbrey, *Zeitschrift für Phys.*, **155**, 206–222 (1959).
146. H.-K. Lim et al., *J. Am. Chem. Soc.*, 9733–9742 (2013).
147. D. Zhai et al., *J. Am. Chem. Soc.*, **135**, 15364–72 (2013).
148. J. Lu et al., *Nature*, **529**, 377–382 (2016).
149. K. U. Schwenke, S. Meini, X. Wu, H. A. Gasteiger, and M. Piana, *Phys. Chem. Chem. Phys.*, **15**, 11830–9 (2013).
150. H. Geaney and C. ODwyer, *Phys. Chem. Chem. Phys.* (2015).
151. B. Sun, P. Munroe, and G. Wang, *Sci. Rep.*, **3**, 1–7 (2013).
152. D. Xu et al., *Chem. Commun. (Camb.)*, **48**, 11674–6 (2012).
153. T. Wang, M. Antonietti, and H. Cölfen, *Chemistry*, **12**, 5722–30 (2006).
154. H. Cölfen and S. Mann, *Angew. Chem. Int. Ed. Engl.*, **42**, 2350–65 (2003).
155. Y. Xu and W. a. Shelton, *J. Electrochem. Soc.*, **158**, A1177 (2011).
156. D. Sharon et al., *ACS Appl. Mater. Interfaces*, **8**, 5300–5307 (2016).
157. S. Meini, M. Piana, N. Tsiouvaras, A. Garsuch, and H. A. Gasteiger, *Electrochem. Solid-State Lett.*, **15**, A45 (2012).
158. J. Uddin et al., *J. Phys. Chem. Lett.*, 3760–3765 (2013).
159. T. Laino and A. Curioni, *New J. Phys.*, **15**, 095009 (2013).
160. N. Kumar, M. D. Radin, B. C. Wood, T. Ogitsu, and D. J. Siegel, *J. Phys. Chem. C*, **119**, 9050–9060 (2015).
161. R. S. Assary, K. C. Lau, K. Amine, Y.-K. Sun, and L. A. Curtiss, *J. Phys. Chem. C*, **117**, 8041–8049 (2013).
162. W. Sun, S. Jayaraman, W. Chen, K. A. Persson, and G. Ceder, *Proc. Natl. Acad. Sci. U. S. A.*, 1423898112– (2015).
163. P. Bénézech, G. D. Saldi, J.-L. Dandurand, and J. Schott, *Chem. Geol.*, **286**, 21–31 (2011).

164. Z. Guo, X. Dong, S. Yuan, Y. Wang, and Y. Xia, *J. Power Sources*, **264**, 1–7 (2014).
165. D. T. Sawyer and J. S. Valentine, *Acc. Chem. Res.*, **14**, 393–400 (1981).
166. D. H. Chin, G. Chiericato, E. J. Nanni, and D. T. Sawyer, *J. Am. Chem. Soc.*, **104**, 1296–1299 (1982).
167. Y. Che et al., *J. Phys. Chem.*, **100**, 20134–20137 (1996).
168. C. P. Andrieux, P. Hapiot, and J. M. Saveant, *J. Am. Chem. Soc.*, **109**, 3768–3775 (1987).
169. F. Y. Fan, W. C. Carter, and Y.-M. Chiang, *Adv. Mater.* (2015).
170. L. C. H. Gerber et al., *Nano Lett.*, **16**, 549–54 (2016).
171. S. Miertuš, E. Scrocco, and J. Tomasi, *Chem. Phys.*, **55**, 117–129 (1981).
172. D. J. Frisch, M. J.; Trucks, G. W.; Schlegel, H. B.; Scuseria, G. E.; Robb, M. A.; Cheeseman, J. R.; Scalmani, G.; Barone, V.; Mennucci, B.; Petersson, G. A.; Nakatsuji, H.; Caricato, M.; Li, X.; Hratchian, H. P.; Izmaylov, A. F.; Bloino, J.; Zheng, G.; Sonnenb, (2009).
173. D. G. Kwabi et al., *J. Phys. Chem. Lett.* (2016).
174. L. Guo, G. Oskam, A. Radisic, P. M. Hoffmann, and P. C. Searson, *J. Phys. D. Appl. Phys.*, **44**, 443001 (2011).
175. A. Bewick, M. Fleischmann, and H. R. Thirsk, *Trans. Faraday Soc.*, **58**, 2200 (1962).
176. M. Avrami, *J. Chem. Phys.*, **8**, 212 (1940).
177. A. Jorio, M. S. Dresselhaus, R. Saito, and G. Dresselhaus, *Raman Spectroscopy in Graphene Related Systems*, p. 368, Wiley, Weinheim, Germany, (2011).
178. D. T. Sawyer, *Oxygen Chemistry*, p. 240, Oxford University Press, USA, (1991).
179. I. B. Afanas'ev, *Superoxide Ion: Chemistry and Biological Implications, Volume 2*, p. 232, CRC Press, (1991).
180. E. J. Nanni, M. D. Stallings, and D. T. Sawyer, *J. Am. Chem. Soc.*, **102**, 4481–4485 (1980).
181. W. N. Olmstead, Z. Margolin, and F. G. Bordwell, *J. Org. Chem.*, **45**, 3295–3299 (1980).
182. W. S. Matthews et al., *J. Am. Chem. Soc.*, **97**, 7006–7014 (1975).
183. C. Xia, R. Black, R. Fernandes, B. Adams, and L. F. Nazar, *Nat. Chem.*, **7**, 496–501 (2015).
184. T. Liu et al., *Science (80-.)*, **350**, 530–533 (2015).
185. W.-J. Kwak et al., *J. Mater. Chem. A*, **3**, 8855–8864 (2015).
186. T. Zhang, K. Liao, P. He, and H. Zhou, *Energy Environ. Sci.* (2016).
187. F. Li et al., *Nat. Commun.*, **6**, 7843 (2015).

188. Y. Liu et al., *Energy Environ. Sci.* (2015).
189. J. Portier, P. Poizot, G. Campet, M. A. Subramanian, and J.-M. Tarascon, *Solid State Sci.*, **5**, 695–699 (2003).
190. B. D. McCloskey, D. S. Bethune, R. M. Shelby, G. Girishkumar, and A. C. Luntz, **2**, 1161–1166 (2011).
191. W. Xu et al., *J. Power Sources*, **215**, 240–247 (2012).
192. B. D. McCloskey et al., *J. Phys. Chem. Lett.*, **4**, 2989–2993 (2013).
193. A. Frimeh, in *The chemistry of peroxides*, S. Patai, Editor, p. 429–461, John Wiley & Sons, Inc., Manchester (1983).
194. A. D. Goolsby and D. T. Sawyer, *Anal. Chem.*, **40**, 83–86 (1968).
195. H. Gampp and S. J. Lippard, *Inorg. Chem.*, **22**, 357–358 (1983).
196. D. Krishnamurti, *Proc. Indian Acad. Sci. - Sect. A*, **50**, 247–253 (1959).
197. R. Younesi, P. Norby, and T. Vegge, *ECS Electrochem. Lett.*, **3**, A15–A18 (2014).
198. K. P. C. Yao et al., *J. Electrochem. Soc.*, **160**, A824–A831 (2013).
199. S. E. Stein, *NIST Mass Spectrom. Data Cent.* (2011)
<http://webbook.nist.gov/cgi/cbook.cgi?ID=C67710&Mask=608>.
200. J. N. Butler, *J. Electroanal. Chem. Interfacial Electrochem.*, **14**, 89–116 (1967).
201. J. Kim et al., *Nat. Commun.*, **7**, 10670 (2016).
202. R. A. Marcus, *J. Chem. Phys.*, **24**, 966 (1956).
203. R. A. Marcus, *J. Chem. Phys.*, **43**, 679 (1965).
204. C. Hartnig and M. T. M. Koper, *J. Chem. Phys.*, **115**, 8540 (2001).
205. C. Hartnig and M. T. M. Koper, *J. Am. Chem. Soc.*, **125**, 9840–5 (2003).
206. C. Hartnig and M. T. . Koper, *J. Electroanal. Chem.*, **532**, 165–170 (2002).
207. B. Genorio et al., *J. Phys. Chem. C*, [acs.jpcc.5b12230](https://doi.org/10.1021/acs.jpcc.5b12230) (2016).
208. W. J. Royea, T. W. Hamann, B. S. Brunschwig, and N. S. Lewis, *J. Phys. Chem. B*, **110**, 19433–42 (2006).
209. M. Z. Bazant, *Acc. Chem. Res.*, **46**, 1144–60 (2013).
210. M. Tang, W. C. Carter, and Y.-M. Chiang, *Annu. Rev. Mater. Res.*, **40**, 501–529 (2010).
211. A. J. Bard and L. R. Faulkner, *Electrochemical Methods: Fundamentals and Applications, 2nd Edition*, 2nd ed., Wiley, New York, (2000).

212. J. Read et al., *J. Electrochem. Soc.*, **150**, A1351 (2003).
213. V. S. Bryantsev, *Chem. Phys. Lett.*, **558**, 42–47 (2013).
214. NIST, *Chemistry WebBook*, June 2005 ., (2005).
215. H. Muramatsu and K. Kimura, *Anal. Chem.*, **64**, 2502–2507 (1992).
216. A. Bund and M. Schneider, *J. Electrochem. Soc.*, **149**, E331 (2002).
217. L. Rottmannova, V. Lukes, and M. Ilcin, *J. Mol. Struct.*, **1049**, 494–501 (2013).
218. M. Fleischmann and H. R. Thirsk, *Electrochim. Acta*, **9**, 757–771 (1964).